Rayleigh Damped Magnetic Resonance Elastography

M. D. J. McGarry

A thesis submitted in partial fulfilment
of the requirements for the degree of
Master of Engineering
in
Mechanical Engineering
at the
University of Canterbury,
Christchurch, New Zealand.

December 2008

Abstract

A three-dimensional, incompressible, Rayleigh damped magnetic resonance elastography (MRE) material property reconstruction algorithm capable of reconstructing the spatial distribution of both the real and imaginary parts of the shear modulus, density and bulk modulus from full-field MR-detected harmonic motion data was developed. The algorithm uses a subzone-based implementation of motion error minimization techniques, using 27 hexahedral finite elements, and is written in FORTRAN to run on high performance distributed computing systems. The theory behind the methods used is presented in a form that is directly applicable to the code's structure, to serve as a reference for future research building on this algorithm. Globally defined Rayleigh damping parameter reconstructions using simulated data showed that it is possible to reconstruct the correct combination of Rayleigh parameters under noise levels comparable to MR measurements. The elastic wave equation is used to demonstrate that use of a one parameter damping model to fit a Rayleigh damped material can lead to artefacts in the reconstructed damping parameter images, a prediction that is verified using simulated reconstructions. Initial results using MR-detected motion data from both gelatine phantoms and *in-vivo* cases produced good reconstructions of real shear modulus, as well as showing promise for successful imaging of damping properties. An initial investigation into an alternative elemental basis function approach to supporting the material property distribution produced some promising results, as well as highlighting some significant issues with large variations across the elements.

Acknowledgements

Most of the thanks for the help I received during this project is directed at my supervisor, Eli van Houten. I consider myself very fortunate to have had a supervisor who not only provided a great deal of expertise and always had an idea to solve the numerous problems I encountered along the way, but was also just an all-around good guy.

Thanks also to the Fortran dictionary, Hans Uwe-Berger for the initial version of the reconstruction code, to Ashton Peters for providing technical support for anything computer-related, and to Naren Naik for doing anything mathematical that was beyond me. The other students working on this and related projects, Zohreh Barani Lonbani, James Flewellen, Christoph Mittermeier and David Viviers, thanks for all your input as well.

I suppose my better half, Christie, can have a mention, thanks for putting up with me over the last few years, and yes, one day I will get a job.....

The thanks for stopping me from going insane and descending into the deepest realms of Nerd-idity goes to my fishing buddies, Rooney, Rueben, Bret, Milo and Eli. Also to my other friends who stayed living the dream in Christchurch, you guys are alright too.

And finally, I am very grateful for the financial support from NIH/NIBIB R01-EB004632-02.

Contents

List of Figures

List of Tables

NOMENCLATURE

Normal type indicates scalars, bold uppercase indicates a Matrix, bold lowercase indicates a vector. Subscript i, j, k, m and n are general counting variables.

Roman Symbols

$\mathbf{A}$:	Forward FEM matrix.
C_D:	Coefficient of the dashpot of a three parameter solid (Fig. 2.1).
C_{sc}:	Complex scalar, $C_{sc}\theta_{sc} = R_{sc}\mathfrak{Re}\{\theta_{sc}\} + iI_{sc}\mathfrak{Im}\{\theta_{sc}\}$.
$\mathbf{C_m}$:	Damping matrix in discretized form of Navier's equation.
E:	Elastic, or Young's modulus.
E_1 & E_2:	Stiffness of the elastic elements of a three parameter solid (Fig. 2.1).
E^*:	Complex modulus developed from a spring-dashpot configuration.
$\mathbf{G}$:	Direct inversion matrix.
$\mathbf{H}_e$:	Exact Hessian matrix.
$\mathbf{H}$:	Gauss-Newton approximation of $\mathbf{H}_e$.
$\mathbf{H}_r$:	Regularized Hessian.
^{H}:	Complex conjugate transpose operator.
I_{sc}:	Scalar for imaginary part of a variable.
$\mathbf{J}$:	Jacobian matrix, $\frac{\partial \mathbf{u}}{\partial \theta}$.
$\mathbf{J}_c$:	Coordinate Jacobian matrix.
$\|J\|_g$:	Global Jacobian size.
$\mathbf{K_m}$:	Elastic stiffness matrix in discretized form of Navier's equation.
K:	Bulk Modulus, related to E and ν by $K = \frac{E}{3(1-2\nu)}$.
$\mathbf{K_m}$:	Elastic stiffness matrix in discretized form of Navier's equation.
$\mathbf{K'_m}$:	$\mathbf{K_m}$ after taking out a common factor of μ.
L:	Characteristic length.
$\mathscr{L}$:	Differential operator acting on $\mathbf{u}$ from Navier's equation.
$\mathbf{M_m}$:	Mass matrix in discretized form of Navier's equation.
$\mathbf{M'_m}$:	$\mathbf{M_m}$ after taking out a common factor of ρ.
N_{con}:	Number of connected nodes.
N_G :	Number of Gauss points in each direction.
N_{nz} :	Number of non-zero matrix entries.
N_{pv}:	Number of elemental basis functions used to support a variable.
NO:	Number of observations.
NP:	Number of reconstructed parameters.
N_z:	Number of subzones.
P:	Pressure, $P = -\bar{\sigma}$.
$\mathbf{P}_i$:	Vector of pressure DOF's, $\mathbf{P}_i = [P \ \frac{\partial P}{\partial x} \ \frac{\partial P}{\partial y} \ \frac{\partial P}{\partial z}]^T$.

$\bar{P}$:	Complex valued pressure amplitude.
$P(x)$:	Phase of MR-detected motions.
R:	The Residual, defined in Eq. B.13.
R_{sc}:	Scalar for real part of a variable.
V:	Volume.
ΔV:	Change in volume for a particular state of strain.
W_i:	The i'th weighted residual weighting function.
WPS:	Shear wavelengths per side.
$X_1 \rightarrow X_{27}$:	The (ξ, η, ζ) coordinates of the 27 node Hexahedral element.
$\mathbf{X}$:	Linear least squares matrix.
a_1:	First Armijo line search constant.
a_2:	Second Armijo line search constant.
$\mathbf{c}$:	Unknown elemental basis constants for linear least squares.
$c_1 \rightarrow c_{10}$:	Elemental basis function variables (Eq. 2.26).
$\mathbf{c}_a$ & $\mathbf{c}_b$:	Arbitrary complex vectors. Split versions are $\mathbf{r}_a$ and $\mathbf{r}_b$.
e:	Volumetric strain, $e = \epsilon_x + \epsilon_y + \epsilon_z$.
e':	Volumetric strain produced by deviatoric stresses, equal to zero.
f:	Frequency (Hz).
$\tilde{\mathbf{f}}$:	Vector Description of external forcing terms.
$\mathbf{f}$:	Discretized description of external and body forces.
$\bar{f}$:	Magnitude of the time-harmonic forces.
f_x, f_y, f_z:	External forcing terms in the x, y and z direction.
g:	An arbitrary function.
$\mathbf{g}$:	Gradient, a vector of the first derivative of the error, Φ w.r.t each of the reconstruction variables.
h:	An arbitrary function.
i:	The imaginary unit, $\sqrt{-1}$.
$\hat{i}, \hat{j}, \hat{k}$:	Unit vectors in x,y and z directions respectively.
$m_1 \rightarrow m_8$:	Components of an arbitrary matrix.
$\mathbf{n}$:	Nodal material properties for linear least squares.
$\mathbf{p}$:	Search direction.
$\mathbf{p}_{SD}$:	Steepest descent search direction.
$p_1 \dots p_i \dots p_m$:	Coefficients of the $i'th$ derivative of stress w.r.t time in the constitutive equation of a spring-dashpot configuration.
$q_1 \dots q_i \dots q_m$:	Coefficients of the $i'th$ derivative of strain w.r.t time in the constitutive equation of a spring-dashpot configuration.
$\mathbf{r}_a$ & $\mathbf{r}_b$:	Arbitrary real vectors. Complex versions are $\mathbf{c}_a$ and $\mathbf{c}_b$.
$\mathbf{r}_d$:	RHS vector for direct inversion.
$\mathbf{r}_f$:	Forward FEM problem RHS vector.
$r(x)$:	Real valued amplitude of MR-detected motions.

s:	A dummy variable.
t:	Time.
$\tilde{\mathbf{u}}$:	The vector displacement (in x,y,z coordinate system).
$\hat{\mathbf{u}}$:	An approximation of the displacement.
$\mathbf{u}, \dot{\mathbf{u}}, \ddot{\mathbf{u}}$:	The discretized description of the displacement, velocity and acceleration.
$\mathbf{u_c}$:	Displacements calculated using the current θ estimate.
$\mathbf{u_m}$:	Measured displacements.
$\|u_{CD}\|$:	Modulus of complex-valued displacement amplitude (CD damping).
$\|u_{CSM}\|$:	Modulus of complex-valued displacement amplitude (CSM damping).
$\bar{\mathbf{u}}$:	Amplitude of time-harmonic motion.
u:	Displacement in the x direction.
v:	Displacement in the y direction.
$v_1 \rightarrow v_4$:	Components of arbitrary vectors.
w:	Displacement in the z direction.
$\bar{u}, \bar{v}, \bar{w}$:	Complex-valued displacement amplitude.
w_{sf}:	Weighting applied to spatial filtering.
w_g:	Weighting applied to each Gauss point.
x:	Coordinate direction.
x_g:	Position of each Gauss point.
y:	Coordinate direction.
z:	Coordinate direction.

Greek Symbols

Γ:	Boundary of Ω.
Γ_z:	Boundary of Ω_z.
Δ_θ:	Integral of a basis function over all connected elements.
Φ:	Displacement error.
Φ_p:	Relative displacement error.
Φ_{tk}:	Error function with Tikhonov regularization.
Φ_{tv}:	Error function with total variation minimization.
Ψ:	Motion difference.
Ω:	Whole problem domain.
Ω_z:	Subzone of problem domain.
α:	Step size selected by line search.
α_{tk}:	Tikhonov regularization weight.
α_{tv}:	Total variation minimization weight.
$\bar{\alpha}$:	Proportionality constant relating damping force to velocity.
α_p:	Proportionality constant of the mass matrix in a proportional damping assumption.

β:	Conjugate gradient scalar.
β_p:	Proportionality constant of the stiffness matrix in a proportional damping assumption.
γ_r	Factor added to the diagonal of $\mathbf{H}$ to improve condition.
$\gamma_{xy}, \gamma_{xz}, \gamma_{xy}$:	Shear strains in corresponding coordinate directions.
δ:	A given change in material property value.
δ_s:	The step size used for the finite difference approximation of the second derivative in the secant method.
$\epsilon_x, \epsilon_y, \epsilon_z$:	Engineering strains in corresponding coordinate directions.
$\epsilon'_x, \epsilon'_y, \epsilon'_z$:	Deviatoric strains in corresponding coordinate directions.
ϵ_0:	Amplitude of time-harmonic strain.
ζ:	Local FE coordinate corresponding to the z direction.
η:	Local FE coordinate corresponding to the y direction.
θ:	A general reconstructed variable.
θ_{sc}:	A scaled reconstructed variable.
$\boldsymbol{\theta}^*$:	Material property description corresponding to min[Φ].
λ:	First Lamé parameter, $\lambda = \frac{\nu E}{(1+\nu)(1-2\nu)}$.
λ_s:	Approximate shear wavelength.
μ:	Shear Modulus, or second Lamé parameter, $\mu = \frac{E}{2(1-\nu)}$.
μ_R:	Real part of μ.
μ_I:	Imaginary part of μ.
ν:	Poisson's ratio.
ξ:	Local FE coordinate corresponding to the x direction.
ξ_d:	Damping ratio (Eq. 2.20).
ξ_{csm}:	Fraction of ξ_d composed of complex shear modulus (Eq. 2.21).
ξ_{cd}:	Fraction of ξ_d composed of complex density (Eq. 2.22).
ρ:	Density.
ρ_R:	Real part of ρ.
ρ_I:	Imaginary part of ρ.
$\sigma_x, \sigma_y, \sigma_z$:	Engineering stresses in corresponding coordinate directions.
$\vec{\sigma}_x, \vec{\sigma}_y, \vec{\sigma}_z$:	Components of the expanded stress tensor.
$\bar{\sigma}$:	Dilatational stress.
$\sigma'_x, \sigma'_y, \sigma'_z$:	Deviatoric stresses in corresponding coordinate directions.
σ_0:	Amplitude of time-harmonic stress.
$\vec{\vec{\sigma}}$:	Isotropic stress tensor, defined in Eq. A.16.
$\hat{\vec{\vec{\sigma}}}$:	Approximation of the stress tensor.
$\tau_{xy}, \tau_{xz}, \tau_{xy}$:	Shear stresses in corresponding coordinate directions.
$\phi_1 \rightarrow \phi_{27}$:	Nodal basis functions.
$\boldsymbol{\phi}$:	Vector of all 27 nodal basis functions.
$\psi_1 \rightarrow \psi_{10}$:	Elemental basis functions.

ω:	Angular frequency of time-harmonic motion ($rad\ s^{-1}$).

Acronyms

AC1:	First Armijo condition.
AC2:	Second Armijo condition.
CD damping:	Damping resulting from a complex density.
CSM damping:	Damping resulting from a complex shear modulus.
CG:	Conjugate gradient.
DOF:	Degree of freedom.
FE:	Finite element.
FEM:	Finite element method.
GN:	Gauss-Newton.
MR:	Magnetic resonance.
MRE:	Magnetic resonance elastography.
MRI:	Magnetic resonance imaging.
PDE:	Partial differential equation.
RHS:	Right hand side.
ROI:	Region of interest.
TV:	Total variation minimization.

Chapter 1

Introduction

1.1 Breast Cancer

Cancer is one of the most significant health issues in the world, the number of cancer-related deaths is second only to heart disease in most developed countries. For women, cancer of the breast is the most common form, over 184,000 new cases, and over 40,000 breast cancer related deaths are expected in the United States in 2008 [1].

Cancer is caused by abnormal cells which do not undergo the normal process of cell death, and continue to divide, initially forming a localized group of abnormal cells (stage 1). At later stages of cancer, malignant cells can spread to other parts of the body, through a process known as metastasis. These can replace healthy cells in vital organs, inhibiting their function, and often leading to the death of the patient. Once cancer reaches this stage (stage 3), survival rates are low, therefore early detection through effective screening techniques plays a significant role in the reduction of mortality. Five year survival rates for breast cancer have been shown to reduce from around 95% for stage 1 tumors to less than 20% for stage 3 tumors [2].

1.2 Screening Techniques

Abnormal cancer cells have differing mechanical properties from the surrounding healthy tissue, most breast cancer screening techniques are based on exploiting these differences to identify tumors. Currently, the most effective method for large scale breast cancer screening is mammography [3, 4], where the breast is imaged using x-rays, and differences in x-ray attenuation, primarily caused by contrasts in density between tissue types are detected. This method is favored because of its relatively low cost, however disadvantages of this method include pain experienced as the breast is compressed to take the image [5], certain types of tumors which are undetectable by x-rays, and dif-

ficulty in interpreting the resulting images due to the sometimes low contrast between tumors and the surrounding healthy tissue [6].

Elastography is an alternative screening and diagnosis technique under development which estimates material property distributions using the mechanical response of the tissue in response to some stimulus. A large range of these stimuli have been experimented with, such as a static or quasi-static compression [7], ultrasound excitation [8], or low frequency steady-state mechanical excitation [9, 10], however Parker et. al. showed these methods all produce responses that fall within a common spectrum of elastic behavior [11]. Responses can be measured throughout the tissue using ultrasound [12], or Magnetic Resonance Imaging (MRI) [13, 14], or only on the surface of the material using digital cameras [15]. The simplest techniques involve strain estimation under compression, where the areas of higher stiffness have lower strains than softer tissue. Other techniques which produce a quantitative estimate of the material properties use a numerical model of the tissue, and look for a material property distribution which most closely reproduces the measured response data. If the model is a reasonable approximation of the true behavior of the tissue, this calculated material property distribution should be close to the actual tissue properties. This work focuses on quantitative material property estimation using MR-detected time-harmonic motion data.

Full field MR-detected motions contain large amounts of data, making it possible to reconstruct the distribution of multiple material properties from a single dataset. Obtaining the data requires the use of large and expensive machines, extracting more parameters will increase the diagnostic efficiency of an MRI scan for breast cancer detection. Currently the most effective property for diagnosis is the mechanical stiffness (either Young's or shear modulus). Contrasts of between 2 and 20 times that of healthy tissue have been reported for tumors, [16], which is far greater than the x-ray attenuation used in mammography, making it easier to differentiate between healthy and cancerous tissue. Other material parameters which have been investigated include Lamé's first parameter, λ, density, ρ [17], loss modulus [18] and anisotropic stiffness parameters [19]. The availability of additional material properties such as these could prove useful for differentiating benign and malignant tumors, reducing the number of unnecessary surgeries performed on benign lesions.

1.3 Contributions

There have been three major contributors to this MRE reconstruction code, the contribution from each person is listed here.

Hans Uwe-Berger :

- Initial implementation of undamped incompressible elasticity forward FE Problem.
- Initial implementation of undamped inverse problem, using the conjugate gradient method with Newton-Raphson Linesearch.

Elijah Van Houten :

- Restructuring initial forward and inverse problem into one program.
- Upgrade of undamped inverse problem: Gauss-Newton method, secant linesearch, gradient calculation using the adjoint method and regularization techniques added.
- Subzone implementation of Rayleigh damped inverse problem, total variation minimization and spatial filtering.
- Added ability to reconstruct bulk modulus.

Matt McGarry :

- Implementation of a Rayleigh damped material model in the forward and inverse problems. Added ability to reconstruct a nodally distributed imaginary shear modulus and complex density.
- Addition of an Armijo linesearch.
- Optimization of forward problem, adjoint method and jacobian build algorithms.
- Further restructuring of the inverse problem.
- Global implementation of the inverse problem using elemental basis functions.
- Conversion of MRI datasets to a MR-voxel based 27 node hexahedral FE mesh.
- Conversion of output FE file format to Ensight case gold format for visualization.
- Development and testing of conjugate gradient search direction scaling techniques.
- Implementation of material property bounds at the update level.
- Setting up, running and analyzing the results for all reconstructions presented in this thesis.

1.4 Thesis Overview

The primary purpose of this work is to apply a Rayleigh damping model to elastographic reconstruction. The most common damping model currently used is a viscoelastic model [20], which models damping effects as being proportional the the elastic forces within the material, and is implemented through the use of a complex shear modulus. The Rayleigh model is an extension of this model which also includes a complex density, modelling damping effects as being related to a combination of both elastic and inertial forces. Use of a Rayleigh model gives reconstructed distributions of two different damping parameters, as opposed to the single damping parameter given by viscoelastic reconstructions. Damping effects *in-vivo* occur due to complex interactions between microstructural tissue elements, so any continuum damping model can only attempt to approximate the aggregate effect of these interactions. It is hoped that a Rayleigh model will be a step towards accurate characterization of damping in human tissue, and the extra damping parameter may also prove useful for clinical diagnosis of different benign and malignant tumor types.

The majority of the work performed has been in the development of a material property reconstruction FORTRAN code, as such the majority of this thesis is devoted to an explanation of the various techniques employed, in a form that is related to the structure of the code.

Chapter 2 and the appendices cover the theory behind the various methods used in the reconstruction, such as the incompressible Rayleigh damped finite element model, optimization based reconstruction techniques, line search algorithms and regularization techniques, and are presented in a form that will hopefully make details of the actual implementation clearer for future researchers building on the current version of code.

Chapter 3 gives a brief overview of the process of MRI measurement of harmonic motions, along with details of how these measurements are converted to the form used in the reconstruction code.

Chapter 4 presents an initial investigation into how reliably differing combinations of Rayleigh damping parameters can be detected by an optimization based reconstruction algorithm, performed using reconstructions of globally defined Rayleigh damping parameters, with simulated motion data.

Chapter 5 presents distributed material property reconstructions to demonstrate that the code works. Results using simulated data are given, as well as reconstructions performed using MR-detected motions from both gelatine tissue-mimicking phantoms, as well as *in-vivo* patient data. Two different descriptions of basis functions are presented, a nodal basis, which uses the FE basis functions, and an alternative elemental basis, which describes the material properties as a general quadratic function over the element.

Chapter 2

Theory

The reconstruction code models tissue as an incompressible, Rayleigh damped elastic continuum. Details of the incompressible elasticity formulation used are given in Appendix A, and the Rayleigh damping theory is developed below in section 2.1. The theory necessary for the finite element implementation is given in Appendix B.

2.1 Rayleigh Damping

The majority of tissue damping models currently used in time-harmonic elastography consist of a viscoelastic material implemented through a complex shear modulus to model damping effects, where the level of damping is related to the elastic forces in the material [21, 18]. Rayleigh, or Proportional damping is a model which incorporates damping effects proportionally related to both elastic and inertial forces, which in the time-harmonic case can be shown to equate to both the shear modulus and density being complex parameters. The use of a complex shear modulus and density to model damping effects can be derived separately using viscoelasticity and the damped wave equation respectively, or simultaneously through the use of a proportional damping matrix in a discretized dynamic system description.

2.1.1 Complex Modulus from Viscoelastic Theory

A viscoelastic material is modelled as a combination of springs and dashpots in series and parallel. The configuration of a three-parameter solid is shown in Fig. 2.1, and will be used as an example in this section.

The constitutive equation of a combination of springs and dashpots arranged in this manner can be written as:

$$p_0\sigma + p_1\frac{d\sigma}{dt} + p_2\frac{d^2\sigma}{d^2t} + \cdots + p_m\frac{d^m\sigma}{d^mt} = q_0\epsilon + q_1\frac{d\epsilon}{dt} + q_2\frac{d\epsilon^2}{d^2t} + \cdots + q_n\frac{d\epsilon^n}{d^nt}, \qquad (2.1)$$

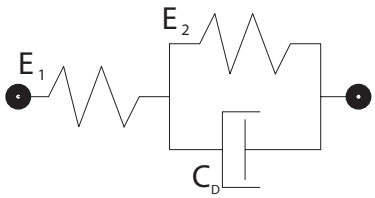

Figure 2.1 Configuration of a one-dimensional three-parameter solid viscoelastic element, with elastic elements E_1 and E_2, and a viscous dashpot, C_D

or

$$\sum_{j=0}^{m} p_j \frac{d^j \sigma}{d^j t} = \sum_{k=0}^{n} q_k \frac{d\epsilon^k}{d^k t}, \tag{2.2}$$

where σ represents the stress in the element, ϵ the strain, and p_i and q_i the constants for the respective derivatives (these are determined by properties and configuration of elements in the model). For example, the behavior of the three-parameter solid from Fig. 2.1 is given by:

$$(E_1 + E_2)\sigma + C_D \frac{d\sigma}{dt} = E_1 E_2 \epsilon + E_1 C_D \frac{d\epsilon}{dt}, \tag{2.3}$$

where E_1, E_2 and C_D are the spring and dashpot constants from Fig. 2.1. If a viscoelastic material is subjected to an oscillatory strain of the form $\epsilon = \epsilon_0 e^{i\omega t}$, where ω is the frequency and t is the time variable, Eq. 2.2 gives a stress of the same form, $\sigma = \sigma_0 e^{i\omega t}$. Substituting these stress and strain relations into Eq. 2.2 gives:

$$\sigma_0 \sum_{j=0}^{m} p_j (i\omega)^j e^{i\omega t} = \epsilon_0 \sum_{k=0}^{n} q_k (i\omega)^k e^{i\omega t}, \tag{2.4}$$

$$\sigma_0 = \left[\frac{\sum_{k=0}^{n} q_k (i\omega)^k}{\sum_{j=0}^{m} p_j (i\omega)^j} \right] \epsilon_0 \tag{2.5}$$

From Eq. 2.5, it can be seen that σ_0 is complex, and is related to ϵ_0 by the complex modulus,

$$E^* = \frac{\sum_{k=0}^{n} q_k (i\omega)^k}{\sum_{j=0}^{m} p_j (i\omega)^j}. \tag{2.6}$$

For example, the complex modulus of the 3 parameter solid is given by:

$$E^* = \frac{E_1 E_2 + i\omega E_1 C_D}{E_1 + E_2 + i\omega C_D}. \tag{2.7}$$

Expansion of this analysis into multiple dimensions gives the Correspondence Principle [20], which states that the viscoelastic solution of a time-harmonic problem can be obtained from the elastic solution by replacing the elastic modulus with the corresponding

complex modulus. For a more complete treatment of viscoelasticity, see [20] and [22].

2.1.2 Complex Density From The Damped Wave Equation

Navier's equation in one dimension with a damping force proportional to the velocity is given by

$$\nabla \cdot \mu \nabla \tilde{\mathbf{u}} + \nabla(\lambda + \mu)\nabla \cdot \tilde{\mathbf{u}} = \rho \frac{\partial^2 \tilde{\mathbf{u}}}{\partial t^2} + \bar{\alpha} \frac{\partial \tilde{\mathbf{u}}}{\partial t}. \tag{2.8}$$

Here, the real valued material parameters μ, ρ and λ are the shear modulus, density and first Lamé coefficient respectively, $\bar{\alpha}$ is the real valued damping proportionality constant and $\tilde{\mathbf{u}}$ is the displacement. Assuming steady state motion of the form $\tilde{\mathbf{u}} = \bar{\mathbf{u}}(x)e^{i\omega t}$ gives

$$\nabla \cdot \mu \nabla [\bar{\mathbf{u}}(x)e^{i\omega t}] + \nabla(\lambda + \mu)\nabla \cdot [\bar{\mathbf{u}}(x)e^{i\omega t}] = [i\bar{\alpha}\omega \bar{\mathbf{u}}(x) - \rho\omega^2 \bar{\mathbf{u}}(x)]e^{i\omega t}. \tag{2.9}$$

Likewise substituting a complex density of the form $\rho = \rho_R + i\rho_I$ into the undamped form of Navier's equation:

$$\nabla \cdot \mu \nabla \tilde{\mathbf{u}} + \nabla(\lambda + \mu)\nabla \cdot \tilde{\mathbf{u}} = \rho \frac{\partial^2 u}{\partial t^2}, \tag{2.10}$$

yields

$$\nabla \cdot \mu \nabla [\bar{\mathbf{u}}(x)e^{i\omega t}] + \nabla(\lambda + \mu)\nabla \cdot [\bar{\mathbf{u}}(x)e^{i\omega t}] = [-\rho_R\omega^2 \bar{\mathbf{u}}(x) - i\rho_I\omega^2 \bar{\mathbf{u}}(x)]e^{i\omega t}, \tag{2.11}$$

which is equivalent to Eq. 2.9 when

$$\rho_I = -\frac{\bar{\alpha}}{\omega}. \tag{2.12}$$

2.1.3 Proportional/Rayleigh Damping

The discretized form of Navier's equation with damping can be written as:

$$\mathbf{M_m}\ddot{\mathbf{u}} + \mathbf{C_m}\dot{\mathbf{u}} + \mathbf{K_m}\mathbf{u} = \mathbf{f}, \tag{2.13}$$

where $\mathbf{M}, \mathbf{C}$ and $\mathbf{K}$ are the mass, damping and stiffness matrices respectively, $\mathbf{u}$ is the displacement vector and $\mathbf{f}$ is the discretized description of external and body forces acting on the system. Assuming steady state motion of the form $\mathbf{u} = \bar{\mathbf{u}}e^{i\omega t}$, with $\mathbf{f} = \bar{\mathbf{f}}e^{i\omega t}$, gives:

$$(-\omega^2 \mathbf{M_m} + i\omega \mathbf{C_m} + \mathbf{K_m})\bar{\mathbf{u}} = \bar{\mathbf{f}}. \tag{2.14}$$

Implementation of a proportional damping assumption, $\mathbf{C_m} = \alpha_p \mathbf{M_m} + \beta_p \mathbf{K_m}$, with proportionality constants $\alpha_p > 0$ and $\beta_p > 0$ leads to:

$$\left[-\omega^2 \left(1 - \frac{i\alpha_p}{\omega}\right) \mathbf{M_m} + (1 + i\omega\beta_p)\, \mathbf{K_m}\right] \bar{\mathbf{u}} = \bar{\mathbf{f}}. \tag{2.15}$$

All terms in $\mathbf{M_m}$ contain the density, ρ, and all terms in $\mathbf{K_m}$ contain the shear modulus, μ, so these parameters can be moved outside the matrices, giving:

$$\left[-\omega^2 \left(\rho - \frac{i\alpha_p \rho}{\omega}\right) \mathbf{M'_m} + (\mu + i\omega\beta_p\mu)\, \mathbf{K'_m}\right] \bar{\mathbf{u}} = \bar{\mathbf{f}}. \tag{2.16}$$

Where $\mathbf{M'_m}$ and $\mathbf{K'_m}$ are the normalized mass and stiffness matrices respectively. Eq. 2.16 shows that the proportional damping model can be implemented in this case using a complex density, $\rho = \rho_R + i\rho_I$ and a complex shear modulus, $\mu = \mu_R + i\mu_I$, where:

$$\rho_R = \rho, \; and \; \rho_I = \frac{-\alpha_p \rho}{\omega} \tag{2.17}$$

$$\mu_R = \mu, \; and \; \mu_I = \omega\beta_p\mu. \tag{2.18}$$

Equation 2.17 is of the same form as Eq. 2.12, with $\bar{\alpha} = \rho\alpha_p$. The damping ratio, ξ_d, given by [23] as

$$\xi_d = \frac{1}{2}\left(\frac{\alpha_p}{\omega} + \beta_p\omega\right), \tag{2.19}$$

can be rewritten using Eqs. 2.18 and 2.17 as:

$$\xi_d = \frac{1}{2}\left(\frac{-\rho_I}{\rho_R} + \frac{\mu_I}{\mu_R}\right). \tag{2.20}$$

The damping ratio is often multiplied by 100 and expressed as a percentage. It is important to consider the signs in Eqs. 2.17, 2.18 and 2.20. In order to have realistic behavior, the imaginary density must be negative and the imaginary shear modulus positive. Equation 2.20 then predicts increasing the magnitude of either damping parameter will increase the level of damping as expected.

The combination of Rayleigh parameters which make up the damping ratio, referred to as the Rayleigh composition, can be defined as either the fraction complex shear modulus, ξ_{CSM}:

$$\xi_{CSM} = \frac{-\mu_I}{2\mu_R\xi_d}, \tag{2.21}$$

or the fraction complex density, ξ_{CD}:

$$\xi_{CD} = \frac{-\rho_I}{2\rho_R\xi_d}. \tag{2.22}$$

2.2 Material Property Support

The usual method of defining a material property distribution in the finite element method is to use the same nodal basis functions as the displacements. This is referred to as a 'nodal basis', and can be shown to lead to varying sensitivity of the displacements to changes in material property value for different types of node in higher order elements. An alternative is an 'elemental basis', where the material properties are defined as a general polynomial over each element.

2.2.1 Nodal Basis

A nodally distributed material property description is implemented by using the FE basis functions for the element, $\phi_1 \rightarrow \phi_{27}$, to describe the distribution across the domain, so that

$$\theta(\xi,\eta,\zeta) = \sum_{k=1}^{27}(\theta_k\phi_k(\xi,\eta,\zeta)), \tag{2.23}$$

where $\theta(\xi,\eta,\zeta)$ is the material property value at a point (ξ,η,ζ), ϕ_k is the FE basis function associated with the k'th node, given by Eq. B.3, and θ_k is the material property value at node k.

This description shares the properties of the FE basis functions, so it is a continuous, elementally piecewise tri-quadratic function across the whole problem domain, with discontinuous first derivatives across element boundaries. It have the advantage of being relatively simple to implement, as no new basis functions need to be defined, and all that needs to be stored is a list of material property values at each node. Display of results is also simple, as each nodal point has a corresponding material property value.

A major issue with this form of material property support is the differing sensitivities for each 'type' of node. The average magnitude of the error gradient terms, $\frac{\partial\Phi}{\partial\theta_i}$, is highly dependent on the location of the node in the element. The center nodes have the highest sensitivity, followed by mid-face, then mid-edge and finally the corner nodes are the least sensitive. This is because there are different types of nodal basis function corresponding to each type of node. Basis functions for a corner, mid-edge, mid face and center node respectively are given in Eq. 2.24.

$$\phi_1 = \frac{\xi}{2}(\xi-1)\frac{\eta}{2}(\eta-1)\frac{\zeta}{2}(\zeta-1) \tag{2.24a}$$

$$\phi_5 = (1+\xi)(1-\xi)\frac{\eta}{2}(\eta-1)\frac{\zeta}{2}(\zeta-1) \tag{2.24b}$$

$$\phi_9 = (1+\xi)(1-\xi)(1+\eta)(1-\eta)\frac{\zeta}{2}(\zeta-1) \tag{2.24c}$$

$$\phi_{27} = (1+\xi)(1-\xi)(1+\eta)(1-\eta)(1+\zeta)(1-\zeta). \tag{2.24d}$$

The total change in material property with a change nodal value is indicated by the integral of the corresponding basis function over all connected elements.

$$\Delta_\theta(\text{corner}) = \int_{-1}^{1}\int_{-1}^{1}\int_{-1}^{1} \phi_1 \mathrm{d}\xi\mathrm{d}\eta\mathrm{d}\zeta \times 8 = 1 \tag{2.25a}$$

$$\Delta_\theta(\text{mid-edge}) = \int_{-1}^{1}\int_{-1}^{1}\int_{-1}^{1} \phi_5 \mathrm{d}\xi\mathrm{d}\eta\mathrm{d}\zeta \times 4 = 1.33 \tag{2.25b}$$

$$\Delta_\theta(\text{mid-face}) = \int_{-1}^{1}\int_{-1}^{1}\int_{-1}^{1} \phi_9 \mathrm{d}\xi\mathrm{d}\eta\mathrm{d}\zeta \times 2 = 1.78 \tag{2.25c}$$

$$\Delta_\theta(\text{center}) = \int_{-1}^{1}\int_{-1}^{1}\int_{-1}^{1} \phi_{27} \mathrm{d}\xi\mathrm{d}\eta\mathrm{d}\zeta \times 1 = 2.37. \tag{2.25d}$$

The sensitivity of the displacement error, Φ, to changes in each nodal material property value will be proportional to the total change in material property solution. Analysis of some typical gradient results reveals the square of these values are similar to the relative sizes of the gradient terms for each type of node seen in practice.

Node type	Δ_θ^2	Relative Average gradient term
Corner	1	1
Mid-edge	1.77	1.95
Mid-face	3.16	3.79
Center	5.62	7.16

This type of mesh-dependent sensitivity is not desirable behavior, Fig. 2.2 shows the pattern that can appear in the material property image, especially in earlier iterations. This patterning become less evident as the iterations progress and the material property values approach their true values, although this can take a long time.

2.2.2 Elemental Basis

A different set of basis functions, where the material property distribution is described quadratically over each element is proposed to alleviate the problem of differing nodal sensitivities discussed in section 2.2.1. The elemental basis material property variation across an element is given by:

$$\theta(\xi,\eta,\zeta) = c_1 + c_2\xi + c_3\eta + c_4\zeta + c_5\xi\eta + c_6\xi\zeta + c_7\eta\zeta + c_8\eta^2 + c_9\eta^2 + c_{10}\zeta^2. \tag{2.26}$$

This elemental description allows discontinuities between elements, which may be an advantage in reconstructions as discontinuities at boundaries between different tissue types are expected.

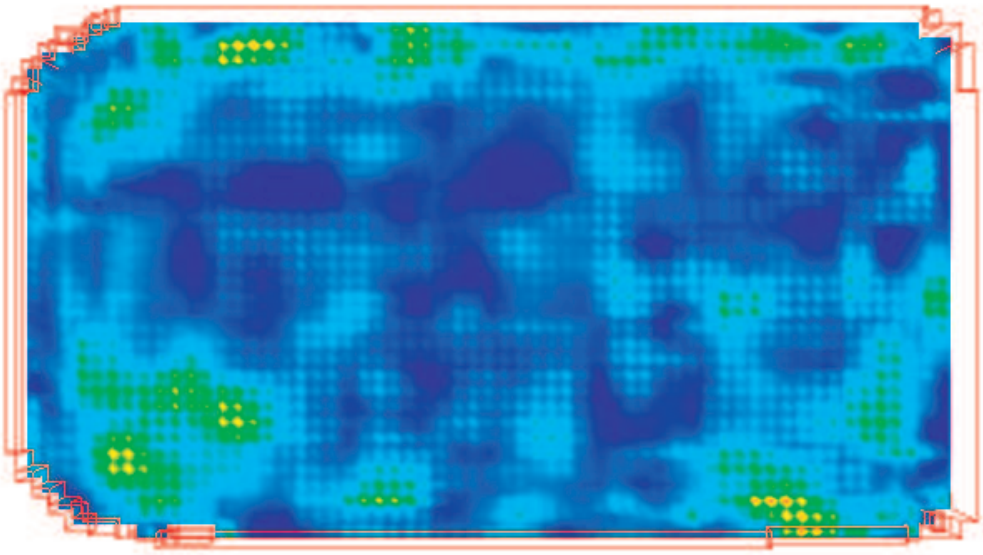

Figure 2.2 Example of patterning due to differences in parameter sensitivity for different types of nodes in the nodal basis functions.

The quadratic nodal basis functions used in in Eq. 2.23 can represent any elementally-piecewise, continuous tri-quadratic function across a mesh. The elemental basis functions in Eq. 2.26 can represent any elementally-piecewise tri-quadratic function across the mesh, without the requirement of continuity across element boundaries. This means the set of functions the nodal basis can represent are a subset of the larger set of functions that the elemental basis can represent, therefore supporting the material property variation on the elemental basis should be more versatile than using the nodal basis.

2.2.2.1 Implementation

A reconstruction code with material property variation supported on elemental basis functions was created by modifying the existing nodal basis code. At the time of writing, this implementation is not subzone-based and no regularization techniques are used, further work will be required to gain the benefits provided by subzone implementation and regularization. Most of the methods remain the same as the nodally distributed material property implementation, a description of any elemental basis specific techniques is given below.

The elemental basis functions are simply an extension of the basis functions used to support the pressure (see Appendix B), so the same symbol, ψ, is used, giving the 10 elemental basis function needed for a general tri-quadratic variation across the element as

$$\begin{aligned}
\psi_1 &= 1 \\
\psi_2 &= \xi \\
\psi_3 &= \eta \\
\psi_4 &= \zeta \\
\psi_5 &= \xi\eta \\
\psi_6 &= \xi\zeta \\
\psi_7 &= \eta\zeta \\
\psi_8 &= \xi^2 \\
\psi_9 &= \eta^2 \\
\psi_{10} &= \zeta^2.
\end{aligned} \tag{2.27}$$

Different types of material properties can be given different order support by truncating the function given in Eq. 2.26 after the constant terms for a piecewise constant distribution, or after the linear terms for a piecewise tri-linear distribution, leading to the dynamic basis statement,

$$\theta(\xi, \eta, \zeta) = \sum_{k=1}^{N_{pv}} c_k \psi_k, \tag{2.28}$$

where c_k is a proportionality constant for the k'th basis function, and N_{pv} is the number of parameters used to support each variable type. In the current elemental basis reconstruction code, shear modulus and density can be supported either as a constant, tri-linear or tri-quadratic function over each element, and bulk modulus is constant across each element. For a dynamic basis approach, the N_{pv} parameter can be increased as the iterations progress, so the first few iterations can use a reduced order constant or linear basis, and later iterations can use higher order quadratic basis functions. The most obvious advantage of this approach is the reduced size of the inversion problem for earlier iterations, however the implicit regularization resulting from the reduced problem dimensions may also increase reliability [24].

The constants, c_k, for each material property type are stored for each element to define the variation of all three material properties across the domain. The terms in the FE stiffness matrix are linear in each c_k, so the matrix can be differentiated with respect to these constants in the same way as the nodal material property values in the nodal basis approach.

Applying material property bounds becomes more complicated because the stored values do not represent the material property values directly, instead they represent constants which define the variation across the element. This problem can be dealt with by calculating the value of each material property at all 27 nodes within the element using Eq. 2.26, applying the bounds to these values, then using a linear least squares approach to find new values for the elemental basis constants to best fit the values

at the nodes after the bounds have been applied. Applying the linear least squares method [25] involves solving the system

$$\mathbf{X}^H\mathbf{X}\mathbf{c} = \mathbf{X}\mathbf{n} \tag{2.29}$$

for each variable type in each element, where $\mathbf{X}$ is a $27 \times N_{pv}$ matrix containing the N_{pv} elemental basis function values at each of the 27 nodes, so that X_{ij} is the value of the j'th elemental basis function at the i'th node, $\mathbf{c}$ is a $N_{pv} \times 1$ vector of the new elemental basis constants to be determined, and $\mathbf{n}$ is the value of the material property at each node after the bounds have been applied. This technique needs to be applied at the subzone level (as discussed in section 2.3.6), because applying it at the material property update level leads to a change in the effective search direction, which affects the linesearch techniques. No 'easy fix' is possible as in the nodal basis case.

Display of results also becomes more complicated because the material property value is not unique at each node. To avoid this issue, the material property values are displayed at a selection of internal points (currently the gauss points and points very close the the element boundaries). These values are uniquely defined, so can be easily displayed and analyzed.

2.3 Inverse Problem

Finding the mechanical properties of an object given the mechanical response is known as the *inverse problem*, this section covers the optimization-based techniques used to solve the inverse problem in the reconstruction code.

The forward problem is defined as:

> Find the mechanical response, $\mathbf{u}$, given the material property distribution, $\boldsymbol{\theta}$, and boundary condition data.

The inverse problem can then be defined as:

> Find the material property distribution, $\boldsymbol{\theta}$, given the mechanical response, $\mathbf{u}$, and boundary condition data.

The size of these inverse problems are defined by the number of observed measurements, NO, and the number of parameters being reconstructed, NP. In the case of MRE, NO is the number of measured displacements, and NP is the number of parameters required to define the material property distribution. The inverse problem can be solved by direct inversion of the elasticity equation (Eq. A.23), provided there are at least as many measurements as parameters being solved for, i.e. $NO \geq NP$. This involves a reformulation of the forward problem,

$$\mathbf{A}(\boldsymbol{\theta})\mathbf{u} = \mathbf{r}_f, \tag{2.30}$$

where $\mathbf{A}(\boldsymbol{\theta})$ is the forward FE matrix containing terms dependent on the material properties, $\boldsymbol{\theta}$, $\mathbf{u}$ are the unknown displacements, and $\mathbf{r}_f$ is the RHS vector for the forward problem (see Appendix B), so that the material properties are the unknowns, and the displacements are known values, i.e.

$$\mathbf{G}(\mathbf{u})\boldsymbol{\theta} = \mathbf{r}_d. \tag{2.31}$$

Here, the matrix $\mathbf{G}(\mathbf{u})$ has terms containing the known (MR-detected) displacements, and $\mathbf{r}_d$ is the direct inversion RHS vector. The system can then be solved for the unknown material properties, $\boldsymbol{\theta}$, using any standard linear equation solver. In an MRI scan, complex values of all three motion components are measured, which should allow up to three different complex material property distributions to be solved for using direct inversion. However, the direct inversion problem is highly ill-conditioned, and very sensitive to measurement noise, therefore data regularization techniques are required in practice, which may result in the loss of some information [21].

The method used in the reconstruction code involves an optimization based approach, which is far more robust to measurement noise. This involves finding a material property distribution, $\boldsymbol{\theta}^*$ that minimizes an error metric, Φ:

$$\boldsymbol{\theta}^* = \arg\min_{\boldsymbol{\theta}}[\Phi]. \tag{2.32}$$

The real-valued displacement error, Φ is given by

$$\Phi = \frac{1}{2}(\mathbf{u}_c - \mathbf{u}_m)^H(\mathbf{u}_c - \mathbf{u}_m), \tag{2.33}$$

where $\mathbf{u}_c$ is the set of motions calculated using an estimate of the material property distribution, $\mathbf{u}_m$ is the measured motion input data, and the superscript H denotes the complex conjugate transpose. This method also has the advantage that it is feasible to solve for more material property values than there are measurements, so effects such as material non-linearity and anisotropy can be considered. However, the iterative nature of optimization techniques results in extremely computationally intensive problems. Many solutions of the forward problem are required to reach the minimum of Eq. 2.33.

Most optimization algorithms are iterative solution techniques, where each iteration can be broken down into two steps. The first step involves selecting a material property 'search direction' for each iteration, $\mathbf{p}_k$, which is used to update the material property description, $\boldsymbol{\theta}$, at each iteration so that the update for the k'th iteration is given by

$$\boldsymbol{\theta}_{k+1} = \boldsymbol{\theta}_k + \alpha_k \mathbf{p}_k, \tag{2.34}$$

where α_k is some step size to be determined. Because these are minimization techniques, restrictions are usually placed on the search direction to ensure some reduction

in error is achieved with each iteration. Some reduction in error is assured at small α_k values if the directional derivative of the error along $\mathbf{p}_k$ is negative, i.e.

$$\mathfrak{Re}\{\mathbf{p}_k^H \mathbf{g}_k\} < 0, \tag{2.35}$$

where $\mathbf{g}_k$ is the current error gradient, $\frac{\mathbf{d}\Phi}{\mathbf{d}\theta}$.

The second step involves selecting a value for α_k in Eq. 2.34. The error domain along the search direction is one dimensional, so can be represented by a line, therefore this step is often called a linesearch. An exact linesearch is where an actual minima in the direction given by $\mathbf{p}_k$ is found, so that

$$\mathfrak{Re}\{\Phi(\boldsymbol{\theta}_k + \alpha_k \mathbf{p}_k)^H \mathbf{g}\} = 0. \tag{2.36}$$

Exact searches can be computationally intensive and sometimes unreliable, so inexact linesearches are sometimes used. These use simple and reliable methods to find a value for α_k which satisfies some descent criteria, such as

$$\Phi(\boldsymbol{\theta}_k + \alpha_k \mathbf{p}_k) < f(\boldsymbol{\theta}_k). \tag{2.37}$$

Although an α_k selected in this way is unlikely to be the optimal value producing the greatest reduction in error, the low computational cost allows more optimization iterations to be completed in a given time, therefore the efficiency of an algorithm with a fast, inexact linesearch could be better than an algorithm with a slower, exact linesearch.

Details of specific techniques used for both of these steps are covered in the next two subsections.

2.3.1 Conjugate Gradient (CG) Method

The conjugate gradient (CG) method [26] is a modification of the simple steepest descent method to make it more efficient. The steepest descent method involves selecting a search direction which is the negative of the gradient, ie:

$$\mathbf{p}_{sd} = -\frac{d\Phi}{d\boldsymbol{\theta}}. \tag{2.38}$$

The gradient is the direction of steepest increase in error values, so the negative of this is the direction of steepest decrease, hence the name 'Steepest Descent'. Although simple in principle, this method suffers from very slow convergence in practice. CG methods improve on steepest descent by building up a set of search directions from the gradient at each iteration, which eventually form a conjugate basis set. For linear problems, an optimization problem involving NP parameters will completely converge in NP iterations. Elastography problems are non-linear, so this N-step superlinear

convergence is not achieved, and the large number of reconstructed parameters also mean it is not feasible to run NP iterations. However, even with a smaller number of iterations, selection of search direction using CG methods is more efficient than using steepest descent methods, and has a similar low computational cost per iteration.

CG is implemented by building the next search direction using a linear combination of the current gradient, $\mathbf{g}_k$, and the previous search direction, $\mathbf{p}_{k-1}$. This gives

$$\mathbf{p}_k = -\mathbf{g}_k + \beta_k \mathbf{p}_{k-1}. \tag{2.39}$$

The constant β_k is selected in such a way that $\mathbf{p}_k$ forms a part of the conjugate basis set that is eventually formed after NP CG iterations. Several formulations exist, the most commonly used is the Polak-Ribére formula [27], given by

$$\beta_k = \max[\frac{\mathfrak{Re}\{\mathbf{g}_k^H(\mathbf{g}_k - \mathbf{g}_{k-1})\}}{\mathfrak{Re}\{\mathbf{g}_{k-1}^H \mathbf{g}_{k-1}\}}, 0]. \tag{2.40}$$

Because the elastographic inverse problem is non-linear, the search directions will lose conjugacy as the iterations progress, therefore CG reconstructions often perform better with periodic 'restarts', where building up the set of conjugate search directions is started from scratch. This is achieved by simply setting $\beta_k = 0$. The only information with significant storage required for a CG algorithm are 4 vectors of length NP, $\mathbf{g}_k, \mathbf{g}_{k-1}, \mathbf{p}_k$ and $\mathbf{p}_{k-1}$. This results in CG being very memory efficient compared with Newton type methods, which require storage of an $NP \times NP$ Hessian matrix. The computational intensity of CG is also very low, due to the simple vector-vector operations it requires. Basic Pseudocode for calculation of the next CG search direction is given in Algorithm 2.1.

Algorithm 2.1: Pseudocode for calculation of the unscaled conjugate gradient search direction.

Input: Current Gradient, $\mathbf{g}_k$, Previous gradient, $\mathbf{g}_{k-1}$, Previous Search Direction, $\mathbf{p}_{k-1}$, Iteration number, k, CG Restart indicator, $rstrt$
Output: New Search direction, $\mathbf{p}_k$
if $k = 1$ *or* $rstrt = true$ **then**
  $\beta_k = 0$
else
  $\beta_k = \max[\frac{\mathfrak{Re}\{\mathbf{g}_k^H(\mathbf{g}_k - \mathbf{g}_{k-1})\}}{\mathfrak{Re}\{\mathbf{g}_{k-1}^H \mathbf{g}_{k-1}\}}, 0]$
end
$\mathbf{p}_k = -\mathbf{g}_k + \beta_k \mathbf{p}_{k-1}$;

2.3.1.1 Scaling of CG Search Direction

The CG search direction is built up from a linear combination of all the previous gradient values, so it's size is determined by the size of the gradient terms. The size of

these gradient terms, $\frac{\partial \Phi}{\partial \theta_i}$, is dependent on several factors, which do not contribute to a well-scaled search direction.

The forward difference approximation of the gradient term for a particular reconstructed parameter, θ_i is given by

$$\frac{\partial \Phi}{\partial \theta_i} \approx \frac{\Phi(\theta_i + \delta) - \Phi(\theta_i)}{\delta} \tag{2.41}$$

Equation 2.33 indicates the error sizes, $\Phi(\boldsymbol{\theta})$, are dependent on the size of the motion amplitudes, $\mathbf{u}_m$ and $\mathbf{u}_c$. The motion amplitudes should have no effect on the material property solution when using a linear elastic model, however larger motion amplitudes will lead to larger gradient terms, hence larger CG search directions. Linesearch techniques perform best when the α_k selected is as close as possible to 1, so if no scaling of the CG search direction is used, the efficiency of the linesearch will be reduced because differing α_k values will be selected by the linesearch techniques depending on the motion amplitudes.

If a material property, θ_i has a large value, such as the bulk modulus terms for a nearly incompressible material, the corresponding gradient terms are usually small because in general, a given absolute change, δ in a large parameter will have a smaller effect on the solution than the same δ applied to a smaller-valued parameter. Eq. 2.41 shows this will result in small gradient values, hence small CG updates for large parameters, and comparatively large updates for small parameters, resulting in very little relative change in these large parameters compared to the smaller ones.

In order to produce a well-scaled search direction, some method of scaling the CG search direction is required. This is complicated by the fact that a search direction may contain terms for different material property types. Scaling each material property type separately is possible in CG because it is equivalent to multiplying the search direction by a diagonal scaling matrix, $\mathbf{D}_s$. Three different scaling techniques were trialled in the reconstruction code, a description of each and the resulting performance is given below.

The first method involves scaling the search direction terms for each parameter type so that a given step size produces, on average, the same relative change in each parameter type, i.e.

$$\sum |\mathbf{p}_t^s| = \delta_t \sum |\boldsymbol{\theta}_t|, \tag{2.42}$$

where the subscript t indicates only the terms corresponding to a particular material property type, $\mathbf{p}_t^s$ contains the scaled search direction terms, $\boldsymbol{\theta}_t$ are the material property description terms, and δ_t is an adjustable parameter set to a value that allows the linesearch methods to work efficiently. This gives the first scaling equation for each variable type as

$$\mathbf{p}_t^s = \delta_t \frac{\sum |\boldsymbol{\theta}_t|}{\sum |\mathbf{p}_t|} \cdot \mathbf{p}_t, \tag{2.43}$$

where $\mathbf{p}_t^s$ and $\mathbf{p}_t$ are the scaled and unscaled CG search direction respectively.

The second scaling technique looks to scale the search direction terms for different material property types in such a way that each has the same effect on the displacement. The effect each material property type has on the solution is quantified using the change in displacement, u, that occurs with a global change in each parameter type, θ_t, i.e. the 'global jacobian size', $|J_g|_t$,

$$|J_g|_t = \sqrt{\frac{\partial \mathbf{u}}{\partial \theta_t}^H \frac{\partial \mathbf{u}}{\partial \theta_t}}. \tag{2.44}$$

Section 2.3.2 deals with a method of calculating $\frac{\partial \mathbf{u}}{\partial \theta_t}$. The size of the effect each material property type is to have on the displacements is set by enforcing a given relative change in μ. This produces the second scaling equation

$$\mathbf{p}_t^s(k) = \delta_\mu \frac{\sum |\boldsymbol{\mu}|}{\sum |\mathbf{p}_\mu|} \cdot \frac{|J_g|_\mu}{|J_g|_t} \cdot \mathbf{p}_t(k), \tag{2.45}$$

where δ_μ is the specified relative change in μ, $\boldsymbol{\mu}$ is the vector of μ terms, $\mathbf{p}_\mu$ is the vector of μ search direction terms, and $|J_g|_\mu$ and $|J_g|_t$ are the global jacobian sizes for μ,and the parameter type being scaled, t, respectively.

A modification to the second method gives rise to the third. The performance of the second method can suffer if a particular material property type does a poor job of reducing the error compared to the others. As the iterations progress, the size of the search direction terms will reduce more for terms which give the greatest error reduction, due to a reduction in their corresponding gradient terms, leading to the displacement change being dominated by terms which produce poor error reduction. To alleviate this problem, the CG search direction is scaled by the ratio of the global Jacobian to the residual size. This ratio can be thought of as an indication of how well a given displacement change from a particular material property type can reduce the error. The third scaling equation is given by:

$$\mathbf{p}_t^s(k) = \delta_\mu \frac{\sum |\boldsymbol{\mu}|}{\sum |\mathbf{p}_\mu|} \cdot \frac{|J_g|_\mu}{|J_g|_t} \cdot \frac{|g|_t}{|g|_\mu} \mathbf{p}_t(k), \tag{2.46}$$

where $|g|_\mu$ and $|g|_t$ are the sizes of the gradient terms for μ and the material property type being scaled, t, respectively.

These scaling factors are all calculated at the first iteration and held constant for subsequent iterations, so that the reduction in gradient size that occurs as iterations progress takes care of reducing the size of the updates as the algorithm approaches the minimum error solution.

A comparison of the error reduction for the three scaling techniques is given in Fig. 2.3. The third method gives the greatest reduction in error at all iterations, so is the

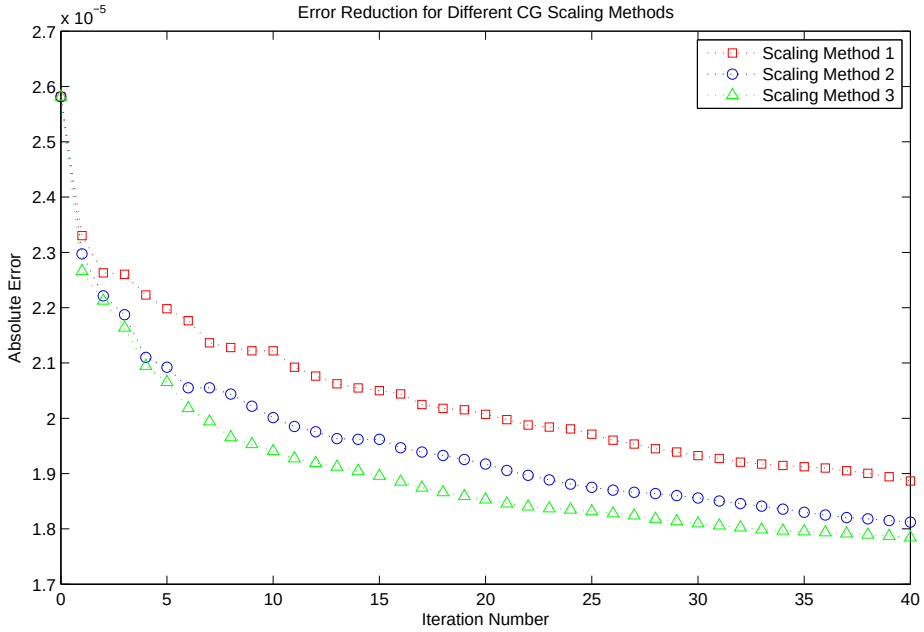

Figure 2.3 Error Reduction of each CG scaling technique, reconstructing $\mathfrak{Re}\{\mu\}$, $\mathfrak{Im}\{\mu\}$ and $\mathfrak{Im}\{\rho\}$ for a 1331 node subsection of a gelatine phantom. Details of each scaling technique are given in section 2.3.1.

method currently used in the reconstruction code, although the code structure for the other methods is left intact should they become useful for future work.

2.3.1.2 Adjoint Gradient Calculation

The CG method requires only gradient information to calculate the search direction, and the adjoint method provides a very efficient method of obtaining it. Only two forward solves are required to calculate a gradient for any number of reconstructed parameters, whereas alternative techniques such as using the Jacobian matrix or a finite difference approximation require as many forward solves as there are parameters.

The derivation of the adjoint method is much more complicated than its implementation. Refer to [28, 29, 30] for details of the derivation for real valued parameters, following these derivations using complex parameters gives the steps required for implementing the adjoint method for Rayleigh damped reconstructions as:

1. Solve the forward problem for $\mathbf{u}_c$, the current displacement solution, using the current material property estimate.

2. Calculate the 'adjoint forcing', which is given by $\overline{(\mathbf{u}_c - \mathbf{u}_m)}$, where $\mathbf{u}_m$ is the vector of measured displacements, and the overbar represents the complex con-

jugate. Therefore the adjoint forcing is the conjugate of the difference between the current displacement estimate and the measured displacement.

3. Solve the forward problem again with the adjoint forcing as the RHS vector, to obtain the adjoint solution, $\mathbf{u}_a$.

4. Calculate the i'th term in the gradient, g_i, using

$$g_i = \overline{\left(\frac{\partial \mathbf{A}}{\partial \theta_i}\mathbf{u}_a\right)^T \mathbf{u}_c}, \tag{2.47}$$

where $\frac{\partial \mathbf{A}}{\partial \theta_i}$ represents the forward FE matrix differentiated with respect to the i'th material property value.

The adjoint method will calculate the true value of the gradient, a comparison of the adjoint-calculated gradient with a finite difference approximation is given in figure 2.4

2.3.2 Gauss-Newton Method

The Gauss-Newton (GN) method usually converges in fewer iterations than CG methods because it utilizes second derivative information. This information is computationally intensive to calculate, and memory intensive to store, limiting the sizes of problems to which the method can be applied. However, through the use of the subzone method, GN has proven successful in previous work [9], so is included as an option in the reconstruction code.

The Gauss-Newton method is derived [31] using the second order Taylor series approximation of the error function:

$$\Phi(\boldsymbol{\theta} + \mathbf{p}) = \Phi(\boldsymbol{\theta}) + \Re\mathfrak{e}\{\mathbf{p}^H\mathbf{g}\} + \Re\mathfrak{e}\{\mathbf{p}^H\mathbf{H_e}\mathbf{p}\} + \mathrm{O}(\mathbf{p}^3). \tag{2.48}$$

Here, $\mathbf{p}$ is some distance away from the current material property estimate, $\boldsymbol{\theta}$, $\mathbf{g}$ is the gradient vector whose terms are given by $g_i = \frac{\partial \Phi}{\partial \theta_i}$, and $\mathbf{H_e}$ is the exact Hessian matrix of second derivatives, whose terms are given by $H_e(ij) = \frac{\partial^2 \Phi}{\partial \theta_i \partial \theta_j}$. Differentiating Eq. 2.65 with respect to $\mathbf{p}$ leads to

$$\frac{\partial \Phi(\boldsymbol{\theta} + \mathbf{p})}{\partial \mathbf{p}} = \mathbf{g} + \mathbf{H_e}\mathbf{p} + \mathrm{O}(\mathbf{p}^2). \tag{2.49}$$

Setting this equation to zero, and solving for the step size, $\mathbf{p}$, which will minimize the second order approximation of Φ gives

$$\mathbf{p} = -\mathbf{H_e}^{-1}\mathbf{g}. \tag{2.50}$$

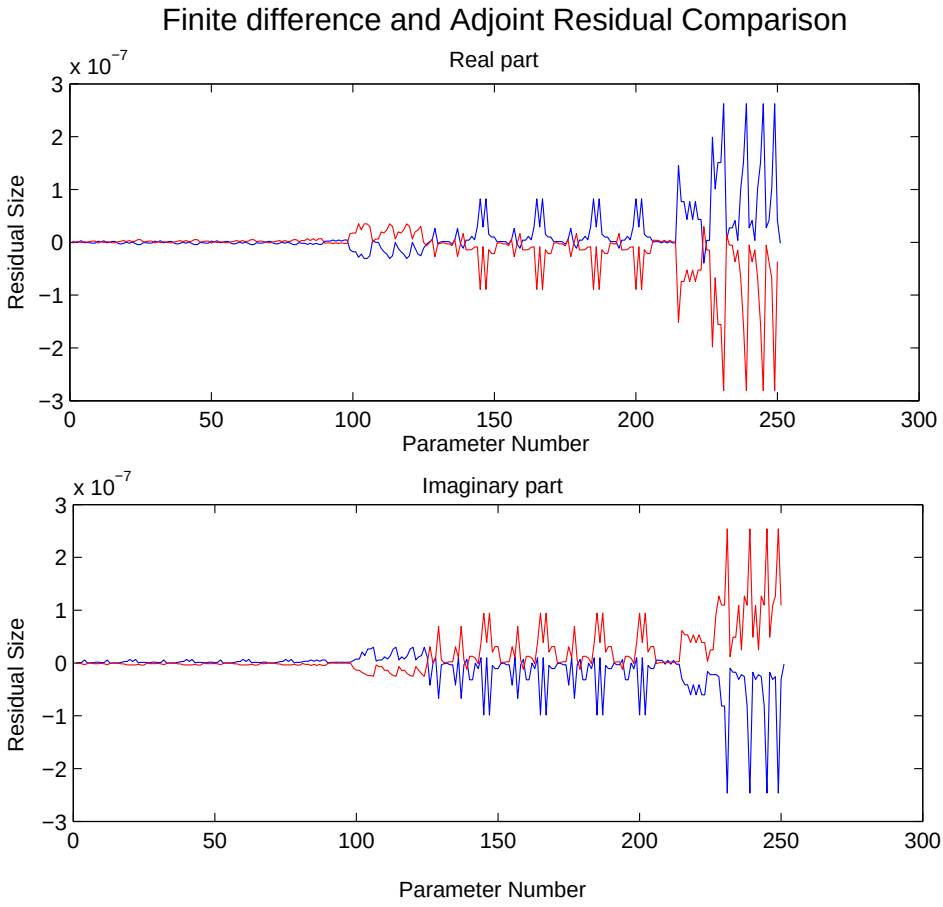

Figure 2.4 Adjoint (blue) and finite difference(red) gradient comparison. The finite difference values are plotted upside down to allow a visual comparison with the adjoint to be made.

A $\mathbf{p}$ calculated in this way represents an adjustment to $\boldsymbol{\theta}$, which will reach the exact minimum of the quadratic approximation of the error domain (Eq. 2.65). Because this is only the minimum of an approximation, it is unlikely that this step will correspond to the true minimum of Φ, and may even result in an increase in Φ. For this reason a linesearch is usually used, meaning the GN step represents a 'search direction' as in CG and Steepest Descent methods, and the method is applied iteratively until the true minimum of Φ is reached. As the the minimum of Φ is approached, $\boldsymbol{\theta} \rightarrow \boldsymbol{\theta}^*$, so the size of $\mathbf{p}$ decreases, resulting in the quadratic approximation of the error domain becoming a better match to the true error domain over the range of $\mathbf{p}$, leading to rapid convergence for later iterations. The calculation of an approximate Hessian matrix, $\mathbf{H}$, and the gradient, $\mathbf{g}$, can be derived by differentiating the error equation,

$$\Phi = \frac{1}{2}(\mathbf{u}_c(\boldsymbol{\theta}) - \mathbf{u}_m)^H(\mathbf{u}_c(\boldsymbol{\theta}) - \mathbf{u}_m), \tag{2.51}$$

where Φ is the displacement error, $\mathbf{u}_c(\boldsymbol{\theta})$ are the displacements calculated using the current material property estimate, $\boldsymbol{\theta}$, and $\mathbf{u}_m$ are the measured displacements. The gradient, $\mathbf{g} = \frac{\partial \Phi}{\partial \theta}$ is found by differentiating Eq. 2.51 once using the chain rule, giving

$$\mathbf{g} = \frac{\partial \mathbf{u}_c}{\partial \boldsymbol{\theta}}^H (\mathbf{u}_c(\boldsymbol{\theta}) - \mathbf{u}_m). \tag{2.52}$$

Here, the Jacobian matrix is $\mathbf{J} = \frac{\partial \mathbf{u}_c}{\partial \boldsymbol{\theta}}$, which is an $NO \times NP$ matrix, where the terms are given by $\mathbf{J}_{ij} = \frac{\partial (u_c)_i}{\partial \theta_j}$.

The Hessian matrix, $\mathbf{H_e}$, is an $NP \times NP$ matrix, calculated by differentiating Eq. 4.1 twice, giving

$$\mathbf{H_e} = \frac{\partial \mathbf{u}_c}{\partial \boldsymbol{\theta}}^H \frac{\partial \mathbf{u}_c}{\partial \boldsymbol{\theta}} + \frac{\partial^2 \mathbf{u}_c}{\partial \boldsymbol{\theta}^2}^H (\mathbf{u}_c(\boldsymbol{\theta}) - \mathbf{u}_m) \tag{2.53}$$

Calculation of the final term in this equation would require the use of at least third order basis functions to support the material properties, but can be neglected if it is assumed that $\mathbf{u}_c(\boldsymbol{\theta}) - \mathbf{u}_m$ is small, which is a reasonable assumption close the error minimum. Simplifying the notation above gives the final expression for the gradient as

$$\mathbf{g} = \mathbf{J}^H(\mathbf{u}_c(\boldsymbol{\theta}) - \mathbf{u}_m), \tag{2.54}$$

and the equation for the approximate Hessian matrix as

$$\mathbf{H} = \mathbf{J}^H\mathbf{J}. \tag{2.55}$$

The Jacobian matrix, $\mathbf{J} = \frac{\partial \mathbf{u}_c}{\partial \boldsymbol{\theta}}$, can be calculated by differentiating the finite element equation,

$$\mathbf{A}(\boldsymbol{\theta})\mathbf{u}(\boldsymbol{\theta}) = \mathbf{f}, \tag{2.56}$$

where $\boldsymbol{\theta}$ is the material property description vector, $\mathbf{A}(\boldsymbol{\theta})$ is the FE stiffness matrix, $\mathbf{u}$ is the displacement vector and $\mathbf{f}$ is the RHS vector, which is independent of $\boldsymbol{\theta}$. Differentiating Eq. 2.56 once with respect to a particular material property, θ_i, using the product rule, gives

$$\frac{\partial \mathbf{A}}{\partial \theta_i}\mathbf{u}_c + \mathbf{A}\frac{\partial \mathbf{u}_c}{\partial \theta_i} = \mathbf{0}. \tag{2.57}$$

Solving this equation for the Jacobian column, $\mathbf{J}_i = \frac{\partial \mathbf{u}_c}{\partial \theta_i}$, leads to

$$\mathbf{J}_i = \mathbf{A}^{-1}[\frac{\partial \mathbf{A}}{\partial \theta_i}\mathbf{u}_c]. \tag{2.58}$$

This equation shows the column of the Jacobian corresponding to the parameter θ_i can be calculated by solving the forward FE problem using a RHS vector of $\frac{\partial \mathbf{A}}{\partial \theta_i}\mathbf{u}$. This means that calculating a $NO \times NP$ Jacobian will require NP forward solves of a NO-dimensional problem. This would be an extremely computationally intensive process, however it can be sped up significantly by only performing the matrix factorization required during the forward solution once, and repeating the back-substitution step for all NP RHS vectors.

Setting the derivative to zero during the derivation of Eq. 2.50 means a stationary point of the error domain will be found, which could either be a minima or a maxima. Finding an error maxima is obviously not desirable, so steps need to be taken to ensure that the error is reduced at each iteration. A given search direction, $\mathbf{p}$, can be guaranteed to be a descent direction if the directional derivative, $\mathfrak{Re}\{\mathbf{p}^H\mathbf{g}\}$, along that direction is negative. Premultiplying Eq. 2.50 by $\mathbf{p}^H$ and taking the real parts leads to

$$\mathfrak{Re}\{\mathbf{p}^H\mathbf{g}\} = -\mathfrak{Re}\{\mathbf{p}^H\mathbf{H}\mathbf{p}\}. \tag{2.59}$$

A descent direction is therefore guaranteed with the GN method if $\mathfrak{Re}\{\mathbf{p}^H\mathbf{H}\mathbf{p}\} > 0$ for all $\mathbf{p}$, which means $\mathbf{H}$ must be positive definite. A simple way of ensuring positive definiteness is to add a factor to the diagonal of the Hessian. This is a form of problem regularization, where the regularized Hessian, $\mathbf{H}_r$ is given by

$$\mathbf{H}_r = \mathbf{H} + \gamma_r\mathbf{I}. \tag{2.60}$$

As the regularization factor, γ_r increases, Eq. 2.50 suggests the GN step will begin to look more like the steepest descent direction, so this form of regularized GN method can be thought of as a compromise between the reliability of steepest descent and the rapid convergence of the GN method.

Many methods of selecting a value for γ_r exist, the methods used in the reconstruction codes are a combination of Joachomowitz and Marquadt regularization. Joachomowitz regularization [32] involves using a γ_r value proportional to the current error value. This ensures a higher level of regularization and reliability in earlier iterations,

where divergence of the iterates is a greater risk, and lower levels later at later iterations when the algorithm is approaching an error minima, and divergence of the iterates is less likely so the fast convergence of the GN method can be exploited. Marquadt Regularization [33] involves scaling the system of equations in Eq. 2.50 so that the diagonal of $\mathbf{H}$ is all ones. This gives a sense of what is a 'big' γ_r, and what is a 'small' γ_r. A set of rules is then used for selecting γ_r at each iteration.

1. Set $\gamma_r = \gamma_r^0$ at the first iteration, where γ_r^0 is some reasonably large value.
2. If the step size, α_k for the previous iteration was close to one, reduce γ_r as the Hessian is likely to be well-conditioned and positive definite. Do not allow γ_r to become smaller than some minimum value.
3. If no error reduction was achieved, reset γ_r to γ_r^0, or increase γ_r, as the Hessian is likely to have become highly ill-conditioned or no longer positive definite.
4. If α_k is smaller than about 0.1, increase γ_r as the Hessian is likely to be poorly conditioned and leading to unreasonably large search directions

The actual values to use for parameters such as γ_r^0, the amount to reduce or increase γ_r by, and the minimum allowable γ_r are selected by balancing efficient algorithm performance with reliability. Basic Pseudocode for the GN method is given in algorithm 2.2.

2.3.3 Line Searches

The reliability and performance of the CG and GN methods are improved by adding a line search, which is a one-dimensional minimization along the direction given by the either the CG or GN method (known as the 'search direction'). Different types of optimization algorithms perform better with different types of linesearch, for example Newton type algorithms perform well with an inexact linesearch [34], whereas Conjugate Gradient methods require reasonably exact methods [35]. A line search finds an acceptable step size, α_i, so that an error-reducing update is given by:

$$\boldsymbol{\theta_{i+1}} = \boldsymbol{\theta_i} + \alpha_i \mathbf{p}_i. \tag{2.61}$$

Because Eq. 2.61 is simply an addition operation, a complex search direction could be easily split up into real and imaginary parts, so the techniques are the same as those for real variables. It should be noted however, the directional derivative along $\mathbf{p}$, which is given by $\mathbf{p}^T\mathbf{g}$ in the real case is given by $\mathfrak{Re}\{\mathbf{p}^H\mathbf{g}\}$ in the complex case. This can be verified by a simple comparison of the split-up and complex inner products as in Eq. C.4. Two linesearch techniques are used in the reconstruction code, a secant method with an Armijo backup. Details of these techniques are given below.

Algorithm 2.2: Pseudocode for the calculating the search direction using the Gauss-Newton method with Marquadt and Joachimowicz regularization.

Input: Calculated Displacements, $\mathbf{u}_c$, Measured Displacements, $\mathbf{u}_m$, FE stiffness matrix, $\mathbf{A}$, Iteration number, k,Current and Previous Errors, Φ_k and Φ_{k-1},last step size, α_{k-1}

Output: Gauss-Newton search direction, $\mathbf{p}_k$, Gradient, $\mathbf{g}_k$

$\beta_\gamma = 0.2$; $\gamma_0 = 0.1$;

cc *Calculate Jacobian matrix*;

for *j=1* **to** *NP* **do**

  $\mathbf{r}_j = \frac{\partial \mathbf{A}}{\partial \theta_j}\mathbf{u}_c$;

  $\mathbf{J}(:, j) = \mathbf{A}^{-1}\mathbf{r}_j$

end

cc *Use Jacobian to calculate gradient and Hessian*;

$\mathbf{g}_k = \mathbf{J}^H(\mathbf{u}_c - \mathbf{u}_m)$;

$\mathbf{H}_k = \mathbf{J}^H\mathbf{J}$;

cc *Apply Joachimowicz regularization*;

for *i=1* **to** *NP* **do**

  $\mathbf{H}(i, i) = \mathbf{H}(i, i) + \alpha_J \Phi_k$

end

cc *Apply Marquadt regularization*;

$\mathbf{r}_m = -\mathbf{g}_k$;

Scale $\mathbf{H}\mathbf{p}_k = \mathbf{r}_m$ system so that $\mathbf{H}$ has ones in the diagonal;

if $k = 1$ **then**

  $\gamma_r = \gamma_0$

else if $\frac{\Phi_k}{\Phi_{k-1}} \geq 1$ *or* $\alpha_{k-1} < 0.1$ **then**

  $\gamma_r = \gamma_r / \beta_\gamma$

else

  $\gamma_r = \beta_\gamma \gamma_r$

end

for *i=1* **to** *NP* **do**

  $\mathbf{H}(i, i) = \mathbf{H}(i, i) + \gamma_r$

end

cc *Solve for GN search direction*;

$\mathbf{p}_k = \mathbf{H}^{-1}\mathbf{r}_m$;

Scale $\mathbf{p}_k$ back to original size;

2.3.3.1 Armijo Line Search

The Armijo line search [36] is an extremely reliable inexact line search technique; some error reduction will be achieved for all but the most complex error domain, as long as the search direction is a descent direction ($\mathfrak{Re}\{\mathbf{p}^H\mathbf{g}\} < 0$). The method can be quite computationally intensive because of the large number of forward solves required to obtain an approximate solution when the acceptable α_i values are not close to 1. It is included in the reconstruction code for its extremely high reliability, and helps to prevent the reconstructions from getting 'stuck', as some update to the material properties is almost guaranteed with each iteration.

The Armijo line search requires two conditions to be met. The first Armijo condition (AC1) enforces a descent condition, and is given by:

$$\Phi_{i+1} < \Phi_i + a_1\mathfrak{Re}\{\mathbf{p}^H\mathbf{g}\}\alpha_i. \tag{2.62}$$

The second Armijo condition ensures that overly small step sizes are avoided, and is important for Quasi-Newton reconstruction techniques to ensure positive-definiteness of the Hessian update.

$$\Phi_{i+1} > \Phi_i + a_2\mathfrak{Re}\{\mathbf{p}^H\mathbf{g}\}\alpha_i. \tag{2.63}$$

$0 < a_1 < 0.5$ must be satisfied to ensure descent and that the minimum value of a quadratic error function is included in the acceptable α range, and $a_1 < a_2 < 1$ is required to ensure an acceptable range exists, and that a zero step size is not acceptable. Commonly used values are $a_1 = 0.05$ and $a_2 = 0.9$. Figure 2.5 gives a graphical explanation of the principles of the Armijo line search.

A forward and back tracking search method is used to find an acceptable value for α_i. $\alpha = 1$ is tried first, as this is the ideal step size for the GN method. The CG step is also scaled so that the best step size is close to 1 most of the time. If the AC1 condition is satisfied at $\alpha = 1$, α is increased until AC1 fails (forward tracking), and the last alpha value which passed AC1 is selected. If AC1 fails for $\alpha = 1$, α is decreased until an α is reached where AC1 is satisfied (back tracking). Once an α which satisfies AC1 has been found by either forward or back tracking search, AC2 is checked. If it is satisfied, the line search is complete. If it fails, the current alpha becomes a lower bound and the lowest α which failed AC1 becomes an upper bound, and a bisection technique is used to find an alpha value which satisfies both AC1 and AC2. Basic pseudocode for the Armijo implementation in the reconstruction algorithm is given in Algorithm 2.3.

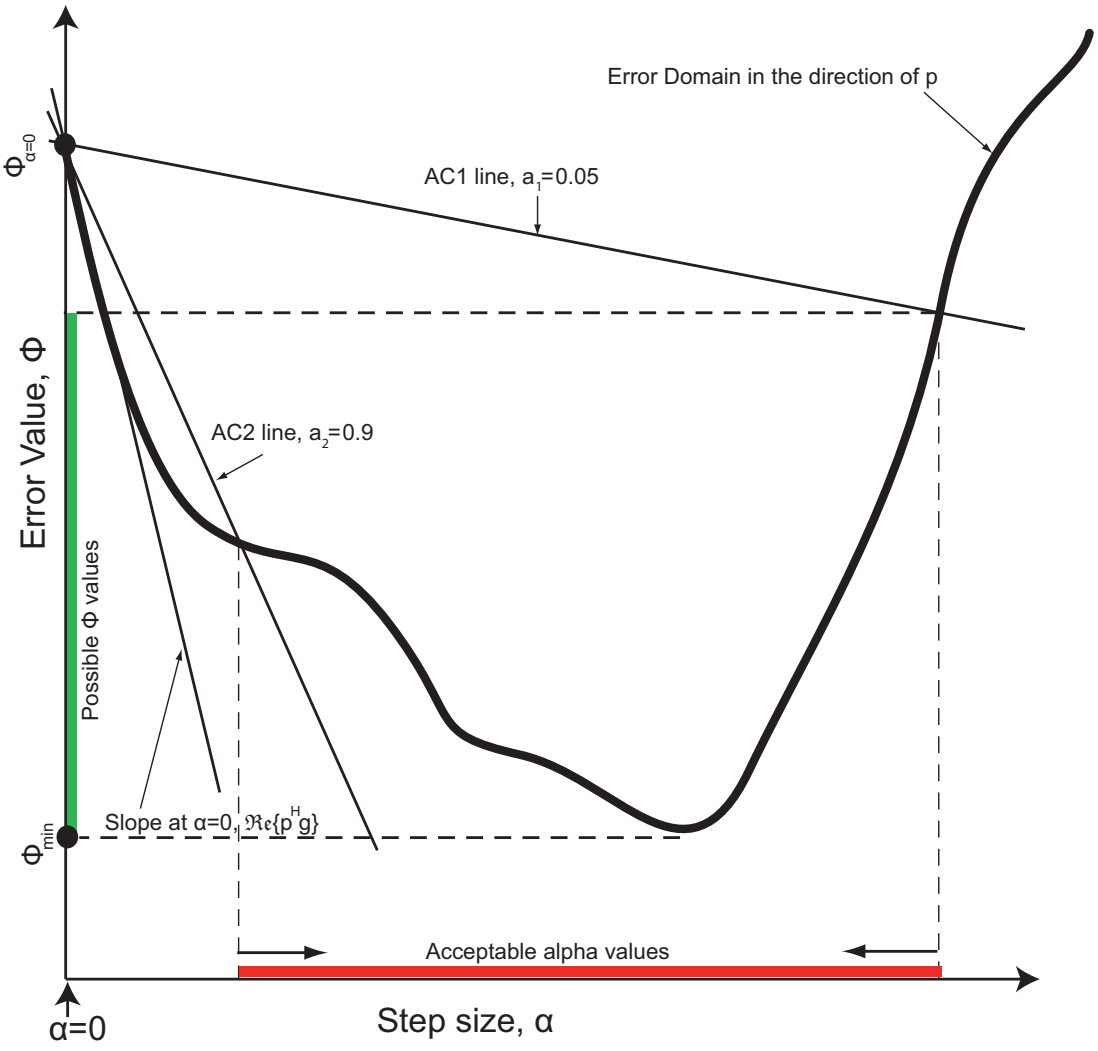

Figure 2.5 Graphical depiction of the Armijo conditions, AC1 and AC2. Both conditions are shown as a function of α, as well as a possible one dimensional error domain along $\mathbf{p}$. The range of feasible alpha values is marked in red, with the corresponding range of possible Φ values shown in green. The directional derivative ($\mathfrak{Re}\{\mathbf{p}^H\mathbf{g}\}$, or slope at $\alpha = 0$) is shown in blue.

Algorithm 2.3: Pseudocode for step size selection using the Armijo linesearch.

Input: AC1 and AC2 requirements, **p** and **g**
Output: Step size, α_i
$j = 0$;
$\alpha_j = 1$;
cc *Check AC1 condition*;
if *AC1=true* **then**
  cc *Use forward tracking*;
  while *AC1=true* **do**
    $j = j + 1$;
    α_j=$\alpha_{j-1} \times 4$;
    $\boldsymbol{\theta}_j = \boldsymbol{\theta}_{j-1} + \alpha_j \mathbf{p}$; Solve forward problem;
    check AC1;
  end
  upperbound=α_j;
  $\alpha_i = \alpha_{j-1}$;
else
  cc *Use back tracking*;
  while *AC1=false* **do**
    $j = j + 1$;
    α_j=$\alpha_{j-1} \times 0.5$;
    $\boldsymbol{\theta}_j = \boldsymbol{\theta}_{j-1} + \alpha_j \mathbf{p}$; Solve forward problem;
    check AC1;
  end
  $\alpha_i = \alpha_{j-1}$;
  upperbound=α_{j-1};
end
cc *Check AC2 condition at* $\alpha = \alpha_i$;
if *AC2=true* **then**
  α_i satisfies AC1 and AC2
else
  lowerbound=α_i;
  Use bisection with upperbound and lowerbound to find α_i which satisfies both AC1 and AC2;
end

2.3.3.2 Secant Line Search

The secant method is a faster exact line search technique which iteratively solves for a stationary point of the error domain, i.e.

$$\frac{\partial}{\partial\alpha}\Phi(\boldsymbol{\theta}+\alpha\mathbf{p})=0. \tag{2.64}$$

This technique can be unreliable, as it will find an error maximum if the the apparent second directional derivative is negative, or will choose an unreasonably large alpha value if it is very small. For this reason, the Armijo line search is used as a backup if the secant method fails. The secant method derivation [26] uses the second order Taylor series approximation,

$$\Phi(\boldsymbol{\theta}+\alpha\mathbf{p})\approx\Phi(\boldsymbol{\theta})+\alpha[\frac{\partial}{\partial\alpha}(\Phi(\boldsymbol{\theta}))]+\frac{\alpha^2}{2}[\frac{\partial^2}{\partial\alpha^2}(\Phi(\boldsymbol{\theta}))]. \tag{2.65}$$

The term $\frac{\partial}{\partial\alpha}(\Phi(\boldsymbol{\theta}))$ is just the directional derivative along p, given by $\mathfrak{Re}\{\mathbf{p}^H\mathbf{g}\}$. A finite difference approximation of the second derivative can be used,

$$\frac{\partial^2}{\partial\alpha^2}(\Phi(\boldsymbol{\theta}))\approx\frac{\mathfrak{Re}\{\mathbf{p}^H\mathbf{g}(\boldsymbol{\theta}+\delta_s\mathbf{p})\}-\mathfrak{Re}\{\mathbf{p}^H\mathbf{g}(\boldsymbol{\theta})\}}{\delta_s} \tag{2.66}$$

Combining Eqs. 2.65 and 2.66, then differentiating with respect to α gives:

$$\frac{\partial}{\partial\alpha}\Phi(\boldsymbol{\theta}+\alpha\mathbf{p})\approx\mathfrak{Re}\{\mathbf{p}^H\mathbf{g}(\boldsymbol{\theta})\}+\alpha\frac{\mathfrak{Re}\{\mathbf{p}^H\mathbf{g}(\boldsymbol{\theta}+\delta_s\mathbf{p})\}-\mathfrak{Re}\{\mathbf{p}^H\mathbf{g}(\boldsymbol{\theta})\}}{\delta_s}, \tag{2.67}$$

for some sufficiently small δ_s. Setting this to zero and solving for alpha gives the minimum of the Taylor series approximation,

$$\alpha=-\delta_s\frac{\mathfrak{Re}\{\mathbf{p}^H\mathbf{g}(\boldsymbol{\theta})\}}{\mathfrak{Re}\{\mathbf{p}^H\mathbf{g}(\boldsymbol{\theta}+\delta_s\mathbf{p})\}-\mathfrak{Re}\{\mathbf{p}^H\mathbf{g}(\boldsymbol{\theta})\}}. \tag{2.68}$$

Because the Taylor series in Eq 2.65 is only an approximation, this value of α will most likely not be the true minimum. The secant method can be applied iteratively, so that a modification to α, δ_α, is calculated each iteration until a true minima is found. When δ_α becomes small, the method is deemed to have converged.

The multiple gradient evaluations required can make the secant method quite computationally intensive, although the rapid convergence behavior for 'well behaved' error domains often outweighs this disadvantage. A gradient evaluation can be saved by using the gradient from the previous α value to calculate the finite difference second derivative if the previous δ_α was sufficiently small. Although the secant method is intended to be an exact linesearch, in practice it is often used as more of an inexact linesearch technique by using allowing only small numbers of secant iterations. Pseudocode for the secant linesearch is given in Algorithm 2.4.

Algorithm 2.4: Pseudocode for step size selection using the secant linesearch.

Input: Current material property estimate, $\boldsymbol{\theta_0}$, Current gradient, $\mathbf{g}(\boldsymbol{\theta_0})$, Search Direction, $\mathbf{p}$
Output: Step size, α
cc *Initialization*;
$\delta_{\alpha\,min} = 0.05,\ \delta_{\alpha\,max} = 10,\ ii_{max} = 7;$
$\alpha = 0,\ \delta_s = 0.0001,\ \delta\alpha = 1000,\ \theta = \theta_0,\ ii = 0;$
cc *Begin Secant Iterations*;
while $(\delta_\alpha > \delta_{\alpha\,min})$ *and* $(ii < ii_{max})$ **do**
  $ii = ii + 1;$
  $\delta_\alpha = -\delta_s \frac{\mathbf{p}^T\mathbf{g}(\boldsymbol{\theta})}{\mathbf{p}^T\mathbf{g}(\boldsymbol{\theta}+\delta_s\mathbf{p})-\mathbf{p}^T\mathbf{g}(\boldsymbol{\theta})};$
  $\boldsymbol{\theta} = \boldsymbol{\theta} + \delta\alpha\mathbf{p};$
  $\alpha = \alpha + \delta_\alpha;$
  if $(\alpha < 0)$ *or* $(\delta_\alpha > \delta_{\alpha\,max})$ **then**
    SECANT FAILURE;
    BREAK;
  end
  if $\delta\alpha < 0.1$ **then**
    $\delta_s = -\delta_\alpha$
  else
    $\delta_s = 0.0001$
  end
end

2.3.4 Regularization Techniques

The error function, Φ, places no restrictions on the material property values or their distribution. This means any distribution which decreases Φ will be acceptable as a solution, whether or not it is physically realistic. Some *a-priori* information about the true material property solution can be deduced by considering the structure of human tissue. Techniques which involve modifying Φ in an attempt to make the reconstruction algorithm prefer solutions which fit this *a-priori* information are known as regularization techniques. Three regularization methods are included in the reconstruction code, Tikhonov, Total variation minimization and spatial filtering. To increase the flexibility of the inversion algorithm, the relative level of each type of regularization is allowed to vary linearly as the iterations progress.

2.3.4.1 Tikhonov Regularization

A 'ballpark' figure for the material property values is provided by the initial guess at the material property distribution. Tikhonov regularization is a method of ensuring the material property solution does not vary wildly from this initial guess. The function

for Φ is modified to Φ_{tk},

$$\Phi_{tk} = \frac{1}{2}(\mathbf{u}_c - \mathbf{u}_m)^H(\mathbf{u}_c - \mathbf{u}_m) + \alpha_{tk}(\boldsymbol{\theta} - \boldsymbol{\theta}_0)^H(\boldsymbol{\theta} - \boldsymbol{\theta}_0), \tag{2.69}$$

where $\boldsymbol{\theta}$ is the current material property estimate, $\boldsymbol{\theta}_0$ is the initial material property guess, and α_{tk} is the weighting applied to Tikhonov regularization. This Regularization technique effectively penalizes solutions according to how far they deviate from the initial guess, therefore will preferentially select solutions which are closer to the initial guess. A modification to this method is where $\boldsymbol{\theta}_0$ is set to the previous material property estimate at each iteration, limiting the change in material properties for each iteration, but not the total deviation from the initial guess.

2.3.4.2 Total variation minimization

Human tissue contains areas of particular tissue types, with each area having approximately constant material properties. Total variation minimization (TV) provides a means to preferentially select material property distributions which consist of discrete regions of constant material properties over distributions with a greater degree of spatial variation. The function for Φ is modified to Φ_{tv},

$$\Phi_{tv} = \frac{1}{2}(\mathbf{u}_c - \mathbf{u}_m)^H(\mathbf{u}_c - \mathbf{u}_m) + \iiint_{\Omega} \left(\alpha_{tv}\sqrt{\nabla\boldsymbol{\theta}^H\dot{\nabla}\boldsymbol{\theta}}\right)dV, \tag{2.70}$$

where $\nabla\boldsymbol{\theta}$ is the spatial variation of the material property, $\boldsymbol{\theta}$, and α_{tv} is the weighting applied to TV. The integral means that the level of total variation is the area under the $\sqrt{\nabla\theta^H\nabla\theta}$ curve. Figure 2.6 shows one-dimensional examples of a material property distribution with low total variation, along with a similar case with high total variation. The addition of total variation minimization will therefore preferentially select material property distributions consisting of discrete regions of constant material properties over distributions with higher levels of spatial variation which will hopefully lead to cleaner, more physiologically correct images. Figure 2.7 is an illustration of the effect total variation minimization has on the material property solution.

2.3.4.3 Spatial Filtering

Spatial filtering is a smoothing technique, based on the idea that there should not be large variations in material properties in regions of a particular tissue type. It does have the effect losing some of the definition of boundaries between tissue types, so is often used with a low weighting at later iterations. The technique involves simply replacing each material property value with a weighted average of the material property value and that of it's closest neighbors, so that the spatially filtered value for a material

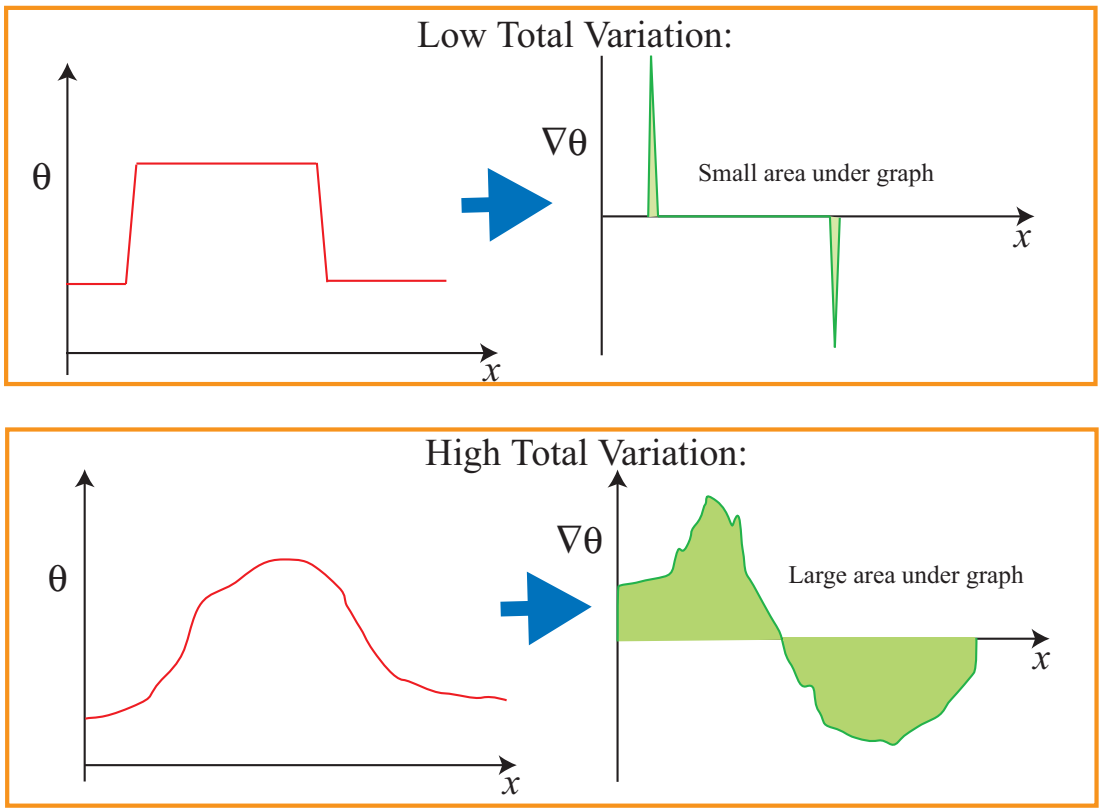

Figure 2.6 One dimensional parameter description examples to illustrate total variation. Equation 2.70 shows the total variation is given by the area under the $\nabla\boldsymbol{\theta}$ curve, therefore the upper case, with discrete regions of constant material properties has a low total variation, whereas the lower case, which shows a material property distribution with greater spatial variation has a high total variation.

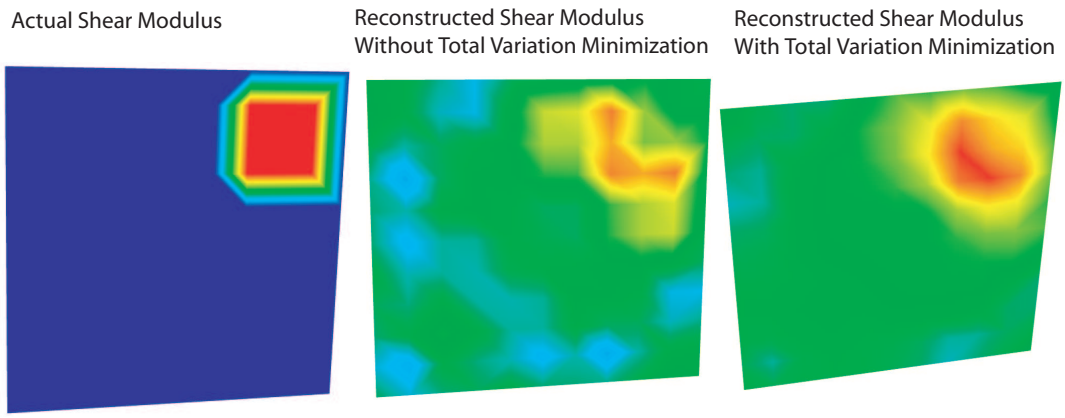

Figure 2.7 The effect of total variation minimization. The left image shows the true material property distribution used to generate the simulated input motion data for the inverse problem. The middle image shows the reconstructed property distribution with no total variation minimization, and the right image shows the same reconstruction with total variation minimization included. Total variation minimization favors material property distributions with discrete regions of approximately constant values.

property θ_k is given by

$$\theta_k = (1 - W_{sf})\theta_k + \frac{w_{sf}}{N_{con}} \sum_{l=1}^{N_{con}} (\theta_l), \tag{2.71}$$

where w_{sf} is a weighting applied to spatial filtering, l refers to the nodes in the neighborhood of node k, and N_{con} is the number of these neighborhood nodes.

2.3.5 Subzone Implementation

A subzone-based reconstruction scheme is used to allow material property reconstructions using the very large datasets MRI is capable of producing. MR-detected motion data is available at spatial resolutions which often produce over 100,000 nodal points for a single scan. Current computer systems are unable to process FE models of this size due to memory limitations. The time that required to build and solve this large system of equations is also prohibitive. To get around these issues, the overall size of the problem can be reduced by using a smaller sub-region of the full dataset, or a lower spatial resolution.

The full-volume data provided by MRI allows a subset of data of any size to be 'carved' out of the full dataset, and used to run a reconstruction where the Dirichlet boundary conditions are the motions on the boundary of this subset. This idea can be expanded to a macro-parallelization strategy for reconstructing whole MR-detected motion datasets at MR pixel-resolution, where many different reconstructions are per-

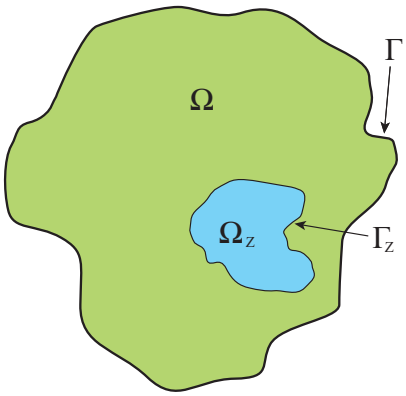

Figure 2.8 Schematic representation of subzone concept. The global problem domain is represented by Ωz with boundary Γ, and the domain of the subzone is represented by Ω_zz with boundary Γ_z.

formed on separate processors, using many different subsets of the motion data. Results from the individual subsets can then be combined to encompass the whole geometry, an approach is known as an 'overlapping subzone method' [37]. This method has proven successful in reconstructing stiffness distributions using MR-detected motion datasets from both gelatine phantoms and real patients [38, 9]. A brief overview of the method and its advantages over global reconstruction methods is presented below, for a more detailed treatment see [37, 39].

Figure 2.8 illustrates the subzone concept. A small sub-domain, or subzone, Ω_z is extracted from the global problem domain, Ω. Displacement data is available over all of Ω_z, including the boundary, Γ_z, which means there is enough information to reconstruct a material property description of Ω_z using the elastographic reconstruction techniques detailed in Section 2.3. If reconstructions are performed on a set of subzones for which the union of all the individual Ω_z's encompasses the total problem domain, Ω, these results can be combined to form a material property description for the total problem domain at MR pixel resolution, something that is not possible using global reconstruction techniques. The technique effectively replaces the minimization of a large sum with a sum of smaller minimizations, i.e.

$$\min\Big(\sum_{\Omega}(u_c-u_m)\overline{(u_c-u_m)}_{\Omega}\Big)=\sum_{z=1}^{N_z}\min\Big(\sum_{\Omega_z}(u_c-u_m)\overline{(u_c-u_m)}_{\Omega_z}\Big), \qquad (2.72)$$

where $\mathbf{u}_c$ and $\mathbf{u}_m$ are individual calculated and measured displacements, Ω represents the entire problem domain, and Ω_z represents the z'th subzone of a total of N_z.

There are many advantages to this approach. The most obvious is the reduction

in the size of the inversion problems which must be solved. The computational cost of the optimization based techniques used in the inversion process scales cubically with the number of nodal points, so the computational load quickly becomes unmanageable as problem size increases. The subzone method allows the size of the minimization problems to be chosen by the user to suit the available computational resources, without limiting the size or spatial resolution of the overall problem. This strategy also allows a relatively simple macro-parallelization strategy, where multiple subzones are processed at once on separate processors. Each subzone inversion is independent of the others, so inter-process communication is minimal, allowing efficient use of available resources. Another less obvious advantage is the increase in reliability of the reconstructions. The nature of minimization methods mean they are to some degree unreliable, for example they may end up at a local error minima rather that the minima corresponding to the true parameter description, or they may fail to make any progress at all in reducing the error. Good algorithm design reduces the occurrence of these failures, but they may still occur under certain conditions. Because the subzone method involves so many different minimizations, the occasional failure on one of the subzones does not mean the entire reconstruction will fail. The solution from the failed subzone can simply be ignored, and a different subzone or set of subzones can be defined which encompass the region of the failed subzone. Provided these are successful, the reconstructed material property description will still cover the whole of Ω.

The subzone method is implemented using the Message Passing Interface (MPI). One of the processors is defined as the 'master' processor, which handles such 'administrative' tasks as dividing the problem into subzones, sending them out to the other slave processors for reconstruction, and receiving the completed material property solutions from the slaves, and combining these into an image of the entire problem domain. Once a subzone is sent to a slave processor, the reconstruction proceeds in the standard fashion outlined in section 2.3, therefore only the tasks performed by the master processor will be outlined here.

Pseudocode for the method of dividing the problem domain into a grid of overlapping subzones is given in algorithm 2.5. This method creates a subzone distribution which encompasses all of Ω, and ensures each subzone meets a minimum size criteria. The center point for the grid of subzones is determined randomly, therefore a different set of subzones will be generated each time the geometry is divided up, reducing the occurrence of boundary related artefacts in the final material property image.

When the master process receives the solution for a particular zone, it inserts the solution into the correct location in the global solution arrays. Because the subzones overlap, multiple values for some material properties will be returned. These are dealt with by using an average value.

Algorithm 2.5: Pseudocode for division of global geometry into a grid of overlapping subzones.

Input: Global nodal positions, $\mathbf{x}_g$, $\mathbf{y}_g$, $\mathbf{z}_g$, Global list of element centroid locations, $\mathbf{Elc}_g$, Number of Subzones in each direction, Nz_x, Nz_y, Nz_z, Subzone overlap factor, $SZov$, Minimum number of internal nodes, min_{nod}

Output: Number of Subzones, Nsz, Subzone mesh information, **SM**

cc *Create Zone grid covering whole geometry*;

$g_x = (\max(\mathbf{x}_g) - \min(\mathbf{x}_g))/Nz_x$;

$g_y = (\max(\mathbf{y}_g) - \min(\mathbf{y}_g))/Nz_y$;

$g_z = (\max(\mathbf{z}_g) - \min(\mathbf{z}_g))/Nz_z$;

Create $g_x \times g_y \times g_z$ grid and center on random location in $\mathbf{Elc}_g$;

Each grid cube containing at least 1 point in $\mathbf{Elc_g}$ becomes a subzone;

Nsz = Number of subzones;

cc *Apply subzone overlap and ensure each subzone is large enough*;

for $iz = 1$ **to** Nsz **do**

  $Nn_{int} = 0;, \quad tSZov = SZov$;

  while $Nn_{int} < min_{nod}$ **do**

    $\mathbf{SM}(:, iz)$ = all elements with centroid within grid cube + overlap given by $tSZov$;

    Nn_{int} = Number of internal nodes in $\mathbf{SM}(:, iz)$;

    if $Nn_{int} < min_{nod}$ **then**

      cc Increase subzone overlap to include more internal nodes.;

      $tSZov = tSZov \times 1.5$

    end

  end

end

2.3.6 Material Property Bounds

Optimization-based reconstruction techniques can run into problems where some of the material property solution takes on unrealistic values, which increases the chance of the algorithm finding a local minima, rather than the true minima corresponding the correct material properties.

To alleviate this problem, maximum and minimum bounds are applied to each of the material properties to ensure they remain physically realistic. The safest time to apply these bounds is after each subzone has been processed, as this will have no effect on the algorithm processing each zone. It has the disadvantage of modifying the material property distribution returned from the subzone, therefore the update to the global property description is no longer one that is guaranteed to result in a reduction in the error, however this method does perform well in practice.

An alternative method is to apply the bounds each time the material properties are updated. This method does not alter the material property description returned from each subzone, so any reduction in error is preserved, but can sometimes cause the minimization algorithm to fail completely for some subzones. This problem could be addressed by using a constrained minimization approach, where a penalty term is added to the error function for any material properties which have physically unrealistic values, however further work would be required to implement this. The problem can be partially alleviated by setting the search direction terms which would have the solution move into the infeasible region to zero. This does not guarantee the modified search direction will be a descent direction, but does ensure the initial directional derivative is correct, which ensures that the linesearch techniques will function normally.

A comparison of convergence behavior for the two techniques is shown in Fig. 2.9, and a reconstruction of a gelatine phantom with two stiff cones using each bounding technique is given in Fig. 2.10. Applying the bounds every time the material properties are updated appears to give slightly better convergence behavior and a cleaner material property image. Because of the possible complications that modifying the search direction could have on the optimization algorithm, the choice of when to apply the material property bounds is left as a user-selected option.

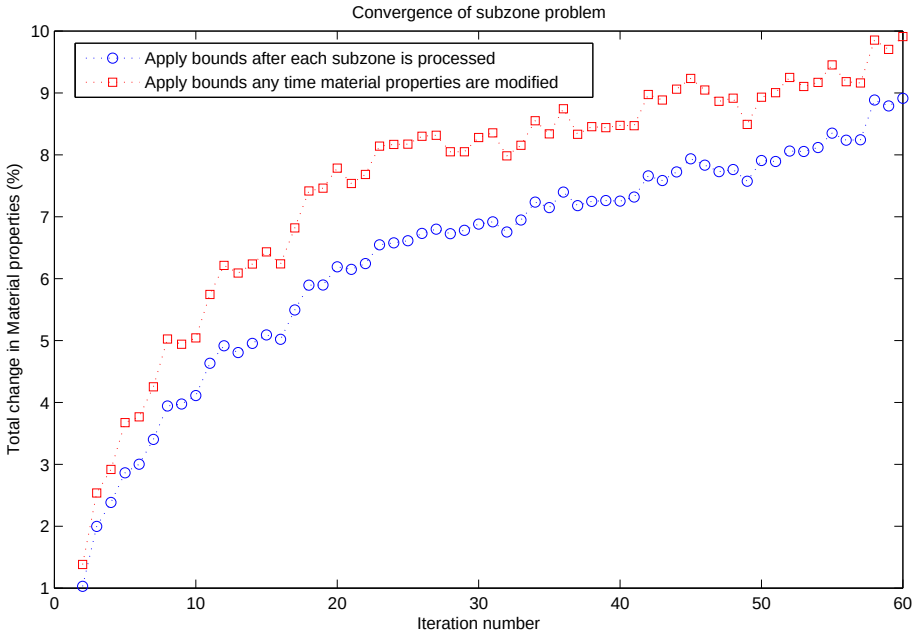

Figure 2.9 Convergence of subzone reconstruction algorithm with material property bounds applied at the subzone level (blue circles), and applied at the material property update level (red squares). Updates applied at the material property update level accelerates converge.

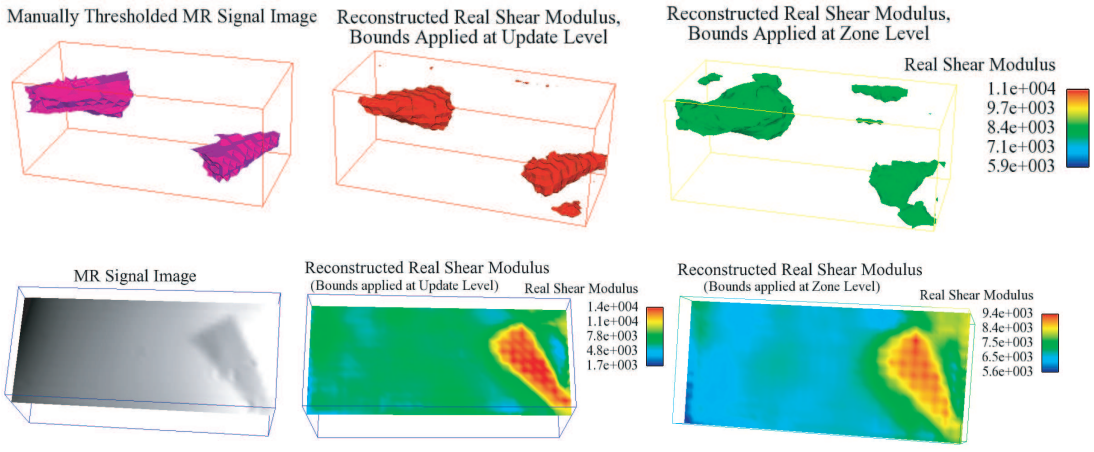

Figure 2.10 Material property image with bounds applied at the subzone level (right image), and applied at the material property update level (middle image). The left image shows the manually thresholded MR signal image, which shows the true structure of the phantom. Updates applied at the material property level lead to a cleaner image.

Chapter 3

MRI Data Capture, Conversion and Display of Results

3.1 MRI Motion Scanning

Measurements of motion data are made using a Magnetic Resonance Imaging (MRI) scanner. The sample being imaged is actuated using a piezoelectric actuator with a sinusoidal driving signal. The resulting harmonic motions can then be detected throughout the full volume of the material using a phase contrast MRI technique [40]. A conventional MRI system is used with additional motion sensitizing magnetic field gradients, which enables measurement of the motion by measuring the accumulated phase shift of the nuclear spins [41] at different points along the sinusoidal signal. Motion encoding can be along any of the three orthogonal axes, thus leading to a full 3D description of the motion at every point in space within the imaged volume. This technique produces a complex displacement value at a grid of internal points within the sample, along with a value for the strength of the MR signal at each point. This signal strength measurement can be altered by adding a contrast agent to the material, so can be used to differentiate different material types in a tissue-mimicking gelatine or silicon phantom. Typical conditions used are a spatial resolution of 1 × 1 × 1mm and at a frequency of 100Hz, which gives a reasonable number of shear waves across the sample being imaged. Typical sample dimensions are about 100 × 100 × 30mm. The shear wavelength can be estimated using

$$\lambda_s \approx \frac{1}{f}\sqrt{\frac{\mathfrak{Re}\{\mu\}}{\mathfrak{Re}\{\rho\}}}, \tag{3.1}$$

where λ_s is the shear wavelength, f is the actuation frequency in Hz, μ is the shear modulus of the material and ρ is the density. Approximate values of $f = 100$Hz, $\mathfrak{Re}\{\mu\} = 9000$Pa and $\mathfrak{Re}\{\rho\} = 1000\text{kgm}^{-3}$ give $\lambda_s = 30$mm.

3.2 Data Conversion

Motion Data from MRI scans is supplied as matlab '.mat' files, which contain information relevant to the dataset, such as frequency, spatial resoultion and information to convert values from the MRI coordinates to the physical (xyz) coordinate directions, as well as the full volume amplitude and phase of the harmonic motions throughout the material. These are supplied in 3-dimensional arrays, where the index of a value indicates it 3-D position in the original geometry. It is important that this amplitude and phase information is converted to a form which is consistent with the complex displacement amplitudes used in the inversion code.

The derivation of the finite element method uses the harmonic motion assumption

$$\mathbf{u}(\mathbf{x},t) = \mathfrak{Re}\{\bar{\mathbf{u}}_c(\mathbf{x})e^{i\omega t}\}. \tag{3.2}$$

Here, $\mathbf{u}(\mathbf{x},t)$ is the real-valued displacement occurring at a point, $\mathbf{x}$, at time t, and $\bar{\mathbf{u}_c}$ is a complex displacement amplitude which defines the harmonic displacement amplitude, with frequency ω. If we define the real and imaginary components of $\bar{\mathbf{u}_c}$ as

$$\bar{\mathbf{u}}_c(\mathbf{x}) = \bar{\mathbf{u}}_r(\mathbf{x}) + i\bar{\mathbf{u}}_i(\mathbf{x}), \tag{3.3}$$

Eq. 3.2 can be expanded using Euler's formula, $e^{i\theta} = \cos\theta + i\sin\theta$, to give

$$\mathfrak{Re}\{\bar{\mathbf{u}}_c(\mathbf{x})e^{i\omega t}\} = \mathfrak{Re}\{\Big(\bar{\mathbf{u}}_r(\mathbf{x}) + i\bar{\mathbf{u}}_i(\mathbf{x})\Big)\Big(\cos(\omega t) + i\sin(\omega t)\Big)\}, \tag{3.4}$$

which leads to

$$\mathbf{u}(\mathbf{x},t) = \bar{\mathbf{u}}_r(\mathbf{x})\cos(\omega t) - \bar{\mathbf{u}}_i(\mathbf{x})\sin(\omega t). \tag{3.5}$$

This equation gives the form of the real harmonic motions, so it is important that the measured motions are interpreted so that they are in the same form.

The MR-detected motions are given as a real-valued amplitude, $\mathbf{r}(\mathbf{x})$, and phase, $P(\mathbf{x})$, for each point, so that the displacement at a point, $\mathbf{x}$, and at time t, are given by

$$\mathbf{u}(\mathbf{x},t) = \mathbf{r}(\mathbf{x})\cos(\omega t + P(\mathbf{x})) \tag{3.6}$$

Euler's formula allows this to be written as

$$\mathbf{u}(\mathbf{x},t) = \mathfrak{Re}\{\mathbf{r}(\mathbf{x})e^{i(\omega t + P(\mathbf{x}))}\} \tag{3.7}$$

$$\mathbf{u}(\mathbf{x},t) = \mathfrak{Re}\{\mathbf{r}(\mathbf{x})e^{iP(\mathbf{x})}e^{i(\omega t)}\} \tag{3.8}$$

$$\mathbf{u}(\mathbf{x},t) = \mathfrak{Re}\{\mathbf{r}(\mathbf{x})\Big(\cos(P(\mathbf{x})) + i\sin(P(\mathbf{x}))\Big)\Big(\cos(\omega t) + i\sin(\omega t)\Big)\} \tag{3.9}$$

$$\mathbf{u}(\mathbf{x},t) = \mathbf{r}(\mathbf{x})\cos(P(\mathbf{x}))\cos(\omega t) - \mathbf{r}(\mathbf{x})\sin(P(\mathbf{x}))\sin(\omega t) \tag{3.10}$$

This is in the same form as Eq. 3.5, and the components of the equivalent complex displacement amplitude are given by

$$\begin{aligned} \bar{\mathbf{u}}_r(\mathbf{x}) &= \mathbf{r}(\mathbf{x})\cos(P(\mathbf{x})) \\ \bar{\mathbf{u}}_i(\mathbf{x}) &= \mathbf{r}(\mathbf{x})\sin(P(\mathbf{x})). \end{aligned} \tag{3.11}$$

27 node Hexahedral meshes can be created with the nodes arranged in a regular grid, so each voxel of data can be directly applied to a node in an appropriately scaled hexahedral FE mesh. This leads to MR-pixel level resolution in the reconstructed material properties, and avoids any interpolation errors. To overcome the difficulty creating a 27 node hexahedral element list from a grid of points, a mesh from the commercial meshing program Gambit$^{\text{TM}}$is used as a template. The steps involved in converting an MRI dataset to a FE mesh are briefly outlined below.

1. Create rectangular 27 node Hexahedral mesh in Gambit with at least as many nodes per side as there are voxels per side in the MRI dataset.

2. Scale mesh so that each dimension has a distance of 1 between adjacent nodes.

3. Shift mesh so the bottom corner is at $(1, 1, 1)$

4. Use the scaled, shifted mesh to assign each MRI voxel a corresponding mesh node.

5. Using the ROIPOLY function in the Matlab$^{\text{TM}}$image processing toolbox, define a region of interest (ROI) in the MRI dataset. Build up a list of all corresponding FE nodes which are inside the ROI.

6. Loop over all elements and build a list of all elements with all 27 nodes inside the ROI.

7. Build a list of all nodes in these elements, renumber the nodes and update the element list to reflect this renumbering.

8. Output FE node, element and displacement files. The MRI magnitude image is output in the same format as a material input file to allow it to be compared to the reconstructed property distributions.

If any node for a particular element is outside of the ROI, the entire element must be discarded. This can result in significant amounts of useful data being excluded, and is one of the drawbacks of using high order hexahedral elements. An example mesh, illustrating the MR-pixel based meshing is shown in Fig 3.1.

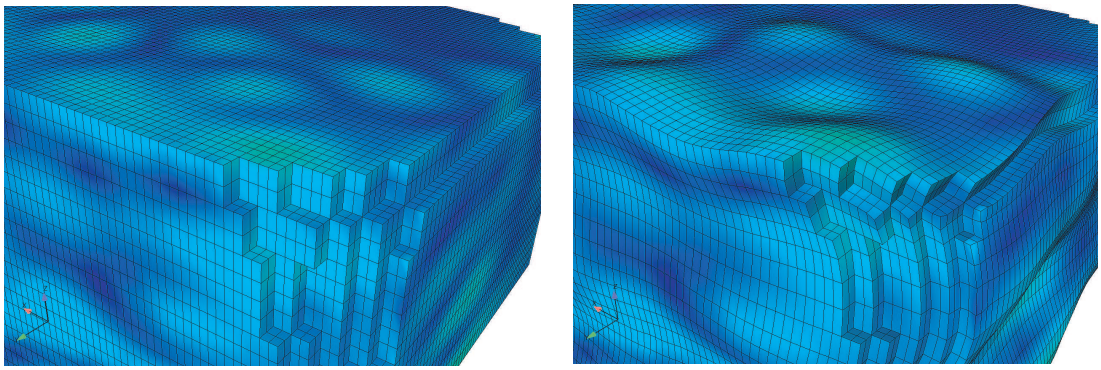

Figure 3.1 Example of an MR voxel based Finite Element mesh. The MR resolution is 1x1x2mm, which can be seen in the shape of the elements. Both images are colored by the displacement amplitude at $t = 0$, and the right image shows the displaced mesh.

3.3 Display of Results

The commercial visualization package Ensight^{TM}is used to visualize the results. The node, element, displacement and material property output files are first converted to the Ensight case gold format [42], and the results viewed using a combination of clip planes and isosurfaces.

Chapter 4

Global Rayleigh Parameter Reconstruction

An investigation into globally defined homogeneous Rayleigh parameter reconstruction was performed to give an indication how well a material property reconstruction algorithm will be able to detect differences in Rayleigh damping parameters. The damping ratio, given in Eq. 2.20, suggests the same level of damping can be obtained using only a complex shear modulus (CSM damping), and using only a complex density (CD damping), however the actual motion patterns in each of the two cases will differ. This investigation seeks to determine the level of this difference, and how successfully a reconstruction algorithm can use the difference to determine the Rayleigh damping parameters for a given material. A material with independently measured Rayleigh damping parameters is not available, therefore simulation studies were used. The investigation involved an analysis of the motion differences resulting from changes in damping parameters, along with globally defined damping parameter reconstructions using simulated displacement data.

4.1 Methods

4.1.1 Three Parameter Reconstruction Algorithm

A motion error minimization based inversion algorithm which fits globally defined values of μ_I and ρ_I to a set of complex-valued full-field time-harmonic motion data was created. A regularized Gauss-Newton method was used to minimize the error function

$$\Phi = (\mathbf{u}(\mu, \rho) - \mathbf{u}_m)^H (\mathbf{u}(\mu, \rho) - \mathbf{u}_m). \tag{4.1}$$

Here, $\mathbf{u}(\mu, \rho)$ is the calculated displacement vector at the current globally defined complex μ and ρ estimate, and $\mathbf{u}_m$ is the measured displacement vector. Both contain

displacements in all three coordinate directions. The superscript H indicates a complex conjugate transpose. The error can be converted to a relative error, given by

$$\Phi_p = \frac{(\mathbf{u}(\mu,\rho) - \mathbf{u}_m)^H(\mathbf{u}(\mu,\rho) - \mathbf{u}_m)}{\mathbf{u}_m^H \mathbf{u}_m}. \tag{4.2}$$

Details of the Gauss-Newton algorithm are given in section 2.3.2.

4.1.2 Variations With Constant ξ_d

For fixed ξ_d, the percentage motion difference between a set of motions from a material model with a given CSM/CD damping composition, $\mathbf{u}$ and motions from a material model with the same ξ_d composed of purely CSM damping, $\mathbf{u}_{CSM}$, is defined as:

$$\Psi = \frac{\|(\mathbf{u} - \mathbf{u}_{CSM})\|^2}{\|\mathbf{u}_{CSM}\|^2} \quad \times \quad 100. \tag{4.3}$$

A database of motions was generated in order to plot Ψ for a variety of damping ratios and CSM/CD damping compositions. An example of cases from this database is shown in Fig. 4.1. The CSM/CD composition was quantified using the percentage of ξ_d generated by CD damping, ξ_{cd}, given by

$$\xi_{cd} = \frac{-\rho_I}{2\rho_R \xi} \quad \times \quad 100. \tag{4.4}$$

The resulting plot, Fig. 4.2, gives a quantitative estimate of the sensitivity of the motions predicted by the Rayleigh model to changes in the CSM/CD composition at a given damping ratio. This estimate should give an indication of the accuracy with which a motion-difference minimization based algorithm can determine the correct damping parameters under a given amount of measurement noise. Parameter variations which cause a motion difference lower than the noise level should be difficult to detect, although the quantitative value of this estimate will limited by the differences between incoherent error from noisy measurements and coherent error resulting from variations in the Rayleigh parameters.

Values from Fig. 4.2 will be sensitive to changes in test parameters (e.g. frequency, real material property values, test geometry, boundary conditions etc.). In order to investigate how reliably these values can be applied to different geometries, materials and frequencies, a second plot was created of the percentage motion difference between purely CD and purely CSM damping at a range of values of shear wavelengths per side, given by:

$$WPS = \frac{L\omega}{2\pi}\sqrt{\frac{Re\{\rho^*\}}{Re\{\mu^*\}}} \tag{4.5}$$

This parameter relates the effects of frequency, ω, characteristic problem dimension, L (edge length in the cubic test geometry), and real material property values (μ and ρ) to a single term describing the number of waves within the sample. Normalization of different problem domains using the WPS parameter is useful because the number of waves within the domain roughly describes the amount of information about the internal mechanical properties that exists within the data. The size of variations in the motion difference values for a particular damping ratio as WPS varies will indicate the deviation which can be expected from values in Fig. 4.2 under different test conditions.

4.1.3 Simulation Studies

The ability of a reconstruction algorithm to determine the correct parameters for a Rayleigh damped material in practice was investigated by estimating the homogeneous Rayleigh damping parameters of a reference case using an optimization based global Rayleigh damping parameter reconstruction algorithm. Simulated motions were used as reference data to ensure the input data fits the behavior of a Rayleigh damped material. The progression of this iterative algorithm was plotted on top of the error domain, Φ to visually track the algorithm's behavior, using both uncorrupted reference data to investigate ideal conditions, and data modified by adding 5% gaussian distributed noise to more closely represent true MR detected input data.

A larger simulation study was also performed, four reconstructions with differing reference CSM/CD damping combinations were performed at each of four reference damping ratios. Real material property values were held constant. To simulate the effects of noise expected from MRI measurement, 5% gaussian noise was added to the reference data. An Armijo line search [43] was added to the optimization algorithm for this part of the study to accelerate convergence.

4.2 Results

4.2.1 Forward Solution Comparison

Equation 2.20 suggests that the same overall level of damping can be achieved by either using only complex shear modulus or only complex density. Figure 4.1 shows a comparison of the motions produced by purely CSM and purely CD damping with a highly damped inclusion present. Both cases have the same damping ratio distribution throughout the material.

4.2.2 Variations With Constant $\boldsymbol{\xi}_d$

Figure 4.2 shows a plot of the percentage motion difference, Ψ, as a function of the damping ratio, ξ_d, and the percentage of ξ_d made up of CD damping, ξ_{cd}. Fig. 4.3 shows

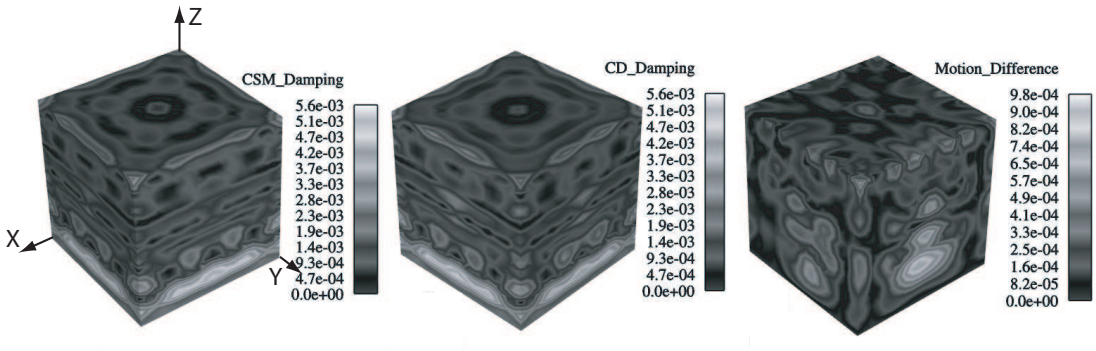

Figure 4.1 Left image: CSM Damping motion amplitude, $|u_{CSM}|$, $\xi_{d(background)} = 2.5\%$. A 40mm cubic inclusion is situated at the center of the bottom face with $\xi_{d(inclusion)} = 10 \times \xi_{d(background)}$ and no change in real parameters. Center image: CD Damping motion amplitude, $|u_{CD}|$, $\xi_{d(background)} = 2.5\%$, and an identical inclusion to the CSM case. Right Image: Motion difference, $|u_{CSM} - u_{CD}|$.

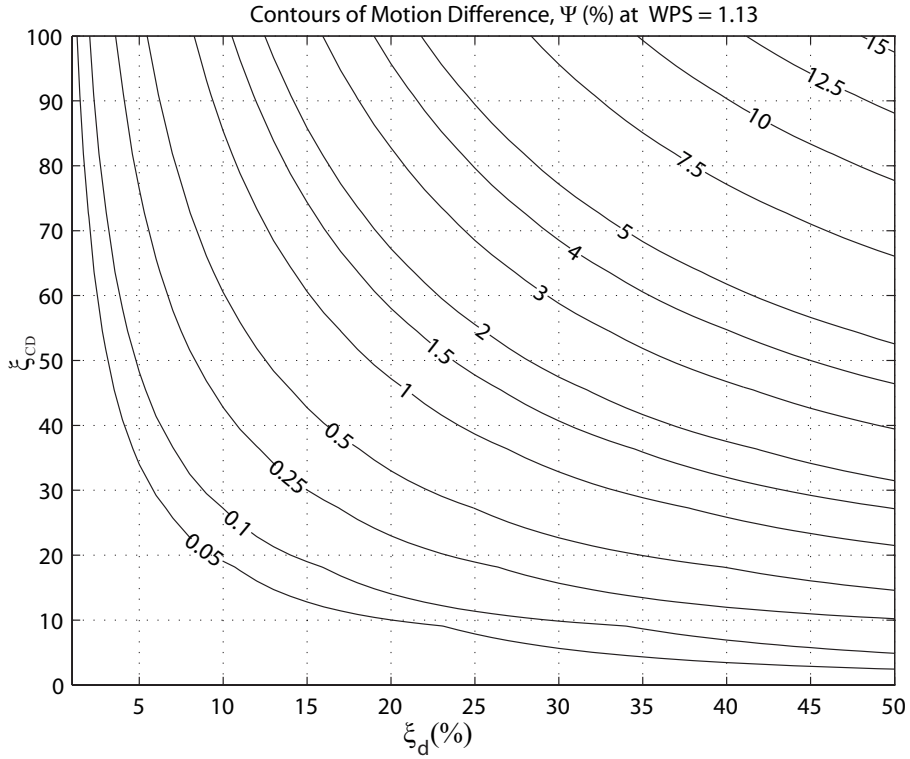

Figure 4.2 Contour plot of motion difference, Ψ (Eq. 4.3), as a function of damping ratio, ξ_d (Eq. 2.20), and percentage of ξ_d made up of CD damping, ξ_{cd}. This plot allows the motion difference to be estimated for a given damping ratio as the CSM/CD damping composition changes.

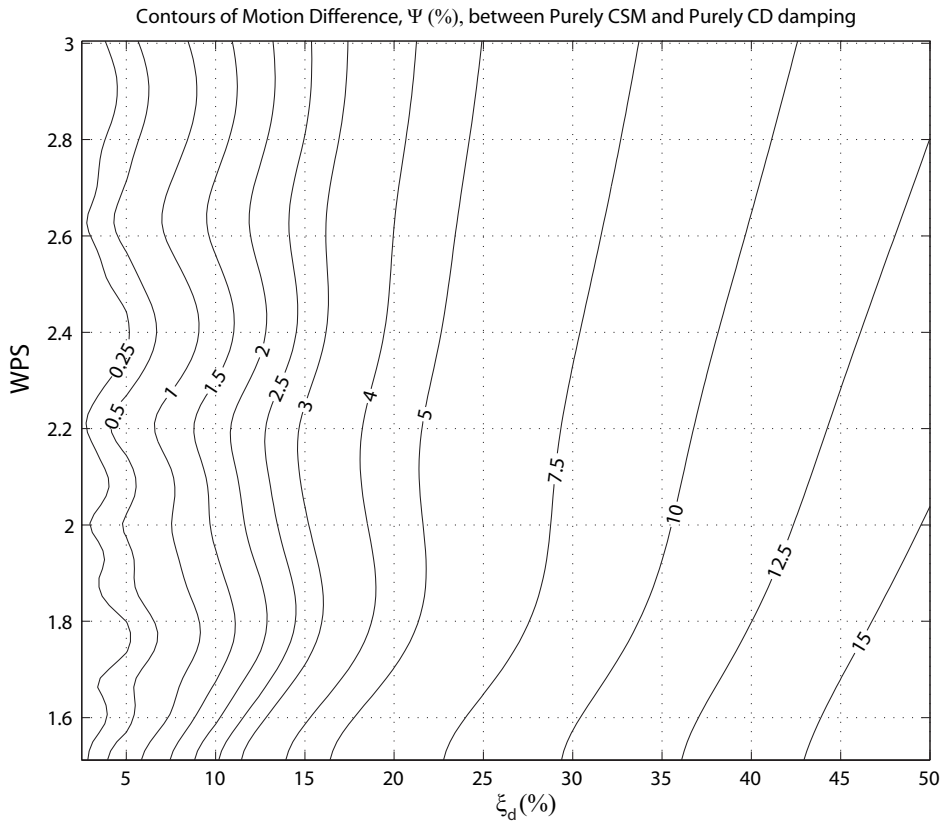

Figure 4.3 Contour plot of motion difference, Ψ (Eq. 4.3) between purely CD and purely CSM damping ($\xi_{cd} = 100\%$) as a function of damping ratio, ξ_d (Eq. 2.20), and shear wavelengths per side, WPS (Eq. 4.5). Values from this plot at a given WPS value are equivalent to those from a plot similar to Fig. 4.2 for $\xi_{cd} = 100\%$, generated at that particular WPS value. The variation in Ψ for a given ξ_d with WPS gives an indication of the variation in the values from Fig. 4.2 which can be expected as parameters such as $Re\{\mu\}, Re\{\rho\}, \omega$ and the geometry are altered.

a plot of Ψ at $\xi_{cd} = 100\%$, as a function of damping ratio, ξ_d, and shear wavelengths per side, WPS.

4.2.3 Simulation Study Results

The contours of Fig. 4.4 show the percentage error, Φ_p between calculated motions from a reference set of damping parameters (reference motions, marked with a star), and calculated motions from other values of damping parameters. Parameter updates for two typical global damping parameter reconstructions using the reference motions as measured data are also shown, both for the case of no noise as well as the case of 5% gaussian noise.

Simulation study results from 16 reconstructions with 5% noise are presented in Table 4.1. Initial guesses for all cases were arbitrarily chosen to be a 50-50 CSM/CD damping combination at a damping ratio 10% below the reference value. Real parameters were given as the reference values and not allowed to be adjusted by the algorithm. All reconstructions with $\xi_d = 40\%$ or greater failed due to the algorithm having difficulty finding a descent direction.

Table 4.1 Simulation study results. Reference and reconstructed parameters are given in the format ($\xi_d(\%)$, ξ_{cd}). Parameter errors given are the difference between reference and reconstructed values.

Parameters: (ξ_d, ξ_{cd}) (%)		Parameter Errors (%)	
Reference	Reconstructed	ξ_d	ξ_{cd}
(10, 0)	(9.96, 3.66)	0.04%	3.7%
(10, 30)	(9.97, 32.06)	0.03%	2.1%
(10, 70)	(9.98, 68.89)	0.02%	1.1%
(10, 100)	(9.96, 98.04)	0.04%	2.0%
(20, 0)	(20.03, -1.61)	0.03%	1.6%
(20, 30)	(20.01, 31.45)	0.01%	1.5%
(20, 70)	(20.02, 68.15)	0.02%	1.9%
(20, 100)	(20.00, 101.11)	0.00%	1.1%
(30, 0)	(29.98, 1.44)	0.02%	1.4%
(30, 30)	(30.00, 30.04)	0.00%	0.0%
(30, 70)	(29.96, 69.79)	0.04%	0.2%
(30, 100)	(29.84, 97.55)	0.16%	2.5%
(40, 0)	RECONSTRUCTION FAILED		
(40, 30)	RECONSTRUCTION FAILED		
(40, 70)	RECONSTRUCTION FAILED		
(40, 100)	RECONSTRUCTION FAILED		

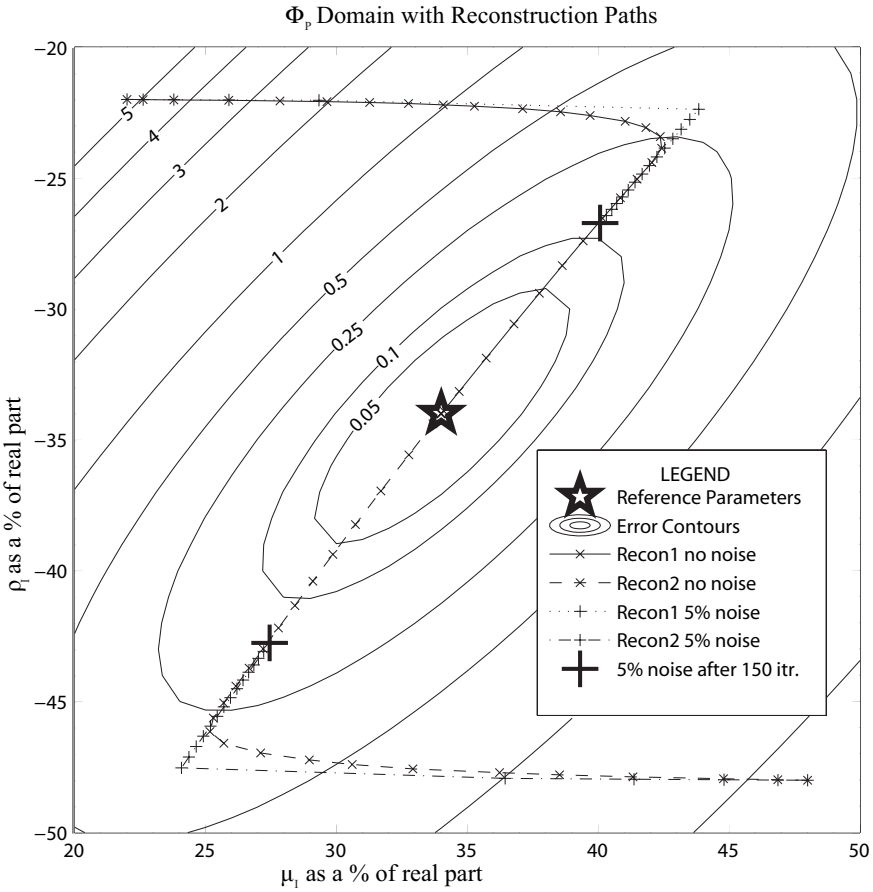

Figure 4.4 Rayleigh damping parameter percentage error domain, Φ_p with two typical reconstructions. Both of these reconstructions were run with both noise-free data and with data corrupted by adding 5% gaussian noise. Real parameter values were $Re\{\mu^*\} = 7000$, $Re\{\rho^*\} = 1020$. The contours show the noise-free error domain, the major axis of the elliptical contours represents a line of constant ξ_d. The various line types show the iterative progress of each of the 4 damping parameter reconstructions, and the reference parameters are marked with a star.

4.3 Discussion of Global Reconstructions

A comparison of the motion patterns produced by CSM and CD damping at the same damping ratio, shown in Fig. 4.1, reveals noticeable differences in the motions of up to about 15%. Figure 4.2 shows that these motion differences increase with higher damping ratios, which is in agreement with the results obtained by Semblat [44], and indicates using the most appropriate damping model to fit a Rayleigh damped material becomes increasingly important at higher levels of damping. This type of coherent motion pattern difference should theoretically allow a motion-error minimization based property reconstruction algorithm to determine the relative levels of each of the damping parameters for a given material.

Figure 4.2 shows that motion difference also increases with the level of the discrepancy in Rayleigh parameter composition. The actual values from the figure should give an estimate of how well a motion-error minimization based reconstruction algorithm can differentiate relative levels of each damping parameter, based on the idea that a particular level of motion difference will likely become undetectable if the same or greater level of measurement noise is present. However, the differences between coherent errors from parameter variation and incoherent errors from noise limit the quantitative value of this comparison. An indication as to how reliably values from this plot can be applied to similar cases is given by Fig. 4.3, which reveals variation in the motion difference with respect to the number of shear wavelengths per side that can be attributed to resonance-related effects. While the impact of resonance is reduced by the presence of damping, the motions at resonant frequencies remain significantly higher than at non-resonant frequencies. Figure 4.3 suggests the plot in Fig. 4.2 can be used as a guide to the expected parameter sensitivity levels, but variations of between 0.5 and 3% can be expected, depending on the size of the damping ratio.

The error domain shown in Fig. 4.4 shows elliptical contour lines, with the major axis along a line where the damping ratio, ξ_d is equal to the reference case. These contours become more elongated as the reference damping ratio decreases due to increasing similarity between the two damping models at equal values of ξ_d. The reconstruction paths show the algorithm quickly approaches the correct damping ratio, and only then begins adjusting to the correct combination of damping parameters, indicating the actual combination of the two types of damping only becomes significant once the correct damping ratio has been found. The much larger adjustment in imaginary shear modulus in the early iterations is likely to be due to differences in the sensitivity derivatives for μ and ρ [17]. $\frac{\partial u}{\partial \rho}$ is much smaller than $\frac{\partial u}{\partial \mu}$, which causes the algorithm to preferentially adjust μ over ρ.

The reconstruction results presented in table 4.1 show that the correct combination of globally defined Rayleigh parameters can be accurately determined in simulation tests with noise levels comparable to MR-measured data. The algorithm had difficulty

satisfying the Armijo linesearch sufficient descent condition at a damping ratio of 40% . A damping ratio this large causes very high levels of motion attenuation, so the added noise would have a greater effect on the smoothness of the error domain, affecting the performance of the linesearch. Reconstructed values of the damping ratio, ξ_d, showed very high accuracy, correct to within 0.04% in all but one successful reconstruction. Reconstructed results for the Rayleigh parameter combination, defined by ξ_{cd}, were also quite accurate (within 4% of the true values for all successful reconstructions), although not as accurate as the reconstructed values of ξ_d. The elliptical error domain contours of Fig. 4.4 show that ξ_d is the dominant damping parameter, and the Rayleigh parameter combination is a secondary effect, which explains the difference in accuracy of the reconstructed values of ξ_d and ξ_{cd}.

At the damping ratios used in the simulations, Fig. 4.2 shows that the motion difference, Ψ, with changes of around 4% in ξ_{cd} is much smaller than the noise level of 5%. This would indicate such variations would be very difficult to detect under 5% noise. The fact that the algorithm could estimate parameters to this accuracy may be due to the statistical nature of gaussian noise, together with the low ratio of number of reconstructed parameters to number of noisy measurements.

Damping effects *in-vivo* occur due to complex interactions between microstructural tissue elements. Any continuum model can therefore only hope to provide an approximation of the attenuation behavior of actual tissue. Other factors such as material non-linearity also act to reduce resonant effects, however it is hoped that the two-parameter Rayleigh model is a step closer toward accurate characterization of tissue damping. It is recognized that simulation experiments are a poor substitute for *in-vivo* experiments in general, but are used here to illustrate some of the basic behavior of the Rayleigh damping model from a reconstruction perspective in a more controlled environment. Independent experimental measurement of Rayleigh damping parameters will also prove difficult, so testing the algorithm on a phantom with known material properties for verification is not possible at this stage.

The differences between damping related to elastic forces (CSM damping), and damping related to inertial effects (CD damping) suggest that the behavior of a Rayleigh damped material cannot be accurately captured by considering only one damping component. A method which accounts for both aspects of the damping model is required, especially at higher damping ratios. Differences between CSM and CD damping are large enough to allow a motion difference minimization based reconstruction algorithm to accurately estimate the correct combination of Rayleigh damping parameters using simulated data with noise levels that are comparable to those expected from MR measurements.

The large amount of measured data obtained from an MRI scan should allow estimation of the distribution of multiple material properties. At this stage one of the

barriers to the widespread use of MRE is the cost of the initial scan to obtain the motion dataset. Exactly which parameters will be of use in clinical diagnosis is not certain at this point, but extracting two damping parameters from a dataset instead of just one may provide an additional diagnosis tool at little extra cost.

Chapter 5

Distributed Material Property Reconstruction

5.1 Nodally Distributed Reconstruction Results

This section presents reconstruction results using the subzone based nodal basis algorithm.

5.1.1 Artefact resulting from one parameter damping model

If CSM damping is used to model damping effects better described by CD damping or vice-versa, the damping ratio equation (Eq. 2.20) indicates that the same level of damping can be achieved by either damping model. A closer analysis reveals this situation will actually result in an artefact related to the ratio of the displacements and their second derivatives. A mathematical prediction is given in this section, which is verified through a purely complex shear modulus reconstruction using simulated motion data generated using purely complex density.

The general time-harmonic wave equation in 1D, which the elastic wave equation is an example of, is given by:

$$\frac{\partial E(x)}{\partial x}\frac{\partial \bar{u}(x)}{\partial x} + E(x)\frac{\partial^2 \bar{u}(x)}{\partial x^2} + \rho(x)\omega^2 = 0, \tag{5.1}$$

where $E(x)$ represent a stiffness distribution, $\rho(x)$ is a density distribution, and $\bar{u}(x)$ is the time-harmonic motion amplitude, so that $u(x,t) = \mathfrak{Re}\{\bar{u}(x)e^{i\omega t}\}$. Allowing both E and ρ to be complex in Eq. 5.1, where $E(x) = E_R(x)+iE_I(x)$ and $\rho(x) = \rho_R(x)+i\rho_I(x)$ gives the Rayleigh Damping equation. Setting $\rho_I(x) = 0$ gives the complex shear modulus (CSM) damped equation:

$$\frac{\partial E_R(x)}{\partial x}\frac{\partial \bar{u}(x)}{\partial x} + i\frac{\partial E_I(x)}{\partial x}\frac{\partial \bar{u}(x)}{\partial x} + E_R(x)\frac{\partial^2 \bar{u}(x)}{\partial x^2} + iE_I(x)\frac{\partial^2 \bar{u}(x)}{\partial x^2} + \rho_R(x)\omega^2\bar{u}(x) = 0, \tag{5.2}$$

Similarly, setting $E_I(x) = 0$ gives the complex density (CD) damped equation:

$$\frac{\partial E_R(x)}{\partial x}\frac{\partial \bar{u}(x)}{\partial x} + E_R(x)\frac{\partial^2 \bar{u}(x)}{\partial x^2} + \rho_R(x)\omega^2\bar{u}(x) + i\rho_I(x)\omega^2\bar{u}(x) = 0. \tag{5.3}$$

If we wish to model one type of damping using the other, equating the real and imaginary parts of Eqs. 5.2 and 5.3 will give the required damping parameter distribution. As a simple example, suppose we were to use a CD model to mimic the effect of a CSM model with all parameters homogeneous in the domain, ie $E_R(x) = \bar{E}_R$, $E_I(x) = \bar{E}_I$ and $\rho_R(x) = \bar{\rho}_R$. Using the same constant $\bar{E}_R$ and $\bar{\rho}_R$ in the CD equation (5.3), equating real parts of Eqs. 5.2 and 5.3 gives:

$$\begin{aligned}\bar{E}_R\,\mathfrak{Re}\{\frac{\partial^2 \bar{u}(x)}{\partial x^2}\} - \bar{E}_I\,\mathfrak{Im}\{\frac{\partial^2 \bar{u}(x)}{\partial x^2}\} + \bar{\rho}_R\,\omega^2\mathfrak{Re}\{\bar{u}(x)\} = \\ \bar{E}_R\,\mathfrak{Re}\{\frac{\partial^2 \bar{u}(x)}{\partial x^2}\} + \bar{\rho}_R\,\omega^2\mathfrak{Re}\{\bar{u}(x)\} - \rho_I(x)\omega^2\mathfrak{Im}\{\bar{u}(x)\},\end{aligned} \tag{5.4}$$

and equating imaginary parts gives:

$$\begin{aligned}\bar{E}_R\,\mathfrak{Im}\{\frac{\partial^2 \bar{u}(x)}{\partial x^2}\} + \bar{E}_I\,\mathfrak{Re}\{\frac{\partial^2 \bar{u}(x)}{\partial x^2}\} + \bar{\rho}_R\,\omega^2\mathfrak{Im}\{\bar{u}(x)\} = \\ \bar{E}_R\,\mathfrak{Im}\{\frac{\partial^2 \bar{u}(x)}{\partial x^2}\} + \bar{\rho}_R\,\omega^2\mathfrak{Im}\{\bar{u}(x)\} + \rho_I(x)\omega^2\mathfrak{Re}\{\bar{u}(x)\}.\end{aligned} \tag{5.5}$$

Solving these equations for $\rho_I(x)$ gives:

$$\rho_I(x) = \bar{E}_I\frac{\mathfrak{Im}\{\frac{\partial^2 \bar{u}(x)}{\partial x^2}\}}{\omega^2\mathfrak{Im}\{\bar{u}(x)\}} = \bar{E}_I\frac{\mathfrak{Re}\{\frac{\partial^2 \bar{u}(x)}{\partial x^2}\}}{\omega^2\mathfrak{Re}\{\bar{u}(x)\}}. \tag{5.6}$$

Simple displacement patterns of the form $\bar{U}(x) = \hat{U}e^{ikx}$ satisfy

$$\frac{\mathfrak{Re}\{\frac{\partial^2 \bar{u}(x)}{\partial x^2}\}}{\mathfrak{Re}\{\bar{u}(x)\}} = \frac{\mathfrak{Im}\{\frac{\partial^2 \bar{u}(x)}{\partial x^2}\}}{\mathfrak{Im}\{\bar{u}(x)\}} = \frac{\frac{\partial^2 \bar{u}(x)}{\partial x^2}}{\bar{u}(x)} = \text{constant}, \tag{5.7}$$

but more complex displacement patterns may not, indicating an exact match is not possible. In the general 3D case, the equivalent ratios to those in Eq. 5.6 will vary spatially, therefore the best match for a constant value of one damping parameter will be a spatially varying distribution of the other. This effect could introduce artefacts in the reconstructed damping property field if a one parameter model was used to fit a material better described by a two parameter Rayleigh model.

These simulation tests are used to verify this prediction. Figure 5.1 shows the result of reconstructing each Rayleigh damping parameter on its own to fit reference motions generated using damping resulting purely from a homogeneous imaginary density. Similarities between the motion patterns and damping ratio images resulting from reconstructing the 'wrong' damping parameter (imaginary shear modulus) are obvious,

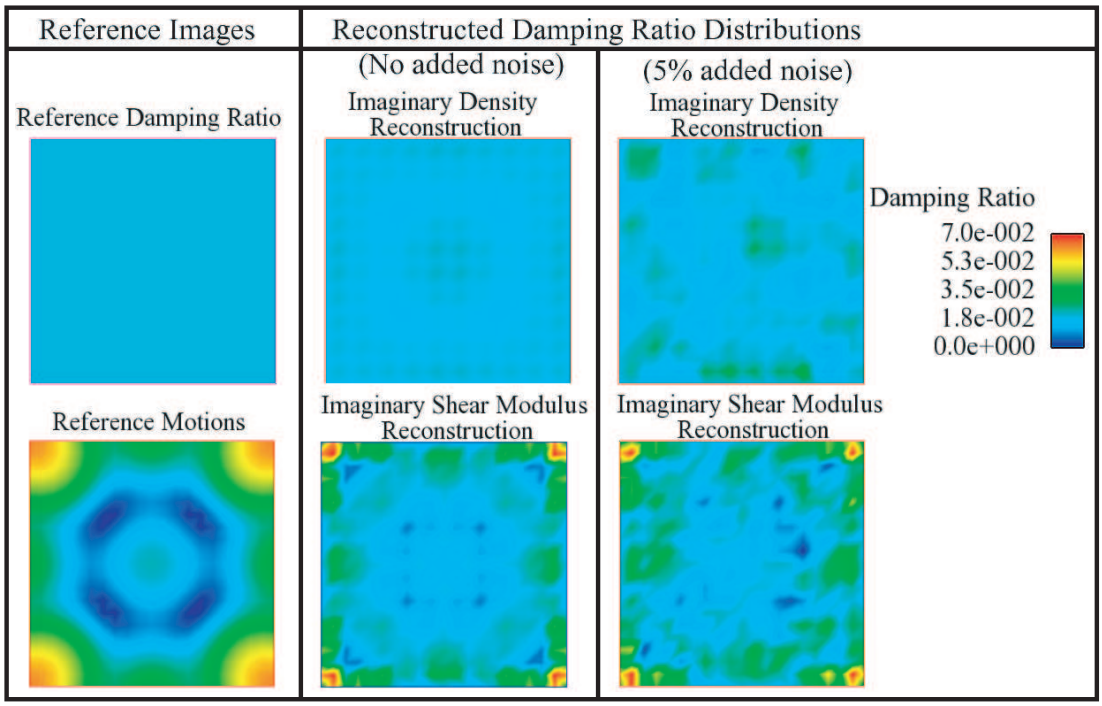

Figure 5.1 Cross-sections of 3D data. The images on the left show the damping ratio and motion amplitude of the reference case (Homogeneous, $\xi_d = 0.02$, Imaginary density damping). The center images show reconstructions of the damping ratio distribution with no noise added to the data, the upper image is the result of reconstructing only an imaginary density, and the lower image shows the result of only reconstructing an imaginary shear modulus. The right images show the same reconstructions as the center images, with 5% gaussian noise added to the input motion data. case.

whereas the damping ratio images resulting from reconstructing the correct damping parameter (imaginary density) give a much smoother distribution, which is not related to the motion patterns.

5.1.2 Reconstructions of Gelatine Phantoms

The ability of the reconstruction program to produce correct results using real data is demonstrated through these reconstructions of tissue-mimicking gelatine phantoms. These phantoms are constructed with inclusions of gelatine with a higher stiffness than the background material, which are marked using a contrast agent to make them visible in the MR signal image. The phantoms are actuated at 100Hz using a piezoelectric mechanical actuator, and the motions measured using phase-contrast MRI. A photo of the experimental setup used by the group at Dartmouth College is given in Fig. 5.2.

The reconstructions presented use a variety of settings for the various options in the code, much more testing will be required to find the optimal configuration. As a

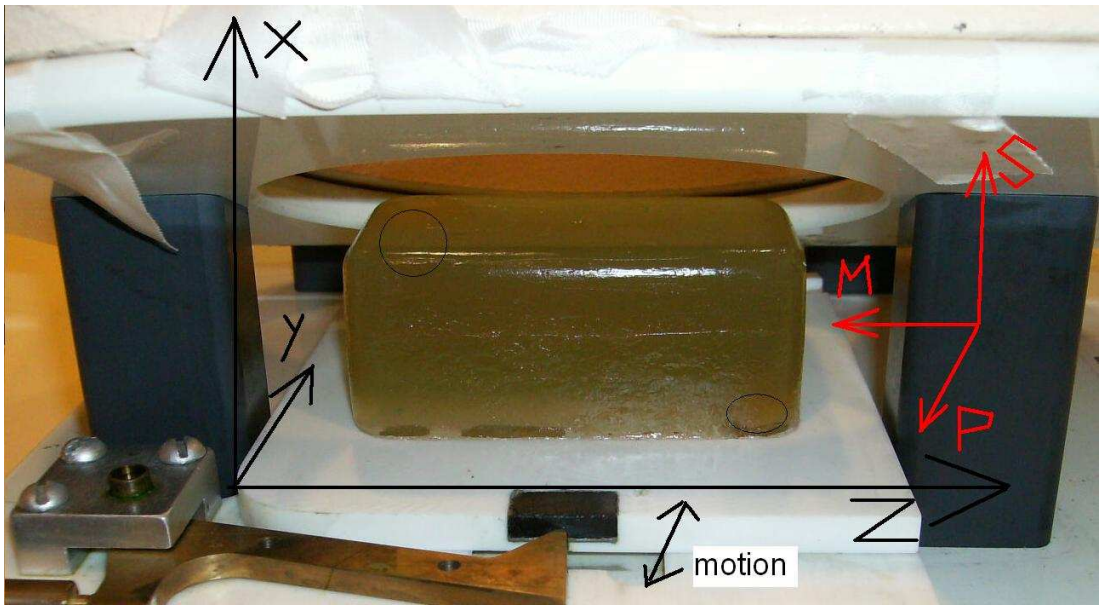

Figure 5.2 MRI motion capture setup. The physical xyz coordinate system is shown in black, and the scanner mps coordinate system is in red. The mechanical linkage used to increase the motion amplitude produced by the piezoelectric actuator is visible at the bottom of the image. Image courtesy of Dartmouth College, NH, USA.

guide, values for these parameters which seem to produce the best results are given below:

Subzone Size: As close to cubic as possible, with about 2000 nodes per zone. This is the factor with the greatest influence on results.

Subzone Overlap: $15 - 20$ %.

Initial guess: $\mathfrak{Re}\{\mu\}$ within 20-30% of the background values, $\mathfrak{Re}\{\rho\} = 1000\text{kgm}^{-3}$, low values for imaginary parts (e.g. 5% of real part), 10^8 for bulk modulus.

Material Property Bounds: Physically unrealistic values, applied at the material property update level.

Total Variation Weight: Start low, end high (eg $10^{-10} \rightarrow 10^{-7}$).

Spatial Filtering Level: Start high, end low (eg $0.4 \rightarrow 0.1$).

Iteration limits: Global iterations: Until material property solution approaches convergence (60+ for CG), Iterations per zone: Low (e.g. 4).

5.1.2.1 Spheres Inclusion

This phantom had two spheroidal inclusions of stiffer material in opposite corners. The total number of nodes in the mesh is 163,069. Runtime for 100 global iterations with 3 CG iterations per subzone on 22 1.9GHz processors was about 3 days. Comparisons of the MR signal-strength image and the reconstructed real shear modulus distribution are given in Figure 5.3. A significant artefact is marked with a black arrow.

Damping parameter reconstruction results are given in Figure 5.4, which shows the distribution of both the damping ratio, and Rayleigh Composition, which is defined as the proportion of the damping ratio made up of damping resulting from an imaginary shear modulus, ξ_{csm}.

A comparison of the MR-detected reference motions and the reconstructed values is given in Figure 5.5

5.1.2.2 Cones Inclusion

This phantom had two conical inclusions of stiffer material in opposite corners. Comparisons of the MR signal-strength image and the reconstructed real shear modulus distribution are given in Figure 5.6. The total number of nodes in the mesh is 24,633. Runtime for 100 global iterations with 3 CG iterations per subzone on 18 1.9GHz processors was about 24 hours. Some example damping parameter reconstructions are also given in Figure 5.7.

5.1.3 *In-vivo* Results

Some initial *in-vivo* Rayleigh damped reconstruction results are presented here. MR-detected time-harmonic motion (85Hz) data was obtained from Dartmouth College, and the real shear modulus, damping ratio and Rayleigh composition distributions were reconstructed using 120 global iterations of the nodal basis subzone algorithm, with 3 CG iterations per subzone. Initial guesses for material properties were $\mu = 4000 + 100i$, $\rho = 1000 - 20i$, and $K = 10^8$. Total variation minimization weighting was $10^{-11} \rightarrow 10^{-7}$, and spatial filtering $0.4 \rightarrow 0.1$. Total number of nodes in the dataset was 10,437, subzone geometry parameters were set to give approximately 2500 nodes per subzone.

Areas of fibroglandular and fatty tissue are distinguishable in the T2* weighted MR magnitude images, fatty tissue shows up as relatively homogeneous grey regions, whereas fibroglandular tissue is generally darker and has greater variability. An approximate manual thresholding of each type of tissue in the MR image is shown in Fig. 5.8. Values given in the literature for the stiffness of the regions of fibroglandular and fatty tissue types distinguishable on the T2* weighted MR magnitude image vary, how-

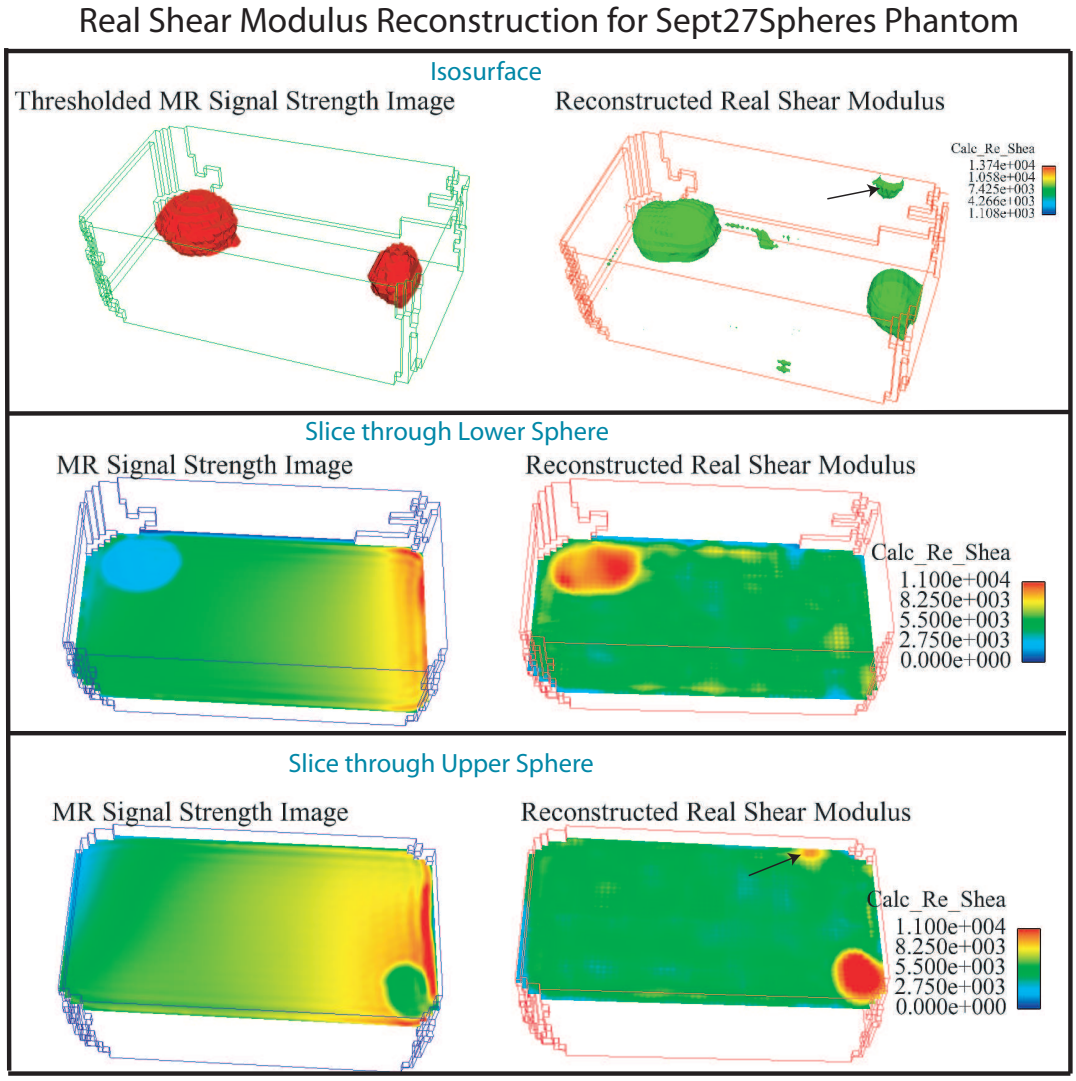

Figure 5.3 Real Shear modulus reconstructions for Sept27-Spheres 64x64 gelatine phantom dataset. The spheroidal inclusions are visible in the MR Signal strength image due to the addition of a contrast agent to the stiffer gelatine. The top images show a 3-dimensional isosurface, the middle images are a clip plane through the larger, lower inclusion, and the lower images show a clip plane through the smaller, upper inclusion. The black arrow marks an artefact on the problem boundary.

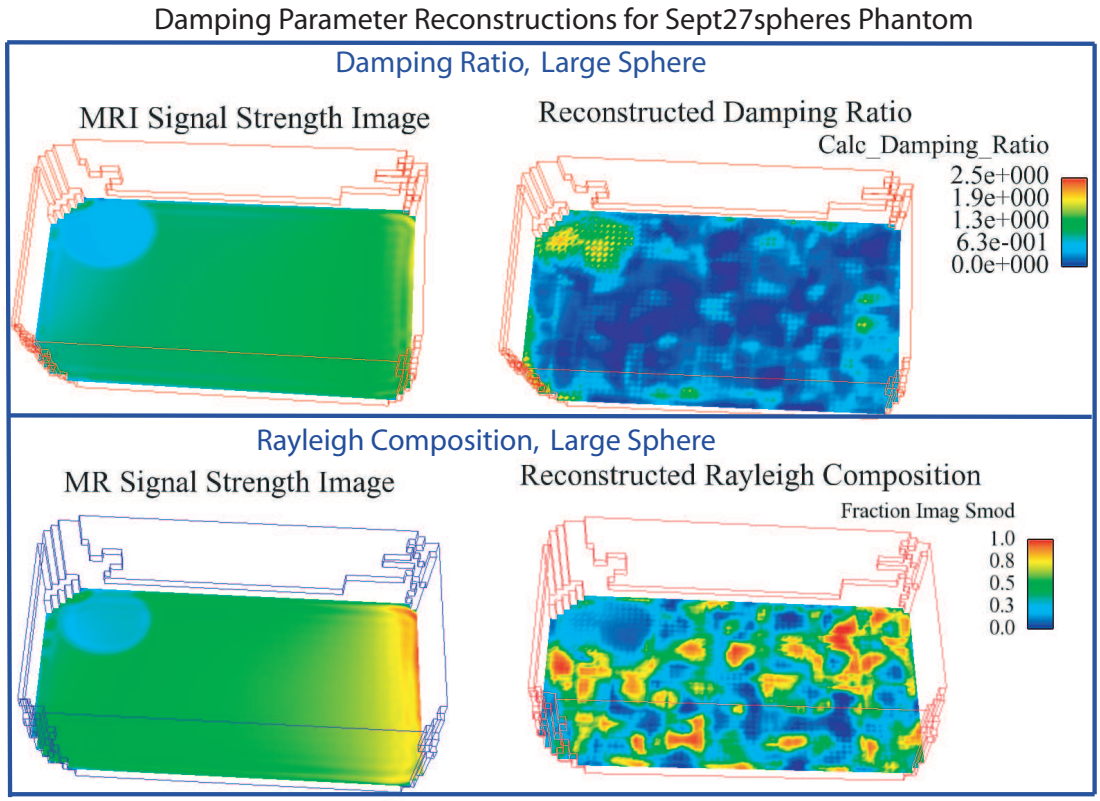

Figure 5.4 Damping Parameter reconstructions for Sept27-spheres 64x64 gelatine phantom dataset. The upper images show a clip plane with the reconstructed damping ratio distribution, and the lower images show the fraction of ξ_d made up of a complex shear modulus, ξ_{csm} (Eq. 2.21). Both of these images are a clip plane through the larger, lower inclusion.

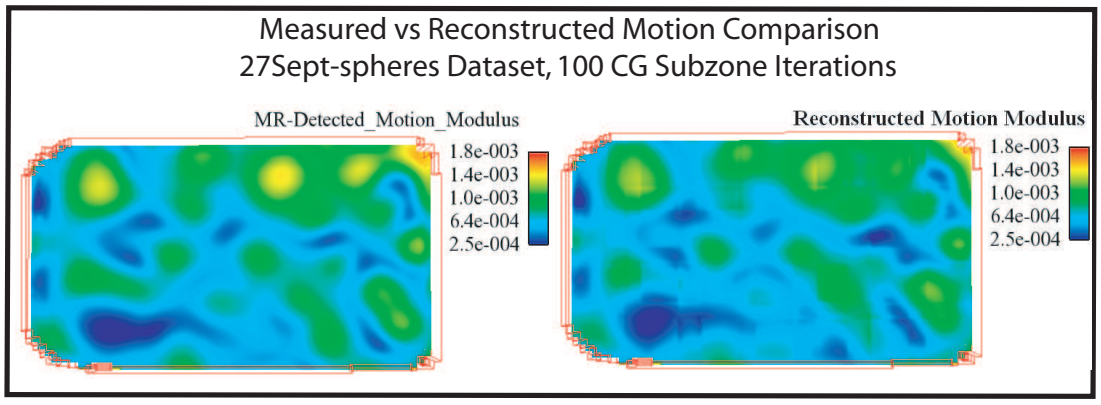

Figure 5.5 Measured and reconstructed motion comparison. The images show the modulus of the complex-valued motion amplitude, measured on the left and reconstructed values on the right.

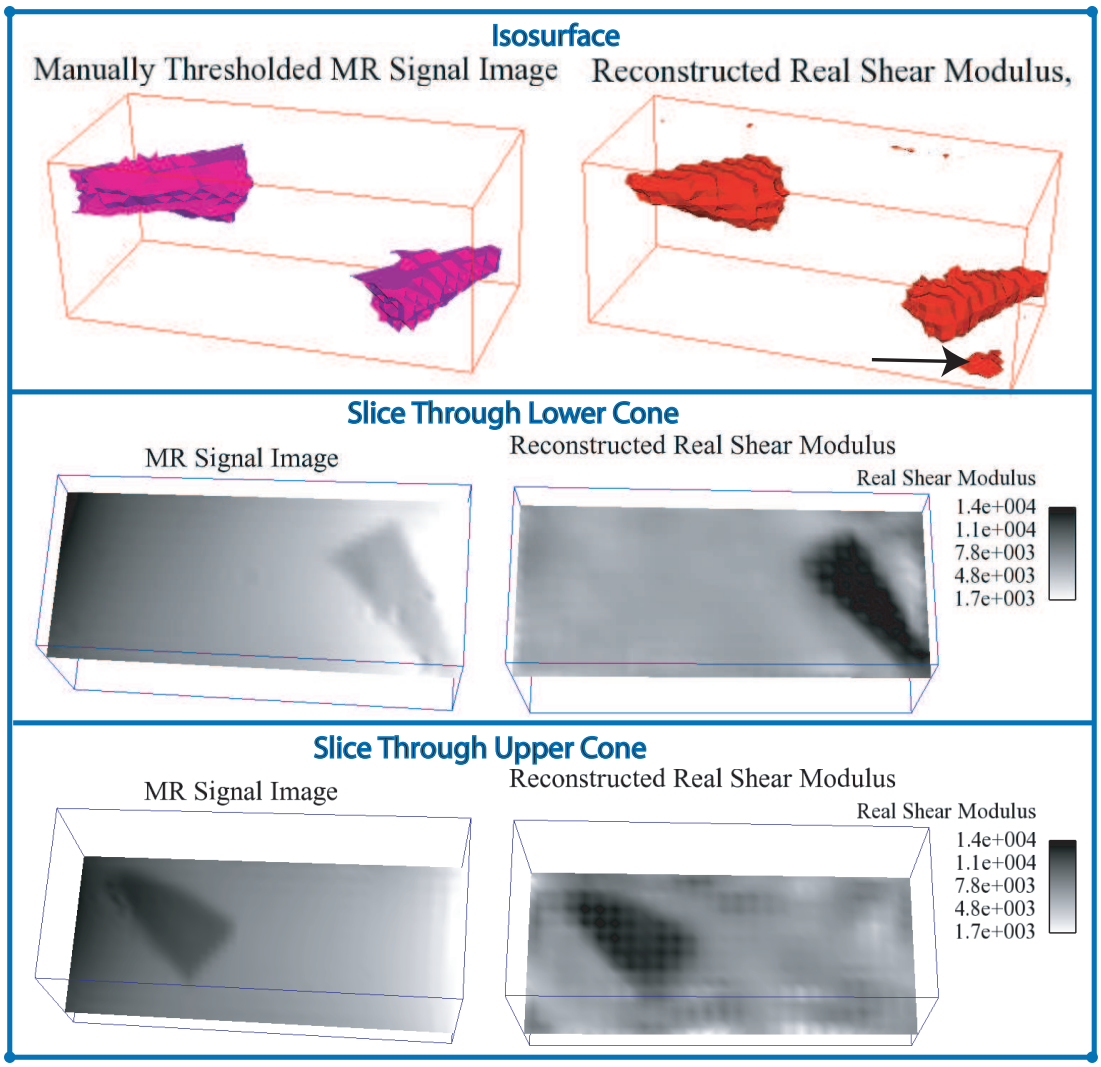

Figure 5.6 Real Shear modulus reconstructions for Oct-11 cones gelatine phantom. The conical inclusions are visible in the MR Signal strength image due to the addition of a contrast agent to the stiffer gelatine. The top images show a three-dimensional isosurface, the middle images are a clip plane through the lower cone, and the lower images show a clip plane through the upper cone. The black arrow marks an artefact on the problem boundary.

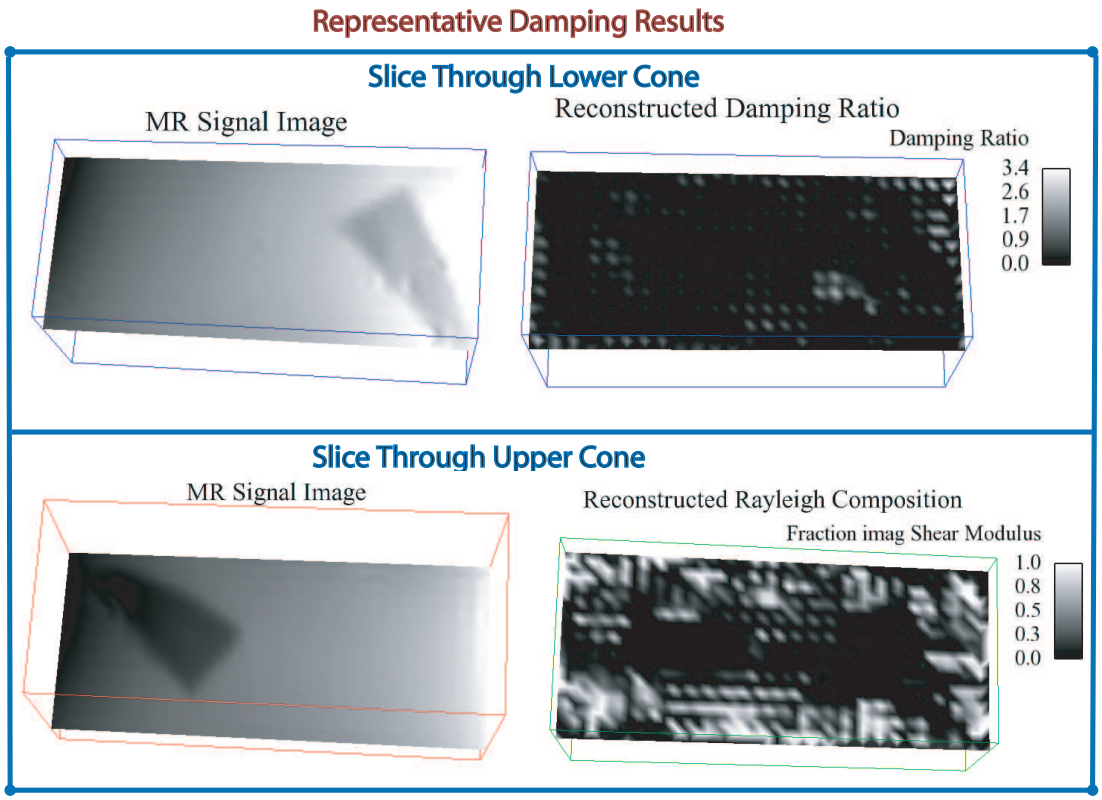

Figure 5.7 Representative Damping Parameter reconstructions for Oct11-cones 64x64 dataset. The upper images show a clip plane through the lower cone and the damping ratio distribution, and the lower images show the fraction of ξ_d made up of a complex shear modulus, ξ_{csm}, on a clip plane through the upper cone. (Eq. 2.21).

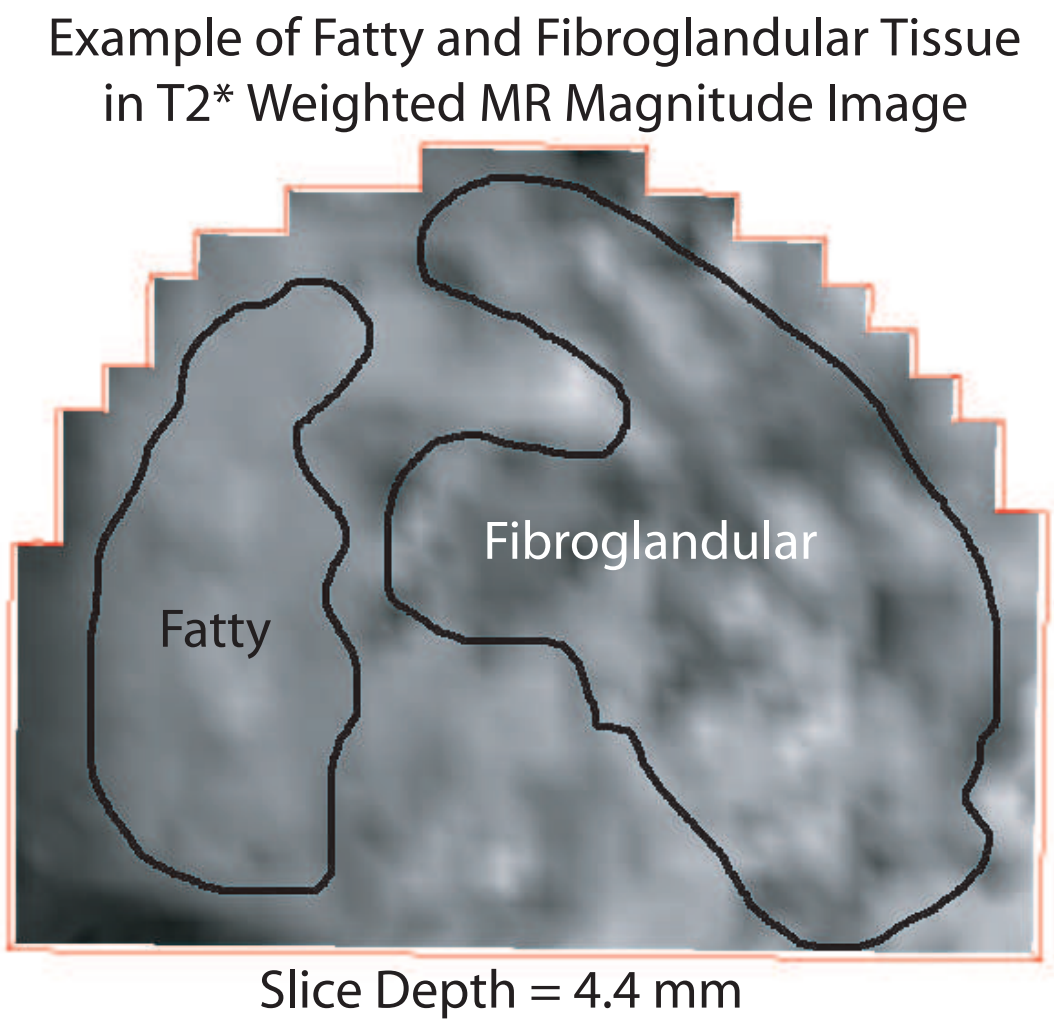

Figure 5.8 Example of manual segmentation of a T2* weighted MR magnitude image into regions of fatty and fibroglandular tissue. Outside these regions, the tissue type is difficult to distinguish, and is left unspecified.

ever most MRE results published have shown higher stiffness values for fibroglandular tissue compared with fat [9].

Figures 5.9 and 5.10 give a comparison of the T2* weighted MR magnitude image with the reconstructed distributions of all three imaged mechanical properties. Results for four different slices are given, the slice at 0mm is on the boundary of the data.

Figure 5.11 shows contours of constant reconstructed properties, plotted on top of the T2* weighted MR magnitude image. A close up version of a particular region of interest with contours of high ξ_{csm} is given in Fig. 5.12.

Approximate values of the reconstructed material properties for each type of tissue were found using manual segmentation of obvious areas of fatty and fibroglandular

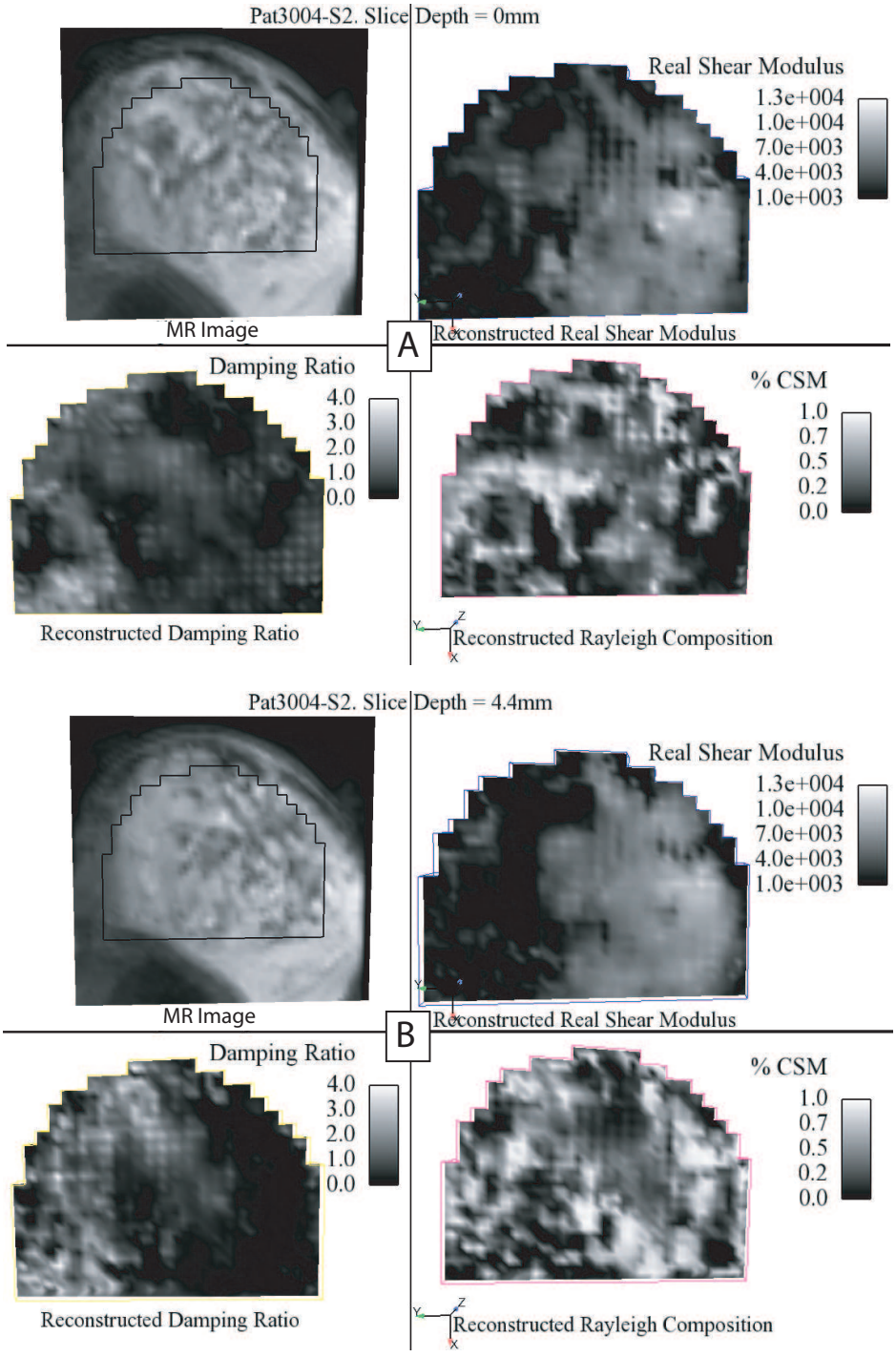

Figure 5.9 Patient 3004S2, slices at 0 and 4.4mm: A comparison of the T2* weighted MR images with the reconstructed distributions of real shear modulus, damping ratio (Eq 2.20), and Rayleigh damping composition, in terms of ξ_{csm} (Eq. 2.21). The images for a slice depth of 0mm represent reconstructions on the boundary of the data, whereas the slice at 4.4mm shows internal data.

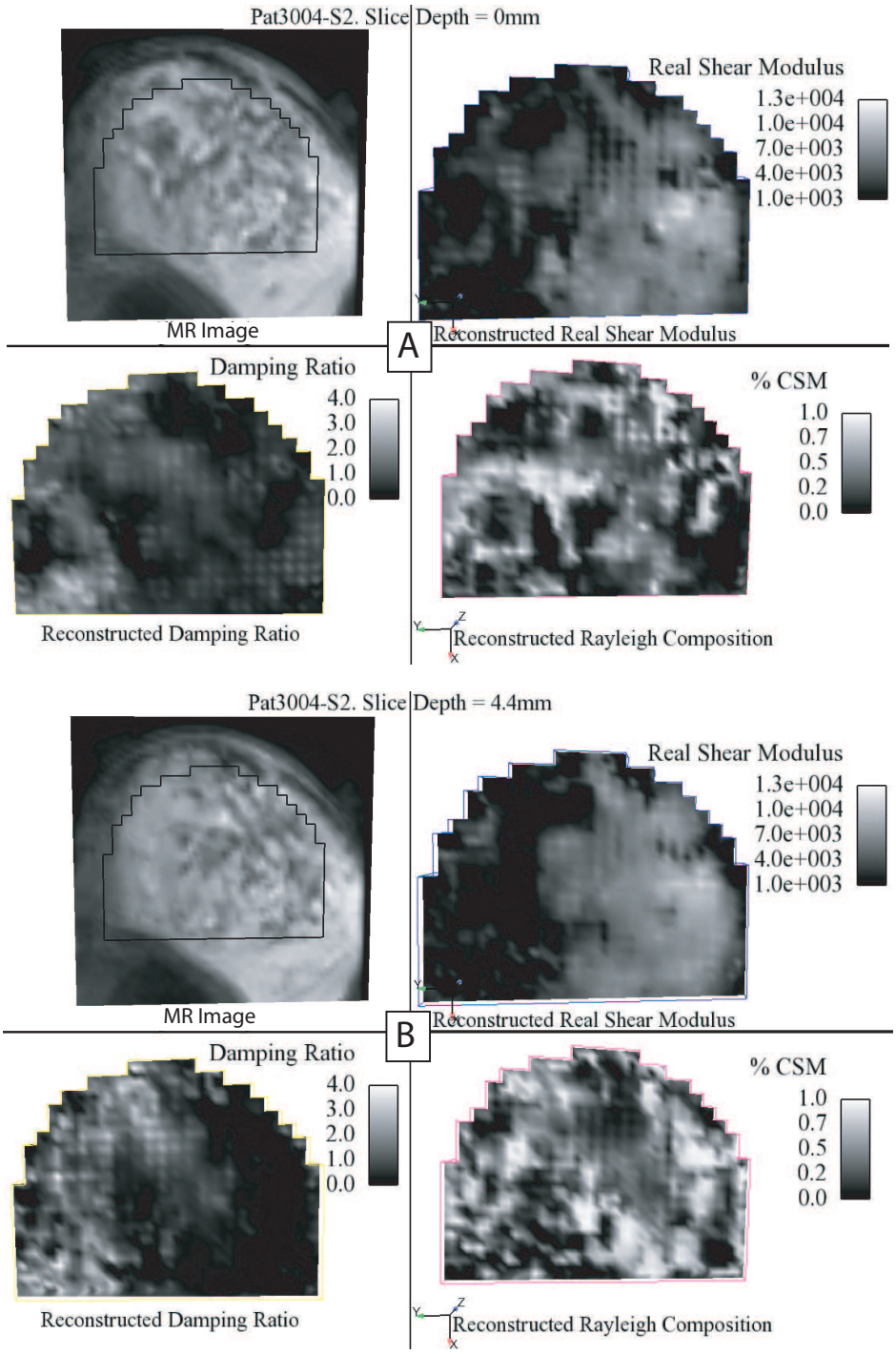

Figure 5.10 Patient 3004S2, slices at 8.8 and 11mm: A comparison of the T2* weighted MR images with the reconstructed distributions of real shear modulus, damping ratio (Eq 2.20), and Rayleigh damping composition, in terms of ξ_{csm} (Eq. 2.21). Both slices represent internal sections of data.

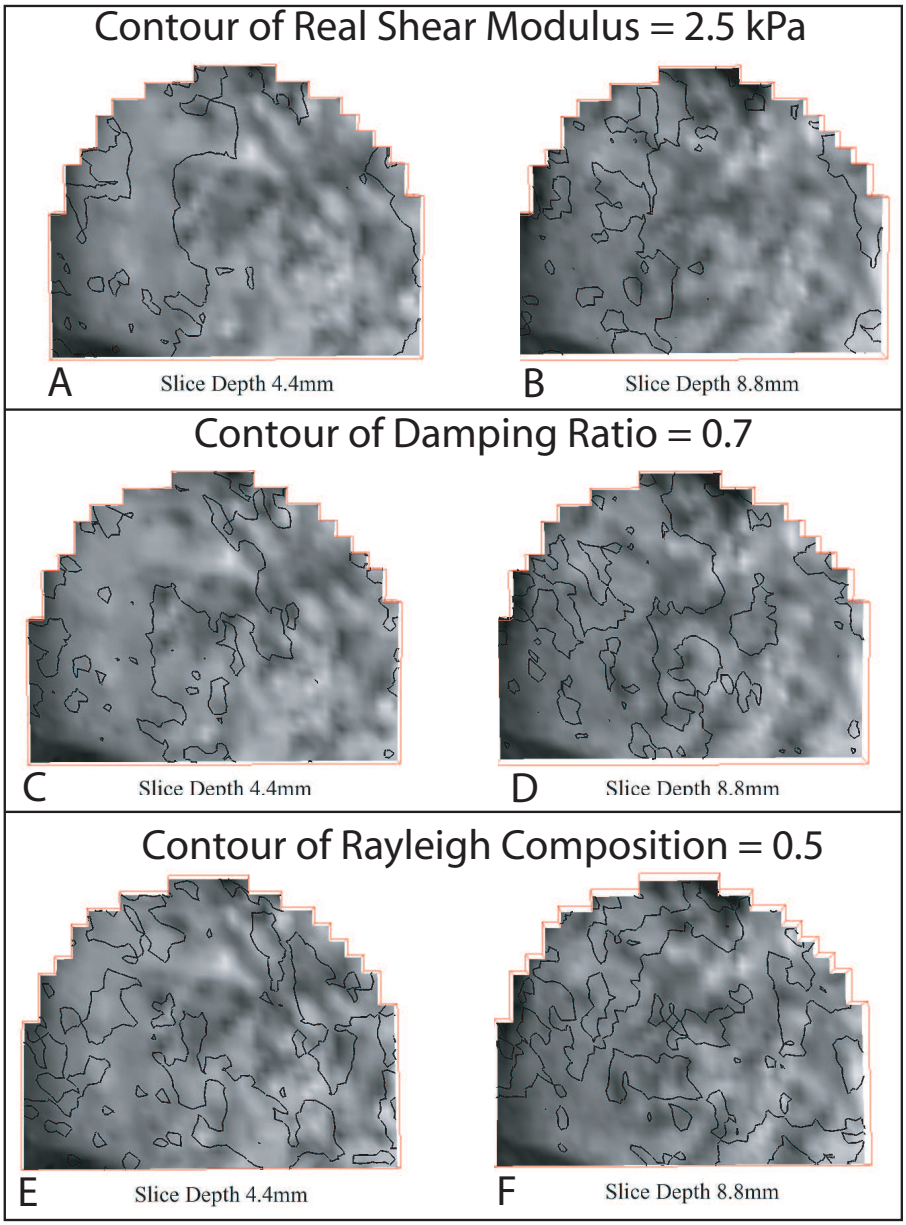

Figure 5.11 Patient 3004S2: Contours of $\mathfrak{Re}\{\mu\} = 2.5$kPa, $\xi_d = 0.7$, and $\xi_{csm} = 0.5$ plotted on top of the corresponding T2* weighted MR magnitude image. Slices of internal data at a depth of 4.4 and 8.8mm are shown.

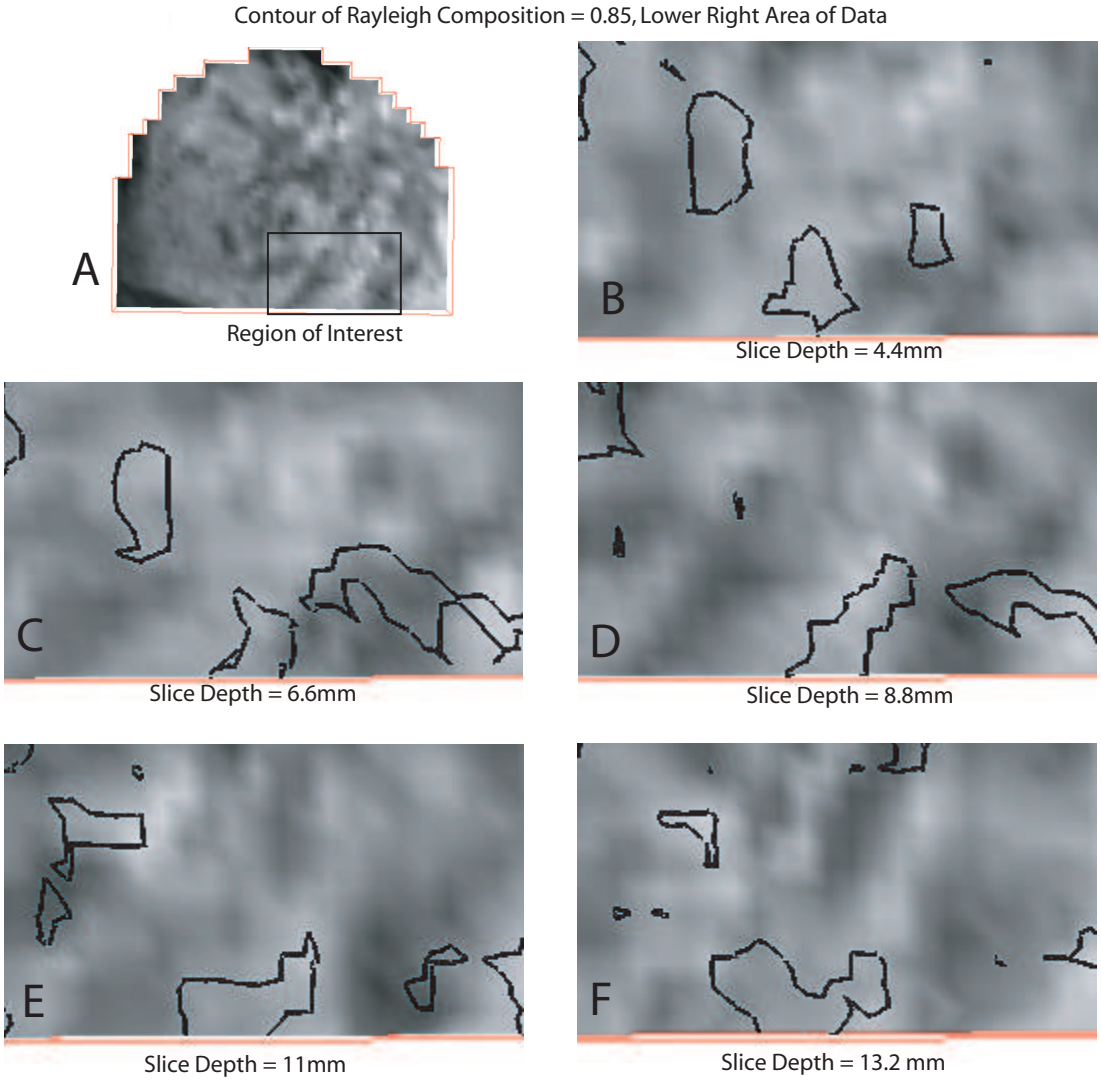

Figure 5.12 Patient 3004S2: Close up view of region of interest. Image A shows the location of the region, and images B-F show contours of $\xi_{csm} = 0.85$ plotted on top of the T2* weighted MR image in this region for different slices.

Tissue Type	$\mathfrak{Re}\{\mu\}$ (kPa)	ξ_d	ξ_{csm}
Fatty (1,113 values)	1.9 ± 1.1	1.18 ± 0.88	0.38 ± 0.30
Fibroglandular (3,375 values)	6.0 ± 2.3	0.66 ± 0.54	0.41 ± 0.26
Difference (95% C.I.)	(4.01,4.21)	(0.47,0.58)	(0.042,0.0049)

Table 5.1 Values of reconstructed material properties for patient 3004S2. Regions of fatty and fibroglandular tissue were manually segmented from the T2* weighted MR magnitude image, and values are given as the mean ± standard deviation. The difference results represent a 95% confidence interval for the difference in the mean material property values between fatty and fibroglandular tissue.

tissue, using the T2* weighted MR image as shown in Fig. 5.8. The mean and standard deviation of the imaged material properties for each type of tissue are given in Table 5.1.

5.2 Elementally Distributed Reconstruction Results

Due to time constraints, extensive development and testing of the elemental basis approach has not been undertaken. Some preliminary results using a global (not subzone-based) reconstruction algorithm with no regularization techniques are presented below, demonstrating that the method works to some degree using simulated data, and small sections of real data from gelatine phantoms.

5.2.1 Using Simulated Data

Reconstructions on simulated data are given below, the reference case consisted of a 1331 node, 125 element, 100mm cube with a 40Hz compressional excitation of the bottom face. All other faces were free surfaces. Three separate cubic inclusions were defined, an increased real shear modulus inclusion with constant damping ratio, one with reduced imaginary density and another with increased imaginary shear modulus. Background values were $\mu = 7000 + 140i$, $\rho = 1000 - 20i$ and $K = 10^8$. Gauss-Newton (GN) reconstructions are shown in Figure 5.13 for noise free data, as well as for data corrupted by 5% gaussian noise.

5.2.2 Using Real Data

Real Data reconstructions using a 1331 node subsection of MR-detected data from a gelatine phantom are given below. Figure 5.14 shows GN and CG real shear modulus reconstructions, for both a dynamic and fixed quadratic elemental basis.

A comparison of the measured and reconstructed motions for the dynamic basis GN reconstruction from Figure 5.14 is given in Figure 5.15.

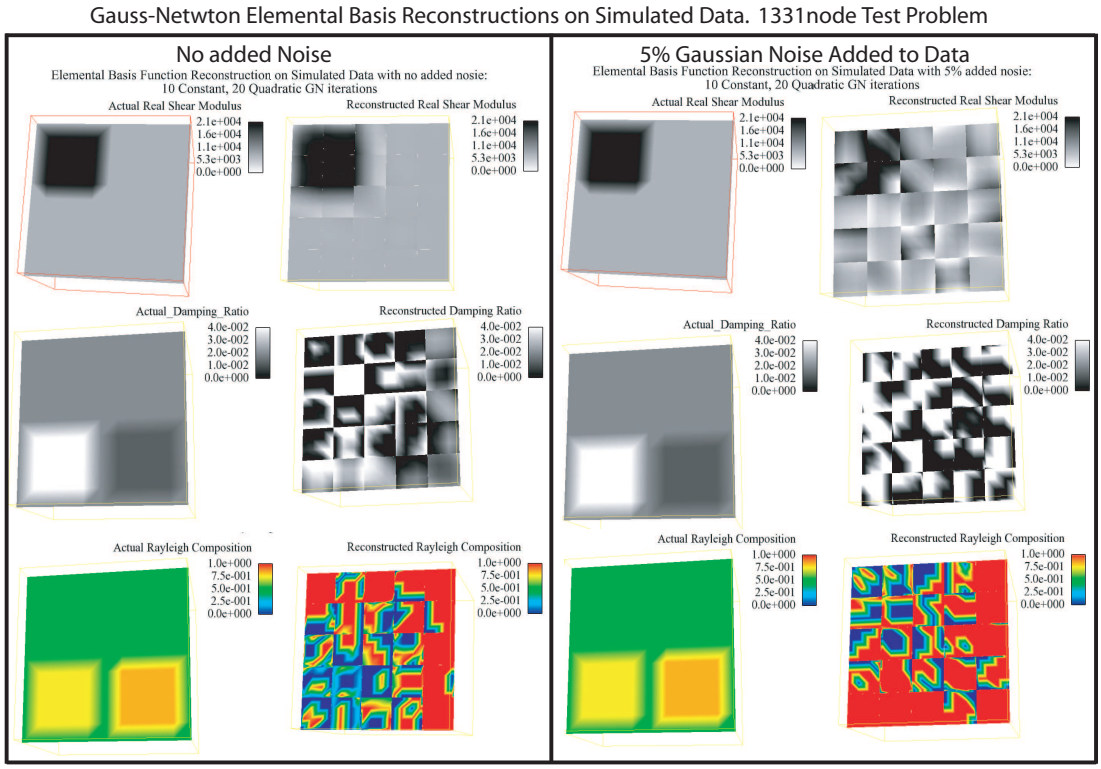

Figure 5.13 Gauss-Newton elemental basis reconstructions using simulated data. Real shear modulus, damping ratio, and Rayleigh composition (ξ_{csm}, Eq. 2.21) distributions are given, results with no noise added to the simulated motion data are on the left, and results with 5% added gaussian noise on the right.

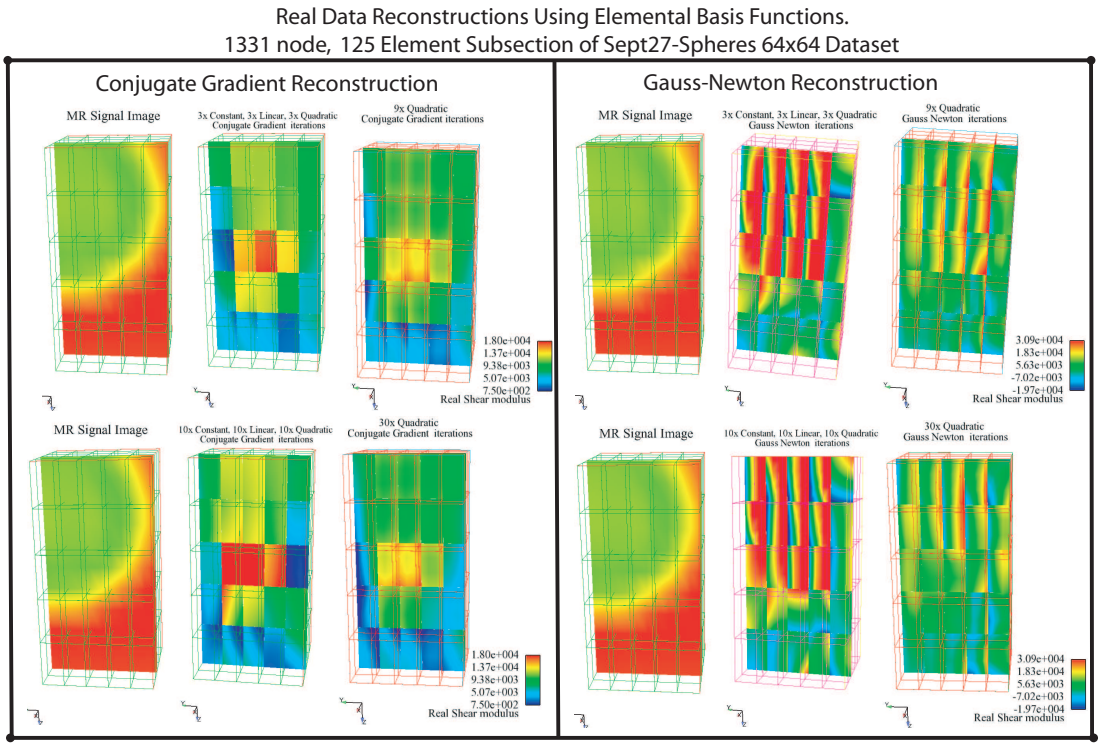

Figure 5.14 Real shear modulus elemental basis reconstructions on a 1331 node subsection of an MRI dataset. The green portion of the MR-signal image corresponds to an increased stiffness region. CG and GN results are given, with dynamic and fixed quadratic basis.

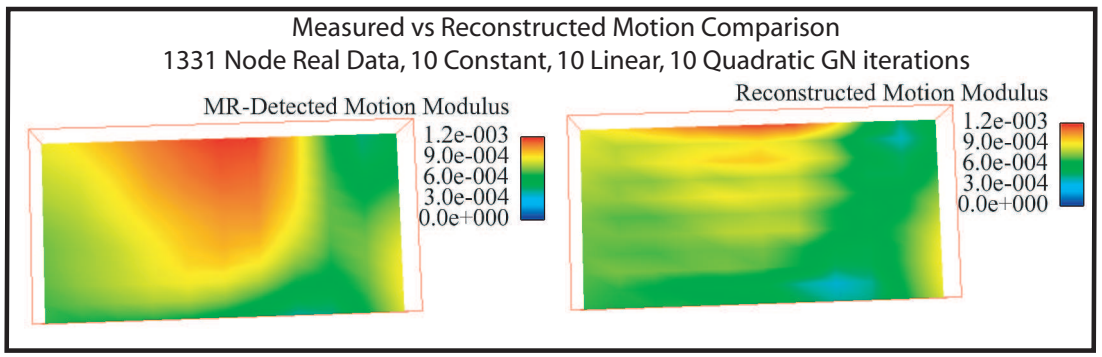

Figure 5.15 Elemental basis reconstructed motion comparison. The images show the modulus of the complex-valued motion amplitude, measured on the left and reconstructed values on the right.

In addition, a GN reconstruction with constant basis functions using a larger 9621 node subsection of MR-detected data is given in Figure 5.16.

5.3 Discussion of Distributed Reconstructions

5.3.1 Gelatine Phantom Reconstructions

Real shear modulus reconstructions of gelatine phantoms shown in Figures 5.3 and 5.6 demonstrate the algorithm does a good job of reconstructing a stiffer inclusion using MR-detected motion data. Some small artefacts were present on the boundary (most likely attributable to boundary noise), however the images showed a reasonably homogeneous distribution in regions of the same material. The resolution of the point of the cone indicates a good ability to reconstruct small-scale stiffer areas. Independently measured values of the shear modulus of each type of material are not available to compare numerical values to, but reconstructed values fall within the range quoted by the group which made the phantoms [45]. Gelatine is regarded as a good tissue mimicking material, therefore these results give a good indication that the algorithm will work using *in-vivo* data.

Damping parameter reconstructions for these gelatine phantoms had mixed success. Figure 5.4 shows the structure of the inclusion is evident in both the damping ratio and Rayleigh composition images, although significant variation is present in some areas of supposedly constant material properties. It should be noted that this variation is most severe in areas of generally low damping ratio, where Figure 4.2 predicts the Rayleigh combination may be difficult to determine. Figure 5.7 shows very little indication of the structure of the phantom in the damping parameter images. These phantoms are not designed to have different levels of damping inside and outside of the inclusion, and have much lower damping levels than is expected in tissue. A phantom with damping contrast and higher overall levels of damping may produce better results.

Figure 5.1 provides a verification of the artefact resulting from using the wrong damping model predicted in section 5.1.1. This artefact is related to the ratio of the motions and their second derivatives, and a clear similarity is evident between the reconstructed damping ratio distribution and the reference motions. There has been no investigation into the rayleigh damping characteristics of tissue, these results indicate that using the common one parameter viscoelastic damping models could introduce artefacts in the reconstructed damping parameter distribution if the true damping behavior of tissue is better described by a two parameter Rayleigh model.

If the Rayleigh damping model provides a better match for the damping behavior of a real material than a viscoelastic model, it may allow better reconstructions of other material properties, such as real shear modulus, due to decreased model-data

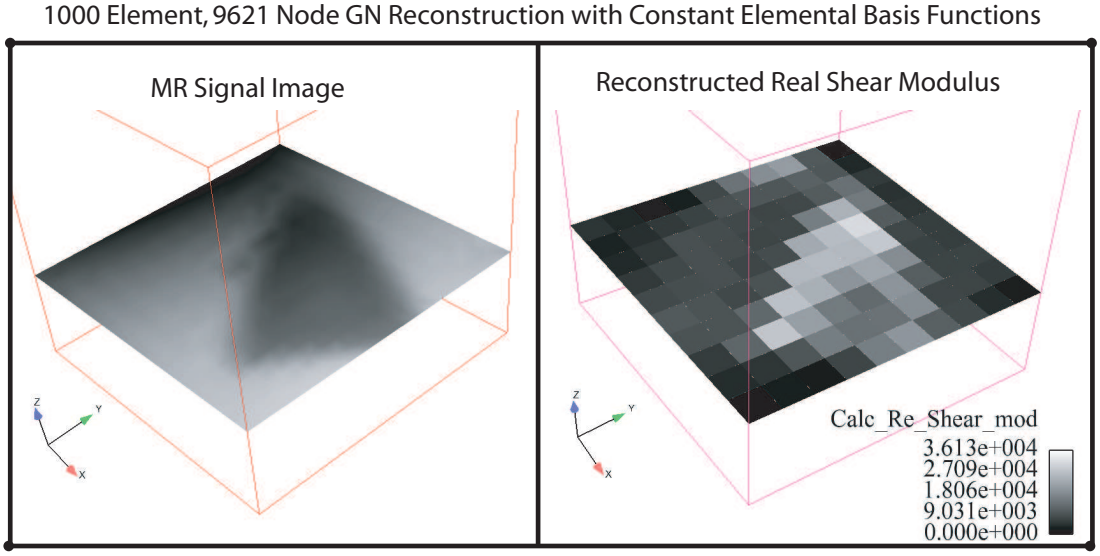

Figure 5.16 Fixed constant elemental basis GN reconstruction on a larger 9621 node subset of an MRI dataset. The dark triangular shape in the MR signal image corresponds to the position of a conical increased stiffness inclusion.

mismatch. This means a Rayleigh damped material model may still be of value even if the Rayleigh composition proves difficult to image, or of limited clinical value.

The algorithm works by minimizing the difference between the measured motions and those generated by the model. Figure 5.5 shows how well this is achieved, there is a very obvious similarity between the two displacement images.

5.3.2 *In-vivo* Reconstructions

Reconstructed Real shear modulus results in Figs. 5.9 and 5.10 show very good correlation with the anatomical structure shown in the MR image, with regions of fibroglandular tissue exhibiting a higher stiffness than regions of fat. Images A and B in Fig. 5.11 show a value of 2.5kPa provides a reasonable differentiation of the two tissue types.

Damping ratio images in Figs. 5.9 and 5.10 also show a good correspondence with anatomical structure, with fibroglandular tissue displaying generally lower damping levels than fat. The damping ratio image highlights slightly different anatomical features compared with the real shear modulus image, although the differentiation between the two tissue types remains clear.

The connection between the Rayleigh damping composition and anatomical structure is less obvious, but some correlation is evident. The differentiation between fatty and fibroglandular tissue seen in the real shear modulus and damping ratio images is not apparent, however the structure shown by Rayleigh composition images appears to be at a smaller scale. There is no evidence to say that the T2* MR magnitude values will be in any way related to the Rayleigh composition, but the MR image does provide a good differentiation between types of tissue. Figure 5.12 shows a close-up view of a region across a number of slices. The slice separation is 2.2mm, therefore the total distance spanned by the 5 slices is less than 9mm. This scale means the bright area at the bottom of the images is likely to correspond to a single anatomical structure. The contour of $\xi_{csm} = 0.85$ shows this area has damping which is dominated by complex shear modulus effects, the change in shape of the region across the slices in the MR image is matched by the change in shape of the ξ_{csm} contours.

Material property images at the boundary of the data, shown in the images marked 'A' in Fig 5.9, were of a similar quality to internal regions, demonstrating the algorithms ability to correctly identify material properties close to the boundaries. This can be especially important in smaller datasets, where the boundaries represent a significant portion of reconstructed values.

The different anatomic structures imaged by real shear modulus, damping ratio and Rayleigh composition show promise for accurate *in-vivo* determination of different tissue types, and the possibility of diagnosing different types of cancer based on

these reconstructed values. These promising initial results warrant a more detailed investigation of the Rayleigh model.

The average material property values estimated by manual segmentation of the MR image into regions of fibroglandular and fatty tissue, shown in Table 5.1, exhibit a definite difference in real shear modulus and damping ratio between the two tissue types, and no significant difference in Rayleigh composition.

Published results for the real shear modulus of fatty and fibroglandular tissue vary, values ranging from 0.16 to 16kPa have been reported [9, 10, 46, 47]. Most values for fibroglandular tissue show a higher stiffness than fatty tissue, as found in this study, although the most recent and comprehensive results from Samani et. al. [16] indicate fatty and fibroglandular tissues have a similar shear modulus of about 1.1kPa. This disagreement is likely to be due to different levels of precompression applied in each test. Krouskop et. al. [47] found variations in stiffness of breast tissue under different levels of precompression, which is attributable to nonlinear material behavior. Another source of discrepancy may be the frequency the measurements are taken at, values measured using quasi-static approaches such as [16] are expected to differ from higher frequency approaches such as time-harmonic MRE, because of the frequency dependence of the shear modulus. The non-linear characteristics and frequency dependence are likely to be different for different tissue types, therefore differing shear moduli under different conditions are possible.

Measurements of damping related properties of tissue in the literature are scarce, Sinkus et. al. use MRE to reconstruct the distribution of shear modulus and shear viscosity. Values given in [18] correspond to damping ratios for healthy tissue of of 0.13, which is lower than the values of 0.6-1.2 reconstructed using the Rayleigh model. These results are taken at a frequency of 65Hz, which is lower than the 85Hz used in the Rayleigh damping reconstructions. Both real and imaginary shear modulus in living tissue have been shown to follow a power law frequency dependence [48, 49, 50], experimental results indicate higher damping ratios at higher frequencies are expected. Results at 85Hz are reported in [51]; although results for normal breast tissue are not given, values equivalent to damping ratios of between 0.25 and 1.1 are given for a variety of benign and malignant lesions. A damping ratio above 1 would mean the transient response of tissue would decay without oscillation, and a value of 0.7 would predict 1-2 oscillations before the motion becomes imperceptibly small, compared with 4-5 oscillations for a damping ratio of 0.13. A simple prod of any fatty region of the body indicate any of these values are reasonable. There are currently no independent measurements of Rayleigh composition available for comparison, results given here indicate such measurements would need to be made on small scale tissue structures to be of use for verification purposes.

5.3.3 Elemental Basis Reconstructions

The real shear modulus reconstruction results in Figures 5.13 and 5.14 showed some promise for elemental basis reconstructions, as the correct distribution was characterized to some degree using both simulated and real data, however the significant variation within regions of supposedly constant material properties in the presence of measurement noise is the major obstacle to overcome at this stage. Damping parameter reconstructions were poor in all cases, most likely due to no bounds being applied to the values, allowing physically unrealistic negative damping ratios to occur. A subzone implementation which includes material property bounds may improve damping parameter reconstructions. The continuity requirement of the nodal basis acts as a kind of regularization, so by removing this requirement other forms of regularization will likely need to be added. This initial implementation uses no regularization techniques, the most obvious one to try would be total variation minimization. This technique would lend itself well to the discontinuous elemental basis functions, and would hopefully suppress some of the extreme variation across the elements.

The significant variation of the material properties across the elements is likely to be due to a lower sensitivity of the linear basis terms. The linear terms give a linear variation across the element, without any change in average material property value. A region with approximately constant material properties may be well represented by a region with a linear variation, where the average material property value is equal to the constant case, with only local displacement differences. This may cause the algorithm to use variation across the elements to fit the local effects of noisy displacement data. This idea was tested through a simple sensitivity analysis, where a 10% overall change in real shear modulus across an element was achieved using the constant term, and a linear term. The constant change resulted in an overall motion difference of 0.21%, whereas the linear change resulted in a 0.09% change.

The reconstructed motion image in figure 5.15 has a similar pattern to the measured motions, but with noticeable striations consistent with element edges. These are a result of the large variation in reconstructed stiffness across the elements in this area.

The comparison of the dynamic basis approach with a fixed quadratic basis in Figure 5.14 shows similar results, which is not surprising because they are essentially solving the same problem. The actual value of a dynamic basis approach may lie in its efficiency. The reduced order basis Gauss-Newton iterations are considerably faster and use a lot less memory than the quadratic basis iterations, for example a 1GB complex Hessian matrix would correspond to 658 elements with μ, ρ and K constant over the element, compared with only 94 if μ and ρ have a quadratic variation. Alternatively, a 100 element Hessian will be only 23MB for the constant case, compared with 1.12GB for quadratic μ and ρ. This could be useful for subzone reconstructions, as early iterations could be processed rapidly using constant basis functions with either a lower

number of larger subzones, or faster processing of smaller ones to get close to the correct properties, then a small number of slower quadratic basis iterations could be used at the end to characterize the variation. Figure 5.16 gives an indication of the possibilities, a problem of this size is not possible to solve using the nodal basis functions or quadratic elemental basis with the GN method, but is easily handled with the constant elemental basis, and gives a good initial estimate of the real shear modulus distribution.

Chapter 6

Conclusions and Future Work

Real shear modulus reconstructions of gelatine phantoms performed well, a good ability to accurately reconstruct the shape of an increased stiffness inclusion was demonstrated. Simulation studies using globally defined Rayleigh damping parameters, as well as some initial promising images from gelatine phantoms indicate it is possible to distinguish regions of differing Rayleigh damping parameters, and that artefacts occur in the reconstructed damping parameter images if a one parameter damping model is used to fit a material better described by a two parameter Rayleigh model.

Initial *in-vivo* results were promising, areas of fibroglandular tissue were found to have a higher real shear modulus and lower damping ratio than the surrounding fatty tissue. Rayleigh damping composition images were also correlated to anatomical structure, although at a smaller scale than the other parameters.

The nodal basis reconstruction code is at a point where a detailed investigation into how reliably useful Rayleigh damping composition images can be produced. Obtaining motion data from a phantom with damping contrast will be the first step down this path. If the Rayleigh parameters are able to be imaged reliably, a clinical investigation into whether or not these additional material properties are able to used to assist in diagnosis of different types of cancer should be undertaken.

One approach to improve the reconstruction of the Rayleigh parameters would be to allow each type of material property to be given a different regularization weight, which would may reduce variation in the material properties with a smaller effect on the motion, such as imaginary density. If the actual combination of Rayleigh parameters proves too difficult to image reliably, a comparison of real shear modulus and damping ratio results should be made between a Rayleigh model and the standard viscoelastic damping model to determine whether reconstructing an imaginary density is worthwhile.

The elemental basis approach showed some initial promise, as well as some significant issues with variation across the elements. In order to make a informed judgement

on their suitability, a subzone implementation with regularization techniques and material property bounds needs to be experimented with.

Appendix A

Incompressible Elasticity Theory

The equations relating axial stress and strain for a compressible, linear elastic, isotropic material in three dimensions can be written as:

$$\begin{aligned} \epsilon_x &= \frac{1}{E}(\sigma_x - \nu(\sigma_y + \sigma_z)) \\ \epsilon_y &= \frac{1}{E}(\sigma_y - \nu(\sigma_x + \sigma_z)) \\ \epsilon_z &= \frac{1}{E}(\sigma_z - \nu(\sigma_x + \sigma_y)), \end{aligned} \tag{A.1}$$

where σ_x, σ_y and σ_z are the stresses in each of the coordinate directions, ϵ_x, ϵ_y and ϵ_z are the corresponding strains, E is the elastic modulus and ν is the Poisson's ratio. Rearranging Eq. A.1 to give stresses in terms of strains gives

$$\begin{aligned} \sigma_x &= 2\mu\epsilon_x + \lambda(\epsilon_x + \epsilon_y + \epsilon_z) \\ \sigma_y &= 2\mu\epsilon_y + \lambda(\epsilon_x + \epsilon_y + \epsilon_z) \\ \sigma_z &= 2\mu\epsilon_z + \lambda(\epsilon_x + \epsilon_y + \epsilon_z), \end{aligned} \tag{A.2}$$

with Lamé's first parameter given by $\lambda = \frac{\nu E}{(1+\nu)(1-2\nu)}$, and Lamé's second parameter, commonly known as the shear modulus, given by $\mu = \frac{E}{2(1+\nu)}$.

The definition of shear modulus gives the shear stresses, τ_{ij} as:

$$\begin{aligned} \tau_{xy} &= \mu\gamma_{xy} \\ \tau_{xz} &= \mu\gamma_{xz} \\ \tau_{yz} &= \mu\gamma_{yz}, \end{aligned} \tag{A.3}$$

where γij are the corresponding shear strains.

The volumetric strain, e, of an elastic solid is given by:

$$e = \frac{\Delta V}{V} = \epsilon_x + \epsilon_y + \epsilon_z, \tag{A.4}$$

where ΔV is the change in total volume, V for a given strain state. The definitions of axial strains, $\epsilon_x = \frac{\partial u}{\partial x}$, $\epsilon_y = \frac{\partial u}{\partial y}$ and $\epsilon_z = \frac{\partial u}{\partial z}$, mean the volumetric strain is also the divergence of the vector displacement field $\mathbf{u}$,

$$e = \nabla \cdot \mathbf{u}. \tag{A.5}$$

As $\nu \to 0.5$, Eqs. A.1 and A.4 show that $e \to 0$, therefore the material becomes incompressible. Examining Eq. A.2, it is seen that the stresses are singular in this case, because $\lambda \to \infty$ as $\nu \to 0.5$.

To deal with this singularity, the overall stress is broken down into two components, the dilatational stress $\bar{\sigma}$, and the deviatoric stresses σ'_x, σ'_y and σ'_z, so that

$$\begin{aligned} \sigma_x &= \sigma'_x + \bar{\sigma} \\ \sigma_y &= \sigma'_y + \bar{\sigma} \\ \sigma_z &= \sigma'_z + \bar{\sigma}. \end{aligned} \tag{A.6}$$

The dilatational stress is given by

$$\bar{\sigma} = \frac{1}{3}(\sigma_x + \sigma_y + \sigma_z) = \frac{1}{3}(2\mu + 3\lambda)e = Ke, \tag{A.7}$$

where the bulk modulus, K is given by $K = \frac{E}{3(1-2\nu)} = \frac{2\mu+3\lambda}{3}$. The dilatational stress is often given as a scalar pressure, P.

$$\bar{\sigma} = Ke = -P. \tag{A.8}$$

The deviatoric stresses σ'_x, σ'_y and σ'_z are the stresses leftover once dilatational effects have been accounted for, so are given by:

$$\begin{aligned} \sigma'_x &= \sigma_x - \bar{\sigma} \\ \sigma'_y &= \sigma_y - \bar{\sigma} \\ \sigma'_z &= \sigma_z - \bar{\sigma}, \end{aligned} \tag{A.9}$$

and

$$\sigma_x + \sigma_y + \sigma_z = 3\bar{\sigma} + \sigma'_x + \sigma'_y + \sigma'_z = 3\frac{1}{3}(\sigma_x + \sigma_y + \sigma_z) + \sigma'_x + \sigma'_y + \sigma'_z. \tag{A.10}$$

This implies

$$\sigma'_x + \sigma'_y + \sigma'_z = 0. \tag{A.11}$$

The deviatoric stresses can be shown to produce no net volume change by considering the deviatoric strains, ϵ'_x, ϵ'_y and ϵ'_z.

$$\begin{aligned}\epsilon'_x &= \frac{1}{E}(\sigma'_x - \nu(\sigma'_y + \sigma'_z)) \\ \epsilon'_y &= \frac{1}{E}(\sigma'_y - \nu(\sigma'_x + \sigma'_z)) \\ \epsilon'_z &= \frac{1}{E}(\sigma'_z - \nu(\sigma'_x + \sigma'_y)).\end{aligned} \tag{A.12}$$

The volumetric strain produced by the deviatoric stresses is given by:

$$e' = \epsilon'_x + \epsilon'_y + \epsilon'_z = \frac{1-2\nu}{E}(\sigma'_x + \sigma'_y + \sigma'_z) = 0. \tag{A.13}$$

The deviatoric stresses are therefore the components of the overall axial stress that produce changes in shape without any changes in volume.

Using Eqs. A.2, A.7 and A.9, the deviatoric stresses can be expressed as:

$$\begin{aligned}\sigma'_x &= 2\mu\epsilon_x + \lambda e - Ke \\ \sigma'_y &= 2\mu\epsilon_y + \lambda e - Ke \\ \sigma'_z &= 2\mu\epsilon_z + \lambda e - Ke.\end{aligned} \tag{A.14}$$

An incompressible material will have zero volumetric strain, e, therefore the deviatoric stresses in this case are given by:

$$\begin{aligned}\sigma'_x &= 2\mu\epsilon_x \\ \sigma'_y &= 2\mu\epsilon_y \\ \sigma'_z &= 2\mu\epsilon_z.\end{aligned} \tag{A.15}$$

The isotropic stress tensor, $\vec{\vec{\sigma}}$, for an incompressible material is therefore given by:

$$\vec{\vec{\sigma}} = \begin{pmatrix} \sigma_x & \tau_{xy} & \tau_{xz} \\ \tau_{yx} & \sigma_y & \tau_{yz} \\ \tau_{zx} & \tau_{zy} & \sigma_z \end{pmatrix}, \tag{A.16}$$

where Eqs. A.6, A.8 and A.15 give the axial stresses as:

$$\begin{aligned}\sigma_x &= 2\mu\epsilon_x - P \\ \sigma_y &= 2\mu\epsilon_y - P \\ \sigma_z &= 2\mu\epsilon_z - P.\end{aligned} \tag{A.17}$$

Equation A.3 relating shear stresses and strains remains unchanged. Equilibrium conditions for the material occur when the internal stresses equal the sum of the inertial

and external forces,

$$\nabla \cdot \vec{\vec{\sigma}} = \rho \frac{d^2\mathbf{u}}{dt^2} + \mathbf{f}, \tag{A.18}$$

where ρ is the density of the material and $\mathbf{f}$ represents the external forces. This divergence operation can be expanded in x, y, z coordinates as

$$\nabla \cdot \vec{\vec{\sigma}} = \nabla \cdot (\vec{\sigma_x}\hat{\mathbf{i}} + \vec{\sigma_y}\hat{\mathbf{j}} + \vec{\sigma_z}\hat{\mathbf{k}}), \tag{A.19}$$

where

$$\begin{aligned} \vec{\sigma_x} &= \sigma_x\hat{i} + \tau_{xy}\hat{j} + \tau_{xz}\hat{k} \\ \vec{\sigma_y} &= \tau_{yx}\hat{i} + \sigma_y\hat{j} + \tau_{yz}\hat{k} \\ \vec{\sigma_y} &= \tau_{zx}\hat{i} + \tau_{zy}\hat{j} + \sigma_z, \hat{k}, \end{aligned} \tag{A.20}$$

and $\hat{i}, \hat{j}$ and $\hat{k}$ are unit vectors in the x, y and z directions respectively. The definitions of axial and shear strains are given by

$$\begin{aligned} \epsilon_x &= \frac{\partial u}{\partial x} \\ \epsilon_y &= \frac{\partial v}{\partial y} \\ \epsilon_z &= \frac{\partial w}{\partial z} \end{aligned} \tag{A.21a}$$

$$\begin{aligned} \gamma_{xy} = \gamma_{yx} &= \frac{\partial u}{\partial y} + \frac{\partial v}{\partial x} \\ \gamma_{xz} = \gamma_{zx} &= \frac{\partial u}{\partial z} + \frac{\partial w}{\partial x} \\ \gamma_{yz} = \gamma_{zy} &= \frac{\partial v}{\partial z} + \frac{\partial w}{\partial y}, \end{aligned} \tag{A.21b}$$

where u, v and w are the displacement in the x, y and z coordinate directions respectively. Combining Eqs. A.17, A.3, A.19 and A.20 and A.21 gives:

$$\begin{aligned} 2\frac{\partial}{\partial x}\,\mu\frac{\partial u}{\partial x} + \frac{\partial}{\partial y}\,\mu(\frac{\partial u}{\partial y} + \frac{\partial v}{\partial x}) + \frac{\partial}{\partial z}\,\mu(\frac{\partial u}{\partial z} + \frac{\partial w}{\partial x}) - \frac{\partial P}{\partial x} - \rho\frac{\partial^2 u}{\partial t^2} &= f_x \\ \frac{\partial}{\partial x}\,\mu(\frac{\partial v}{\partial x} + \frac{\partial u}{\partial y}) + 2\frac{\partial}{\partial y}\,\mu\frac{\partial v}{\partial y} + \frac{\partial}{\partial z}\,\mu(\frac{\partial v}{\partial z} + \frac{\partial w}{\partial y}) - \frac{\partial P}{\partial y} - \rho\frac{\partial^2 v}{\partial t^2} &= f_y \\ \frac{\partial}{\partial x}\,\mu(\frac{\partial w}{\partial x} + \frac{\partial u}{\partial z}) + \frac{\partial}{\partial y}\,\mu(\frac{\partial w}{\partial y} + \frac{\partial v}{\partial z}) + 2\frac{\partial}{\partial z}\,\mu\frac{\partial w}{\partial z} - \frac{\partial P}{\partial z} - \rho\frac{\partial^2 w}{\partial t^2} &= f_z. \end{aligned} \tag{A.22}$$

This can be written in the form of a partial differential equation (PDE) as:

$$\nabla \cdot \mu\nabla\tilde{\mathbf{u}} + \nabla(\mu\nabla \cdot \mathbf{u} - P) - \rho\frac{d^2\mathbf{u}}{dt^2} = \mathbf{f}. \tag{A.23}$$

These equations, together with the continuity equation

$$K\frac{\partial u}{\partial x} + K\frac{\partial v}{\partial y} + K\frac{\partial w}{\partial z} = P, \tag{A.24}$$

describe the behavior of a material with a Poisson's ratio of 0.499999 and higher. Standard compressible elasticity equations become highly sensitive for Poisson's ratio's of above about 0.495 [52]. Equation A.24 means that the term $\nabla \cdot \mathbf{u}$ in Eq. A.23 $\rightarrow 0$ as $K \rightarrow \infty$. This term is left in the PDE to ensure the boundary integrals in the finite element weak form represent elastic stresses.

Appendix B

Finite Element Formulation

This section details the methods used to transform the incompressible elasticity equations developed in Appendix A into a finite element (FE) form. Material property variation is supported by nodal basis functions, a similar formulation is used for elemental basis support.

Figure B.1 shows the 27 node hexahedral elements used in the FE formulation, with the local (ξ, η, ζ) coordinate system. Tri-quadratic displacement and tri-linear pressure support are used, as elements with displacement support one order above that of pressure give good convergence behavior for incompressible materials [53]. The node numbering scheme is shown in the figure, and given by the nodal coordinates:

$$
\begin{array}{lll}
X_1 = (-1,-1,-1\,) & X_{10} = (-1,-1,\ 1\,) & X_{19} = (-1,-1,\ 0\,) \\
X_2 = (\ \ 1,-1,-1\,) & X_{11} = (\ \ 1,-1,\ 1\,) & X_{20} = (\ \ 1,-1,\ 0\,) \\
X_3 = (\ \ 1,\ \ 1,-1\,) & X_{12} = (\ \ 1,\ \ 1,\ 1\,) & X_{21} = (\ \ 1,\ \ 1,\ 0\,) \\
X_4 = (-1,\ \ 1,-1\,) & X_{13} = (-1,\ \ 1,\ 1\,) & X_{22} = (-1,\ \ 1,\ 0\,) \\
X_5 = (\ \ 0,-1,-1\,) & X_{14} = (\ \ 0,-1,\ 1\,) & X_{23} = (\ \ 0,-1,\ 0\,) \\
X_6 = (\ \ 1,\ \ 0,-1\,) & X_{15} = (\ \ 1,\ \ 0,\ 1\,) & X_{24} = (\ \ 1,\ \ 0,\ 0\,) \\
X_7 = (\ \ 0,\ \ 1,-1\,) & X_{16} = (\ \ 0,\ \ 1,\ 1\,) & X_{25} = (\ \ 0,\ \ 1,\ 0\,) \\
X_8 = (-1,\ \ 0,-1\,) & X_{17} = (-1,\ \ 0,\ 1\,) & X_{26} = (-1,\ \ 0,\ 0\,) \\
X_9 = (\ \ 0,\ \ 0,-1\,) & X_{18} = (\ \ 0,\ \ 0,\ 1\,) & X_{27} = (\ \ 0,\ \ 0,\ 0\,).
\end{array}
\tag{B.1}
$$

Quadratic elements perform well for geometries with curved boundaries and displacement patterns, and hexahedral elements were chosen as the regular pattern of nodes is compatible with the voxel-based MRI motion data. Support of a function, $g(\xi, \eta, \zeta)$ on a set of basis functions is defined as

$$
g(\xi, \eta, \zeta) \approx \sum_{i=1}^{N} (g_i \phi_i(\xi, \eta, \zeta)), \tag{B.2}
$$

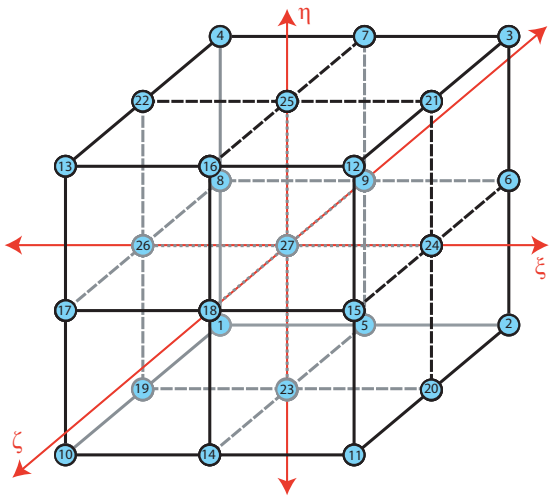

Figure B.1 27 node Hexahedral element with node numbering scheme and local (ξ, η, ζ) coordinate system shown. Element extents are {-1,1} in the ξ, η and ζ directions.

where g_i is the function value at the N nodes of the element, and ϕ_i are the basis functions, given by:

$$\begin{aligned}
\phi_{1+9i}(\xi,\eta,\zeta) &= \theta_1(\xi)\theta_1(\eta)\theta_{i+1}(\zeta)\\
\phi_{2+9i}(\xi,\eta,\zeta) &= \theta_2(\xi)\theta_1(\eta)\theta_{i+1}(\zeta)\\
\phi_{3+9i}(\xi,\eta,\zeta) &= \theta_2(\xi)\theta_2(\eta)\theta_{i+1}(\zeta)\\
\phi_{4+9i}(\xi,\eta,\zeta) &= \theta_1(\xi)\theta_2(\eta)\theta_{i+1}(\zeta)\\
\phi_{5+9i}(\xi,\eta,\zeta) &= \theta_3(\xi)\theta_1(\eta)\theta_{i+1}(\zeta)\\
\phi_{6+9i}(\xi,\eta,\zeta) &= \theta_2(\xi)\theta_3(\eta)\theta_{i+1}(\zeta)\\
\phi_{7+9i}(\xi,\eta,\zeta) &= \theta_3(\xi)\theta_2(\eta)\theta_{i+1}(\zeta)\\
\phi_{8+9i}(\xi,\eta,\zeta) &= \theta_1(\xi)\theta_3(\eta)\theta_{i+1}(\zeta)\\
\phi_{9+9i}(\xi,\eta,\zeta) &= \theta_3(\xi)\theta_3(\eta)\theta_{i+1}(\zeta),
\end{aligned} \tag{B.3}$$

where $i = 0, 1, 2$, and

$$\begin{aligned}
\theta_1(s) &= \frac{s}{2}(s-1)\\
\theta_2(s) &= \frac{s}{2}(s+1)\\
\theta_3(s) &= (1+s)(1-s).
\end{aligned} \tag{B.4}$$

Each basis function, ϕ_i, has a value of 1 at node i, and zero at all other nodes. They are constructed so that for any point ($[\bar{\xi}, \bar{\eta}, \bar{\zeta}]$) within the element,

$$\sum_{i=1}^{27} \phi_i(\bar{\xi}, \bar{\eta}, \bar{\zeta}) = 1 \tag{B.5}$$

Both the x, y and z coordinates, as well as the u, v and w displacements are supported on these basis functions, so this type of element is known as 'isoparametric', because both the displacements and coordinates are described by the same parametric variation. This ensures the element possesses rigid body modes, i.e. the element can displace as a whole with no internal stresses generated. If $\boldsymbol{\phi} = [\phi_1\ \phi_2 \ldots \phi_{27}]$, the displacements, u, v, w, and coordinates, x, y, z, are given by:

$$\begin{Bmatrix} \mathbf{u} \\ \mathbf{v} \\ \mathbf{w} \end{Bmatrix} = \begin{bmatrix} \boldsymbol{\phi} & \mathbf{0} & \mathbf{0} \\ \mathbf{0} & \boldsymbol{\phi} & \mathbf{0} \\ \mathbf{0} & \mathbf{0} & \boldsymbol{\phi} \end{bmatrix} \begin{Bmatrix} \mathbf{U}_i \\ \mathbf{V}_i \\ \mathbf{W}_i \end{Bmatrix} \tag{B.6a}$$

$$\begin{Bmatrix} \mathbf{x} \\ \mathbf{y} \\ \mathbf{z} \end{Bmatrix} = \begin{bmatrix} \boldsymbol{\phi} & \mathbf{0} & \mathbf{0} \\ \mathbf{0} & \boldsymbol{\phi} & \mathbf{0} \\ \mathbf{0} & \mathbf{0} & \boldsymbol{\phi} \end{bmatrix} \begin{Bmatrix} \mathbf{X}_i \\ \mathbf{Y}_i \\ \mathbf{Z}_i \end{Bmatrix}, \tag{B.6b}$$

where $\mathbf{U}_i$, $\mathbf{V}_i$ and $\mathbf{W}_i$ are vectors containing the appropriate nodal displacement at all 27 nodes, and similarly $\mathbf{X}_i$, $\mathbf{Y}_i$, and $\mathbf{Z}_i$ contain the appropriate nodal coordinates. The trilinear pressure function, $P(x, y, z)$ is supported over the element by a constant P, $\frac{\partial P}{\partial x}$, $\frac{\partial P}{\partial y}$ and $\frac{\partial P}{\partial z}$. This basis function is denoted by ψ, so that the pressure distribution is given by:

$$P(\xi, \eta, \zeta) = \sum_{i=1}^{4} [\mathbf{p}_i \psi_i(\xi, \eta, \zeta)], \tag{B.7}$$

where $\mathbf{p}_i$ is a vector which contains the constant pressure and its derivatives for a given element, and the basis functions ψ_i are given by

$$\begin{aligned} \psi_1 &= 1 \\ \psi_2 &= \xi \\ \psi_3 &= \eta \\ \psi_4 &= \zeta. \end{aligned} \tag{B.8}$$

An arbitrarily shaped element in the (x, y, z) coordinate system is mapped onto the reference element shown in Fig. B.1 ((ξ, η, ζ) coordinate system) by the transformation

$$\mathbf{x} = F_e(\boldsymbol{\xi}), \tag{B.9}$$

where $\mathbf{x}$ represents a coordinate in the x, y, z coordinate system, $\boldsymbol{\xi}$ represents a coordinate in the ξ, η, ζ coordinate system, and F_e is given by

$$F_e = \sum_{i=1}^{27} (x_i \phi_i(\boldsymbol{\xi})). \tag{B.10}$$

The derivatives of the basis functions between the two coordinate systems are related by:

$$\begin{bmatrix} \frac{\partial \phi_i}{\partial \xi} \\ \frac{\partial \phi_i}{\partial \eta} \\ \frac{\partial \phi_i}{\partial \zeta} \end{bmatrix} = \begin{bmatrix} \frac{\partial x}{\partial \xi} & \frac{\partial y}{\partial \xi} & \frac{\partial z}{\partial \xi} \\ \frac{\partial x}{\partial \eta} & \frac{\partial y}{\partial \eta} & \frac{\partial z}{\partial \eta} \\ \frac{\partial x}{\partial \zeta} & \frac{\partial y}{\partial \zeta} & \frac{\partial z}{\partial \zeta} \end{bmatrix} \begin{bmatrix} \frac{\partial \phi_i}{\partial x} \\ \frac{\partial \phi_i}{\partial y} \\ \frac{\partial \phi_i}{\partial z} \end{bmatrix} = [\, \mathbf{J}_c \,] \begin{bmatrix} \frac{\partial \phi_i}{\partial x} \\ \frac{\partial \phi_i}{\partial y} \\ \frac{\partial \phi_i}{\partial z} \end{bmatrix} \tag{B.11}$$

Using Eq. B.6b, the coordinate jacobian, $\mathbf{J}_c$, can be calculated by

$$[\, \mathbf{J}_c \,] = \begin{bmatrix} \frac{\partial \phi}{\partial \xi} \\ \frac{\partial \phi}{\partial \eta} \\ \frac{\partial \phi}{\partial \zeta} \end{bmatrix} \begin{bmatrix} \mathbf{X}_i & \mathbf{Y}_i & \mathbf{Z}_i \end{bmatrix}. \tag{B.12}$$

Weighted Residual FEM Formulation

An equivalent weighted residual (WR) weak form of Equations A.23 and A.24 was used to develop the finite element model of the material. If $\mathscr{L}$ is the differential operator from the LHS of equation A.22, the residual, R for an approximation of the displacement $\hat{\mathbf{u}}$ is defined as:

$$R = \mathscr{L}(\hat{\mathbf{u}}) - \mathbf{f}, \tag{B.13}$$

where $\mathbf{f}$ represents the terms on the RHS of Eq. A.22. If $\hat{\mathbf{u}}$ exactly matches the true displacement field, $\mathbf{u}$, the residual will obviously be zero everywhere. If $\hat{\mathbf{u}}$ is an approximation to $\mathbf{u}$, this is not the case. If the residual is supposed to be zero everywhere, a weighted integral over the volume, Ω, should also be zero, i.e.

$$\iiint_{\Omega} W_i R \, \mathrm{d}\Omega, \tag{B.14}$$

for some weighting function W_i. This is the weighted residual statement, and is known as a weak formulation, as the PDE conditions are only required to be met in an average sense over the volume. If Eq. B.14 is required to hold for multiple weighting functions, $\hat{\mathbf{u}}$ will become a better approximation for $\mathbf{u}$. In the extreme case where the set of weighting functions encompasses all possible functions over the volume, $\hat{\mathbf{u}} = \mathbf{u}$.

The Galerkin weighted residual method uses each of the polynomial basis functions as weighting functions, giving the Galerkin weighted residual statement for the i'th

basis function as

$$\iiint_{\Omega} \phi_i R \, \mathrm{d}\Omega = 0, \tag{B.15}$$

where the integral is over the whole volume, Ω. Assuming no external forces, Eq. A.18 can be used to define the residual, R for an approximation to the true stress tensor, $\nabla \cdot \vec{\vec{\sigma}}$ and displacement, $\hat{\mathbf{u}}$.

$$R = \nabla \cdot \vec{\vec{\sigma}} - \rho \frac{\partial^2 \hat{\mathbf{u}}}{dt^2}. \tag{B.16}$$

Greens Theorem can be written as

$$\iiint_{\Omega} g \nabla \cdot \nabla h \, \mathrm{d}\Omega = - \iiint_{\Omega} \nabla g \cdot \nabla h \, \mathrm{d}\Omega + \oint_{\Gamma} g \nabla h \, \mathrm{d}S, \tag{B.17}$$

for functions g and h, and $\oint_{\Gamma}$ represents a surface integral evaluated over the boundary of the volume, Γ. Setting $\nabla h = \vec{\vec{\sigma}}$, and $g = \phi_i$ gives

$$\iiint_{\Omega} \phi_i \nabla \cdot \vec{\vec{\sigma}} dV = - \iiint_{\Omega} \nabla \phi_i \cdot \vec{\vec{\sigma}} dV + \oint_{\Gamma} \phi_i \vec{\vec{\sigma}} dS. \tag{B.18}$$

Applying the expanded stress tensor given in Eq. A.19 leads to

$$\iiint_{\Omega} \phi \nabla \cdot \vec{\vec{\sigma}} dV = - \iiint_{\Omega} \frac{\partial \phi}{\partial x} \cdot \vec{\sigma}_x dV + \frac{\partial \phi}{\partial y} \cdot \vec{\sigma}_y + \frac{\partial \phi}{\partial z} \cdot \vec{\sigma}_z dV + \oint_{\Gamma} \phi \vec{\vec{\sigma}} dS. \tag{B.19}$$

Applying Eq. B.19 to Eq. B.16, and using Eq. A.20, gives to three equations, one for each direction.

$$\begin{aligned}
\left\langle \frac{\partial \phi}{\partial x}\sigma_x + \frac{\partial \phi}{\partial y}\tau_{xy} + \frac{\partial \phi}{\partial z}\tau_{xz} \right\rangle &= \oint_{\Gamma} \phi(\mathbf{n}_x\sigma_x + \mathbf{n}_y\tau_{xy} + \mathbf{n}_z\tau_{xz}) dS_x - \left\langle \rho\phi \frac{\partial^2 u}{\partial t^2} \right\rangle \\
\left\langle \frac{\partial \phi}{\partial x}\tau_{xy} + \frac{\partial \phi}{\partial y}\sigma_y + \frac{\partial \phi}{\partial z}\tau_{yz} \right\rangle &= \oint_{\Gamma} \phi(\mathbf{n}_x\tau_{xy} + \mathbf{n}_y\sigma_y + \mathbf{n}_z\tau_{yz}) dS_y - \left\langle \rho\phi \frac{\partial^2 v}{\partial t^2} \right\rangle \\
\left\langle \frac{\partial \phi}{\partial x}\tau_{xz} + \frac{\partial \phi}{\partial y}\tau_{yz} + \frac{\partial \phi}{\partial z}\sigma_z \right\rangle &= \oint_{\Gamma} \phi(\mathbf{n}_x\tau_{xz} + \mathbf{n}_y\tau_{yz} + \mathbf{n}_z\sigma_z) dS_z - \left\langle \rho\phi \frac{\partial^2 w}{\partial t^2} \right\rangle.
\end{aligned} \tag{B.20}$$

Here, $\langle \dots \rangle$ is shorthand notation for $\iiint_{\Omega} \dots dV$, $\mathbf{n}_x, \mathbf{n}_y$ and $\mathbf{n}_z$ are unit normal vectors in the x, y and z directions respectively, and $\sigma_{\underline{i}}$ and $\tau_{\underline{ij}}$ are normal and shear stresses when $\underline{i}$ and $\underline{j}$ can be the x, y or z directions. The terms inside the surface integral represent surface tractions (external stresses applied to the surface). These are not present in the MRE situation, as all surfaces are either free or subject to a fixed displacement boundary condition, otherwise known as a type 1 or Dirichlet boundary conditions. Therefore setting the surface integral terms to zero, and applying the axial stress definitions given in Eq. A.17 together with the definitions of strain from Eq.

A.21 to the equation for the x direction leads to

$$\Big\langle \frac{\partial \phi}{\partial x}\big(2\mu\frac{\partial u}{\partial x} - P\big) + \frac{\partial \phi}{\partial y}\big(\frac{\partial u}{\partial y} + \frac{\partial v}{\partial x}\big) + \frac{\partial \phi}{\partial z}\big(\frac{\partial w}{\partial x} + \frac{\partial u}{\partial z}\big)\Big\rangle = -\Big\langle \rho\phi\frac{\partial^2 u}{\partial t^2}\Big\rangle. \tag{B.21}$$

The same methods can be applied to the equations for the y and z equations. The ϕ basis functions are used to support the displacements, and the ψ basis functions to support the pressures, so that $u = \sum_{j=1}^{27} u_j\phi_j$, $v = \sum_{j=1}^{27} v_j\phi_j$, $w = \sum_{j=1}^{27} w_j\phi_j$ and $P = \sum_{n=1}^{4} P_n\psi_n$. μ and ρ can be nodally varying if they are supported on the ϕ basis functions, so that $\mu = \sum_{k=1}^{27} \mu_k\phi_k$ and $\rho = \sum_{k=1}^{27} \rho_k\phi_k$. If steady state motion of the form $\mathbf{u}(\mathbf{x},t) = \mathfrak{Re}\{\bar{\mathbf{u}}e^{i\omega t}\}$ is assumed, $\frac{\partial^2 \mathbf{u}}{\partial t^2} = -\omega^2\mathfrak{Re}\{\bar{\mathbf{u}}e^{i\omega^2}\}$. This gives the weighted residual equations in each of the 3 directions for the weighting function ϕ_i as

$$\begin{aligned}\Big\langle \sum_{j=1}^{27}\sum_{k=1}^{27}\Bigg(&\Big[\mu_k\phi_k\big(2\frac{\partial\phi_i}{\partial x}\frac{\partial\phi_j}{\partial x} + \frac{\partial\phi_i}{\partial y}\frac{\partial\phi_j}{\partial y} + \frac{\partial\phi_i}{\partial z}\frac{\partial\phi_j}{\partial z}\big) - \omega^2\phi_i\phi_j\phi_k\rho_k\Big]\bar{u}_j \\ &+ \Big[\mu_k\phi_k\frac{\partial\phi_i}{\partial y}\frac{\partial\phi_j}{\partial z}\Big]\bar{v}_j + \Big[\mu_k\phi_k\frac{\partial\phi_i}{\partial z}\frac{\partial\phi_j}{\partial x}\Big]\bar{w}_j\Bigg) \\ &+ \sum_{n=1}^{4}\left(\frac{\partial\phi_i}{\partial x}\Psi_n P_n\right)\Big\rangle = 0\end{aligned} \tag{B.22a}$$

$$\begin{aligned}\Big\langle \sum_{j=1}^{27}\sum_{k=1}^{27}\Bigg(&\Big[\mu_k\phi_k\frac{\partial\phi_i}{\partial x}\frac{\partial\phi_j}{\partial y}\Big]\bar{u}_j \\ &+ \Big[\mu_k\phi_k\big(\frac{\partial\phi_i}{\partial x}\frac{\partial\phi_j}{\partial x} + \frac{\partial\phi_i}{\partial y}\frac{\partial\phi_j}{\partial y} + 2\frac{\partial\phi_i}{\partial z}\frac{\partial\phi_j}{\partial z}\big) - \omega^2\phi_i\phi_j\phi_k\rho_k\Big]\bar{v}_j \\ &+ \Big[\mu_k\phi_k\frac{\partial\phi_i}{\partial z}\frac{\partial\phi_j}{\partial y}\Big]\bar{w}_j\Bigg) + \sum_{n=1}^{4}\left(\frac{\partial\phi_i}{\partial y}\Psi_n P_n\right)\Big\rangle = 0\end{aligned} \tag{B.22b}$$

$$\begin{aligned}\Big\langle \sum_{j=1}^{27}\sum_{k=1}^{27}\Bigg(&\Big[\mu_k\phi_k\frac{\partial\phi_i}{\partial x}\frac{\partial\phi_j}{\partial z}\Big]\bar{u}_j + \Big[\mu_k\phi_k\frac{\partial\phi_i}{\partial y}\frac{\partial\phi_j}{\partial z}\Big]\bar{v}_j \\ &+ \Big[\mu_k\phi_k\big(\frac{\partial\phi_i}{\partial x}\frac{\partial\phi_j}{\partial x} + \frac{\partial\phi_i}{\partial y}\frac{\partial\phi_j}{\partial y} + 2\frac{\partial\phi_i}{\partial z}\frac{\partial\phi_j}{\partial z}\big) - \omega^2\phi_i\phi_j\phi_k\rho_k\Big]\bar{w}_j\Bigg) \\ &+ \sum_{n=1}^{4}\left(\frac{\partial\phi_i}{\partial z}\Psi_n P_n\right)\Big\rangle = 0.\end{aligned} \tag{B.22c}$$

The Galerkin weighted residual equations for the ψ weighting functions are simpler to derive. The residual for the pressure equation (Eq. A.24) is defined as

$$R_p = -\frac{\partial u}{\partial x} - \frac{\partial u}{\partial x} - \frac{\partial u}{\partial x} - \frac{P}{K}. \tag{B.23}$$

The Galerkin weighted residual statement for a weighting function ψ_m can then be written as

$$\iiint_{\Omega} \psi_m \Big(- \frac{\partial u}{\partial x} - \frac{\partial u}{\partial x} - \frac{\partial u}{\partial x} - \frac{P}{K} \Big) = 0. \tag{B.24}$$

Using the basis function expansions for pressure and displacement given in Eqs. B.2 and B.7 leads to:

$$\Big\langle \sum_{j=1}^{27} \Big(- \big[\psi_m \frac{\partial \phi_j}{\partial x}\big] \bar{u}_j - \big[\psi_m \frac{\partial \phi_j}{\partial y}\big] \bar{v}_j - \big[\psi_m \frac{\partial \phi_j}{\partial w}\big] \bar{w}_j \Big) - \sum_{n=1}^{4} \Big(\frac{\psi_m \psi_n}{K} \bar{P}_n \Big) \Big\rangle = 0 \tag{B.25}$$

A weighted residual equation is created for each ϕ and each ψ weighting function, which will lead to as many equations as unknown variables, i.e. each $u_j, v_j, w_j, p_n, \frac{\partial p_n}{\partial x}, \frac{\partial p_n}{\partial y}$ and $\frac{\partial p_n}{\partial z}$, so that the matrix-vector system can be solved for the displacements and pressures. The structuring of Eqs. B.22 and B.25 allow the FE matrix to maintain symmetry, therefore increasing memory and computational efficiency. In order build a FE matrix-vector system from Eqs. B.21 and B.25, the matrix is divided into parts

$$\left(\begin{array}{ccc|c} \ddots & & & \\ & \mathbf{A}_{dd} & & \mathbf{A}_{dp} \\ & & \ddots & \\ \hline & \mathbf{A}_{pd} & & \mathbf{A}_{pp} \end{array} \right) \left\{ \begin{array}{c} \vdots \\ \mathbf{u}_t \\ \vdots \\ \hline \mathbf{P}_t \end{array} \right\} = \left\{ \begin{array}{c} \vdots \\ \mathbf{R}_{ut} \\ \vdots \\ \hline \mathbf{R}_{pt} \end{array} \right\}. \tag{B.26}$$

Here, $\mathbf{u}_t$ represent the unknown displacement terms, and $\mathbf{R}_{ut}$ are the corresponding RHS terms. Similarly, $\mathbf{P}_t$ are the unknown pressure terms, and $\mathbf{R}_{pt}$ are their corresponding RHS terms. $\mathbf{A}_{dd}$ contains the terms from the WR equations with displacement basis functions as weighting functions (Eq. B.22) which multiply displacement unknowns, and $\mathbf{A}_{dp}$ contains the terms from the same equations which multiply pressure unknowns. $\mathbf{A}_{pp}$ contains terms from the WR equations with pressure basis functions as weighting functions (Eq. B.25) which multiply displacement unknowns, and $\mathbf{A}_{pp}$ are terms from the same equation which multiply pressure unknowns.

$\mathbf{A}_{dd}$ is built from 3 $\times$ 3 sub-matrices for the i'th weighting function, and j'th displacement interpolating function, given by

$$\left(\begin{array}{ccc} A_{dd}(1,1) & A_{dd}(1,2) & A_{dd}(1,3) \\ A_{dd}(2,1) & A_{dd}(2,2) & A_{dd}(2,3) \\ A_{dd}(3,1) & A_{dd}(3,2) & A_{dd}(3,3) \end{array} \right) \left\{ \begin{array}{c} u_j \\ v_j \\ w_j \end{array} \right\} = \left\{ \begin{array}{c} R_{ju} \\ R_{jv} \\ R_{jw} \end{array} \right\}, \tag{B.27}$$

where u_j, v_j and w_j are the j'th displacement DOF's, R_{ju}, R_{jv} and R_{jw} are the corresponding RHS vector terms, and the matrix terms are given by

$$
\begin{aligned}
A_{dd}(1,1) &= \Big\langle \sum_{k=1}^{27} \Big(\mu_k \phi_k \big(2\frac{\partial \phi_i}{\partial x}\frac{\partial \phi_j}{\partial x} + \frac{\partial \phi_i}{\partial y}\frac{\partial \phi_j}{\partial y} + \frac{\partial \phi_i}{\partial z}\frac{\partial \phi_j}{\partial z} \big) - \omega^2 \phi_i \phi_j \phi_k \rho_k \Big) \Big\rangle \\
A_{dd}(1,2) &= \Big\langle \sum_{k=1}^{27} \Big(\mu_k \phi_k \frac{\partial \phi_i}{\partial y}\frac{\partial \phi_j}{\partial z} \Big) \Big\rangle \\
A_{dd}(1,3) &= \Big\langle \sum_{k=1}^{27} \Big(\mu_k \phi_k \frac{\partial \phi_i}{\partial z}\frac{\partial \phi_j}{\partial x} \Big) \Big\rangle \\
A_{dd}(2,1) &= \Big\langle \sum_{k=1}^{27} \Big(\mu_k \phi_k \frac{\partial \phi_i}{\partial x}\frac{\partial \phi_j}{\partial y} \Big) \Big\rangle \\
A_{dd}(2,2) &= \Big\langle \sum_{k=1}^{27} \Big(\mu_k \phi_k \big(\frac{\partial \phi_i}{\partial x}\frac{\partial \phi_j}{\partial x} + 2\frac{\partial \phi_i}{\partial y}\frac{\partial \phi_j}{\partial y} + \frac{\partial \phi_i}{\partial z}\frac{\partial \phi_j}{\partial z} \big) - \omega^2 \phi_i \phi_j \phi_k \rho_k \Big) \Big\rangle \\
A_{dd}(2,3) &= \Big\langle \sum_{k=1}^{27} \Big(\mu_k \phi_k \frac{\partial \phi_i}{\partial z}\frac{\partial \phi_j}{\partial y} \Big) \Big\rangle \\
A_{dd}(3,1) &= \Big\langle \sum_{k=1}^{27} \Big(\mu_k \phi_k \frac{\partial \phi_i}{\partial x}\frac{\partial \phi_j}{\partial z} \Big) \Big\rangle \\
A_{dd}(3,2) &= \Big\langle \sum_{k=1}^{27} \Big(\mu_k \phi_k \frac{\partial \phi_i}{\partial y}\frac{\partial \phi_j}{\partial z} \Big) \Big\rangle \\
A_{dd}(3,3) &= \Big\langle \sum_{k=1}^{27} \Big(\mu_k \phi_k \big(\frac{\partial \phi_i}{\partial x}\frac{\partial \phi_j}{\partial x} + \frac{\partial \phi_i}{\partial y}\frac{\partial \phi_j}{\partial y} + 2\frac{\partial \phi_i}{\partial z}\frac{\partial \phi_j}{\partial z} \big) - \omega^2 \phi_i \phi_j \phi_k \rho_k \Big) \Big\rangle .
\end{aligned}
\tag{B.28}
$$

Equations B.22 and B.25 show $\mathbf{A}_{dp} = \mathbf{A}_{dp}^T$, therefore only one of them needs to be built. $\mathbf{A}_{dp}$ is built up from 3×1 sub-matrices for the i'th displacement weighting function and n'th pressure interpolating function.

$$
\begin{pmatrix} A_{dp}(1,1) \\ A_{dp}(2,1) \\ A_{dp}(3,1) \end{pmatrix} \left\{ \; P_n \; \right\} = \begin{Bmatrix} R_{ix} \\ R_{iy} \\ R_{iz} \end{Bmatrix}, \tag{B.29}
$$

where P_n is the n'th pressure unknown, and R_{ix}, R_{iy} R_{iz} are the RHS vector terms for WR equation i in the x, y and z directions respectively, and

$$
A_{dp}(1,1) = \langle \frac{\partial \phi_i}{\partial x} \Psi_n \rangle, \quad A_{dp}(2,1) = \langle \frac{\partial \phi_i}{\partial y} \Psi_n \rangle, \quad A_{dp}(3,1) = \langle \frac{\partial \phi_i}{\partial z} \Psi_n \rangle. \tag{B.30}
$$

$\mathbf{A}_{pp}$ is a 4 $\times$ 1 sub-matrix for each pressure basis weighting function, m.

$$\begin{pmatrix} A_{pp}(1,1) & A_{pp}(1,2) & A_{pp}(1,3) & A_{pp}(1,4) \end{pmatrix} \begin{Bmatrix} P_m \\ \frac{\partial P}{\partial x}_m \\ \frac{\partial P}{\partial y}_m \\ \frac{\partial P}{\partial z}_m \end{Bmatrix} = \begin{Bmatrix} R_m \end{Bmatrix}, \tag{B.31}$$

with terms given by

$$\begin{aligned} A_{pp}(1,1) &= \frac{\psi_m \psi_1}{K} \\ A_{pp}(1,2) &= \frac{\psi_m \psi_2}{K} \\ A_{pp}(1,3) &= \frac{\psi_m \psi_3}{K} \\ A_{pp}(1,4) &= \frac{\psi_m \psi_4}{K}. \end{aligned} \tag{B.32}$$

Unlike linear tetrahedral elements, quadratic hexahedral elements do not have analytic solutions to the required integrals over the volume, so these integrals must be calculated numerically. Gaussian quadrature provides the most efficient method to do this. A Gaussian scheme using N_G points in each direction can exactly calculate the integral of a polynomial of order $2N_G - 1$. The integral is calculated as a weighted sum of the function values at a specially selected set of points, called Gauss points. The highest order polynomial present in Eq. B.22 comes from the $\phi_i \phi_j \phi_k$ term, and is of order 6. For this reason, 4 Gauss points, which can exactly integrate a polynomial of order 7 were chosen. The 4 point Gaussian quadrature scheme to numerically integrate a function $g(x, y, z)$, with weights and gauss point locations is given below.

$$\int_{-1}^{1}\int_{-1}^{1}\int_{-1}^{1} g(x,y,z)dx\,dy\,dz \approx \sum_{i_g=1}^{4}\sum_{j_g=1}^{4}\sum_{k_g=1}^{4} \Big(w_g(i) w_g(j) w_g(k) g(x_g(i), x_g(j), x_g(k)) \Big) \det \mathbf{J}_c, \tag{B.33}$$

where the weights, w_g, and gauss points, x_g are given by

$$\begin{aligned} w_g(1) &= \frac{18 - \sqrt{30}}{36} & x_g(1) &= -\sqrt{\frac{3 + 2\sqrt{6/5}}{7}} \\ w_g(2) &= \frac{18 + \sqrt{30}}{36} & x_g(2) &= -\sqrt{\frac{3 - 2\sqrt{6/5}}{7}} \\ w_g(3) &= \frac{18 + \sqrt{30}}{36} & x_g(3) &= \sqrt{\frac{3 - 2\sqrt{6/5}}{7}} \\ w_g(4) &= \frac{18 - \sqrt{30}}{36} & x_g(4) &= \sqrt{\frac{3 + 2\sqrt{6/5}}{7}}, \end{aligned} \tag{B.34}$$

and $\mathbf{J}_c$ is the coordinate Jacobian matrix defined in Eq. B.11. Fixed displacement (Dirichlet) boundary conditions (BC's) are known as type 1 boundary conditions in FE. These are applied by replacing the weighted residual equation for the degree of freedom corresponding to the boundary condition with

$$u_{BC} = D_{BC}, \tag{B.35}$$

where u_{BC} is the degree of freedom, and D_{BC} is the BC value. This equates to zeroing the BC row of the FE matrix and inserting a '1' on the diagonal, then inserting D_{BC} into the right hand side vector. In order to maintain symmetry of the FE matrix, the BC column terms in the FE matrix are multiplied by D_{BC} and moved to the right hand side vector. Surface traction, or type 2 boundary conditions are not present in the MRE situation, as type 1 conditions are applied over the entire boundary.

The standard finite element assembly algorithm [23, 54] is used to position these sub-matrices into the global FE matrix. The global FE matrix is a sparse matrix, so is stored in a sparse format to conserve memory, using three arrays. If N_{nz} is the number of non-zero matrix entries, the first array, $\mathbf{A}_s$, is a $N_{nz} \times 1$ array containing the value of each non-zero matrix entry. The second, $\mathbf{J}_{cn}$ is a $N_{nz} \times 1$ array containing the column numbers of the corresponding entry in $\mathbf{A}_s$. A similar matrix could be used to hold the row numbers of the matrix, however to facilitate the matrix assembly, an array of a different format , $\mathbf{I}_{ptr}$, is used. The first column of $\mathbf{I}_{ptr}$ contains the number of non-zeros in each row of the global FE matrix, and the next columns contain the position in $\mathbf{A}_s$ which contains the non-zero matrix value. This sparse matrix vector system is then solved using the MUMPS package [55], which is an efficient parallelizable sparse solver. An example of this sparse storage format is given below. The matrix

$$\begin{pmatrix} 3 & 0 & 7 & 0 \\ 0 & 1 & 6 & 0 \\ 5 & 2 & 7 & 0 \\ 0 & 0 & 0 & 10 \end{pmatrix},$$

would be represented by the sparse storage arrays:

$$\mathbf{A}_s = \begin{pmatrix} 3 \\ 7 \\ 1 \\ 6 \\ 5 \\ 2 \\ 7 \\ 10 \end{pmatrix}; \mathbf{J}_{cn} = \begin{pmatrix} 1 \\ 3 \\ 2 \\ 3 \\ 1 \\ 2 \\ 3 \\ 4 \end{pmatrix} \text{ and } \mathbf{I}_{ptr} = \begin{pmatrix} 2 & 1 & 2 & 0 \\ 2 & 3 & 4 & 0 \\ 3 & 5 & 6 & 7 \\ 1 & 8 & 0 & 0 \end{pmatrix}.$$

Appendix C

Dealing with Complex Variables

The implementation of a Rayleigh material model in the forward FE problem is a simple matter of changing the relevant variable declarations from real to complex, because only basic arithmetic is performed using complex numbers. However, during the material property reconstruction process, more complicated operations are required, such as differentiation, inner and outer products, along with dealing with the real and imaginary parts of a variable separately. All of these problems can be made conceptually simple by separating the real and imaginary parts of the complex variables, so that the generalized complex matrix-vector system

$$\begin{pmatrix} m_1 + m_2 i & m_3 + m_4 i \\ m_5 + m_6 i & m_7 + m_8 i \end{pmatrix} \begin{Bmatrix} v_1 + v_2 i \\ v_3 + v_4 i \end{Bmatrix} = \begin{Bmatrix} r_1 + r_2 i \\ r_3 + r_4 i \end{Bmatrix}, \tag{C.1}$$

is equivalent to the real system

$$\begin{pmatrix} m_1 & -m_2 & m_3 & -m_4 \\ m_2 & m_1 & m_4 & m_3 \\ m_5 & -m_6 & m_7 & -m_8 \\ m_6 & m_5 & m_8 & m_7 \end{pmatrix} \begin{Bmatrix} v_1 \\ v_2 \\ v_3 \\ v_4 \end{Bmatrix} = \begin{Bmatrix} r_1 \\ r_2 \\ r_3 \\ r_4 \end{Bmatrix}. \tag{C.2}$$

The complex-valued forward FE problem can therefore be converted into a real-valued system, therefore all material property reconstruction methods can remain unchanged from those used for real valued systems. The downside to using this method include the increase in memory required to store split matrices (an NxN complex matrix becomes a 2Nx2N real matrix, which uses twice as much memory), and the programming infrastructure required to keep track of what is going on. In most cases, a much more elegant solution is possible using complex algebra and by switching the transpose operator (superscript 'T') from the real system with the complex conjugate transpose, denoted by a superscript 'H' for the complex system [31].

Inner Product

If 2 complex vectors are considered, $\mathbf{c}_a$ and $\mathbf{c}_b$, along with real-valued vectors, $\mathbf{r}_a$ and $\mathbf{r}_b$, which consist of the real and imaginary parts of $\mathbf{c}_a$ and $\mathbf{c}_b$,

$$\mathbf{c}_a = \left\{ \begin{array}{c} v_1 + iv_2 \\ v_3 + iv_4 \end{array} \right\}, \quad \text{and} \quad \mathbf{r}_a = \left\{ \begin{array}{c} v_1 \\ v_2 \\ v_3 \\ v_4 \end{array} \right\} \tag{C.3a}$$

$$\mathbf{c}_b = \left\{ \begin{array}{c} v_5 + iv_6 \\ v_7 + iv_8 \end{array} \right\}, \quad \text{and} \quad \mathbf{r}_b = \left\{ \begin{array}{c} v_5 \\ v_6 \\ v_7 \\ v_8 \end{array} \right\}, \tag{C.3b}$$

a complex inner product which is consistent with the inner product of split vectors can be derived by comparing $\mathbf{c}_a^H \mathbf{c}_b$ with $\mathbf{r}_a^T \mathbf{r}_b$:

$$\mathbf{c}_a^H \mathbf{c}_b = v_1 v_5 + v_2 v_6 + v_3 v_7 + v_4 v_8 + i(v_1 v_6 - v_2 v_5 + v_3 v_8 - v_4 v_7) \tag{C.4a}$$

$$\mathbf{r}_a^T \mathbf{r}_b = v_1 v_5 + v_2 v_6 + v_3 v_7 + v_4 v_8. \tag{C.4b}$$

Therefore $\mathbf{r}_a^T \mathbf{r}_b = \mathfrak{Re}\{\mathbf{c}_a^H \mathbf{c}_b\}$.

Derivatives

The derivative of an analytic function (one which satisfies the Cauchy-Riemann equations [56]), $g(s)$, with respect to the complex variable s, which is given by $s = s_r + is_i$ is handled exactly the same as the real case. The derivatives with respect to the real and imaginary parts are related to the complex derivative by:

$$\frac{\partial g}{\partial s} = \frac{\partial g}{\partial s_r} = i\frac{\partial g}{\partial s_i}. \tag{C.5}$$

A non-analytic function, such as one involving conjugation, for example the error function,

$$\Phi = \overline{(\mathbf{u}_c(\theta) - \mathbf{u}_m)}(\mathbf{u}_c(\theta) - \mathbf{u}_m), \tag{C.6}$$

where the overbar represents the complex conjugate, does not have a derivative in the standard sense, that is the value of the limit,

$$\lim_{\Delta_\theta \to 0} \left(\frac{\Phi(s + \Delta_\theta) - \Phi(\theta)}{\Delta_\theta}\right), \tag{C.7}$$

is dependent on the direction from which Δ_θ approaches zero in the complex plane. However, the for a given point to be considered stationary point for a particular variable θ_k, it is sufficient for

$$\frac{\partial \Phi}{\partial(\mathfrak{Re}\{\theta_k\})} = \frac{\partial \Phi}{\partial(\mathfrak{Im}\{\theta_k\})} = 0. \tag{C.8}$$

Finite Difference Check

A finite difference check of a derivative of a non-analytic function, g, with respect to a complex variable, $s = s_r + is_i$, calculated through the Gauss-Newton or adjoint methods, can be carried out using

$$\frac{\partial g}{\partial s} \approx \frac{g(s + \Delta s_r) - g(s)}{\Delta s_r} + i\frac{g(s + i\Delta s_i) - g(s)}{\Delta s_i}. \tag{C.9}$$

Separate Real and Imaginary parts

If optimization with respect to either the real or imaginary part of a complex parameter on its own is required, any matrix-vector system, such as in the Gauss-Newton algorithm (section 2.3.2) must be split into real and imaginary parts as in Eq. C.2. Any vector-vector operations such as in the Conjugate Gradient method (section 2.3.1) can be dealt with by simply setting the appropriate real or imaginary parts of the vectors to zero.

If the real and imaginary parts of a complex parameter are scaled by different values, so that the true parameter value, θ, is related to the scaled value, θ_{sc} by

$$\theta = R_{sc}\mathfrak{Re}\{\theta_{sc}\} + I_{sc}\mathfrak{Im}\{\theta_{sc}\}, \tag{C.10}$$

where R_{sc} and I_{sc} are the real and imaginary scaling factors, it is not possible to differentiate with respect to the complex θ_{sc}. This problem could be alleviated by converting R_{sc} and I_{sc} into a single complex-valued scaling factor, C_{sc}, so that $\theta = C_{sc}\theta_{sc}$, and

$$\begin{aligned}
\mathfrak{Re}\{C_{sc}\} &= R_{sc}\mathfrak{Re}\{\theta_{sc}\} + \left(\frac{I_{sc}\mathfrak{Im}\{\theta_{sc}\} - R_{sc}\mathfrak{Re}\{\theta_{sc}\}\mathfrak{Im}\{\theta_{sc}\}}{\mathfrak{Im}\{\theta_{sc}\}^2 + \mathfrak{Re}\{\theta_{sc}\}}\right)\mathfrak{Im}\{\theta_{sc}\} \\
\mathfrak{Im}\{C_{sc}\} &= \frac{I_{sc}\mathfrak{Im}\{\theta_{sc}\} - R_{sc}\mathfrak{Re}\{\theta_{sc}\}\mathfrak{Im}\{\theta_{sc}\}}{\mathfrak{Im}\{\theta_{sc}\}^2 + \mathfrak{Re}\{\theta_{sc}\}}.
\end{aligned} \tag{C.11}$$

This allows differentiation with respect to the complex θ_{sc}. These equations simplify considerably if $\theta_{sc} = 1 + i$, giving

$$C_{sc} = \frac{1}{2}\big[(I_{sc} - R_{sc}) + i(I_{sc} + R_{sc})\big].$$

References

[1] A. Jemal, R. Siegel, E. Ward, Y. Hao, J. Xu, T. Murray, and M.J. Thun. Cancer Statistics, 2008. *CA: A Cancer Journal for Clinicians*, 58(2):71–96, 2008.

[2] New Zealand Health Information Service. Cancer patient survival covering the period 1994 to 2003. *NZ Ministry of Health*, 2006.

[3] L. Tabar, M.F. Yen, B. Vitak, H.H.T. Chen, R.A. Smith, and S.W. Duffy. Mammography service screening and mortality in breast cancer patients: 20-year follow-up before and after introduction of screening. *The Lancet*, 361(9367):1405–1410, 2003.

[4] M. Kriege, C.T.M. Brekelmans, C. Boetes, P.E. Besnard, H.M. Zonderland, I.M. Obdeijn, R.A. Manoliu, T. Kok, H. Peterse, M.M.A. Tilanus-Linhorst, et al. Efficacy of Magnetic Resonance Imaging and Mammography for Breast Cancer Screening in Women With a Familial or Genetic Predisposition. *Obstetrical & Gynecological Survey*, 60(2):107, 2005.

[5] R. Sapir, M. Patlas, S.D. Strano, I. Hadas-Halpern, and N.I. Cherny. Does Mammography Hurt? *Journal of Pain and Symptom Management*, 25(1):53–63, 2003.

[6] O. Olsen and P.C. Gøtzsche. Cochrane review on screening for breast cancer with mammography. *The Lancet*, 358(9290):1340–1342, 2001.

[7] J. Ophir, B. Garra, F. Kallel, E. Konofagou, T. Krouskop, R. Righetti, and T. Varghese. Elastographic imaging. *Ultrasound Med Biol*, 26(suppl 1):S23–S29, 2000.

[8] S. Catheline, F. Wu, and M. Fink. A solution to diffraction biases in sonoelasticity: The acoustic impulse technique. *The Journal of the Acoustical Society of America*, 105:2941, 1999.

[9] E. E. W. Van Houten, M. M. Doyley, F. E. Kennedy, J. B. Weaver, and K. D. Paulsen. Initial in-vivo experience with steady-state subzone-based MR elastography of the human breast. *J. Magn. Reson. Imaging*, 17:72–85, 2003.

[10] R. Sinkus, J. Lorenzen, D. Schrader, M. Lorenzen, M. Dargatz, and D. Holz. High-resolution tensor MR elastography for breast tumour detection. *Phys. Med. Biol*, 45(6):1649–1664, 2000.

[11] K.J. Parker, L.S. Taylor, S. Gracewski, and D.J. Rubens. A unified view of imaging the elastic properties of tissue. *The Journal of the Acoustical Society of America*, 117:2705, 2005.

[12] I. Cespedes, J. Ophir, H. Ponnekanti, and N. Maklad. Elastography: elasticity imaging using ultrasound with application to muscle and breast in vivo. *Ultrason Imaging*, 15(2):73–88, 1993.

[13] A. Manduca, T.E. Oliphant, M.A. Dresner, J.L. Kruse, E. Amromin, J.P. Felmlee, J.F Greenleaf, and R.L. Ehman. Magnetic resonance elastography: Non-invasive mapping of tissue elasticity. *Medical Image Analysis*, 5:237–254, 2001.

[14] M. Doyley and J. Weaver. MAGNETIC RESONANCE ELASTOGRAPHY: EXPERIMENTAL VALIDATION AND PERFORMANCE OPTIMIZATION. *Alternative Breast Imaging: Four Model-Based Approaches*, 2005.

[15] A. Peters, J.G. Chase, and E.E.W. Van Houten.

[16] A. Samani, J. Zubovits, and D. Plewes. Elastic moduli of normal and pathological human breast tissues: an inversion-technique-based investigation of 169 samples. *Phys. Med. Biol*, 52(6):1565–1576, 2007.

[17] E. E. W. Van Houten, M. M. Doyley, F. E. Kennedy, K. D. Paulsen, and J. B. Weaver. A three-parameter mechanical property reconstruction method for MR-based elastic property imaging. *IEEE Trans. Medical Imaging*, 24:311–324, 2005.

[18] R. Sinkus, M. Tanter, T. Xydeas, S. Catheline, J. Bercoff, and M. Fink. Viscoelastic shear properties of in vivo breast lesions measured by MR elastography. *Magnetic Resonance Imaging*, 23:159–165, 2005.

[19] R. Sinkus, M. Tanter, S. Catheline, J. Lorenzen, C. Kuhl, E. Sondermann, and M. Fink. Imaging anisotropic and viscous properties of breast tissue by magnetic resonance-elastography. *Magnetic Resonance In Medicine*, 53:372–387, 2005.

[20] D. R. Bland. *The Theory of Linear Viscoelasticity.* Pergamon Press, Oxford, 1960.

[21] T. E. Oliphant, A. Manduca, R. L. Ehman, and J. F. Greenleaf. Complex-valued stiffness reconstruction for magnetic resonance elastography by algebraic inversion of the differential equation. *Magnetic Resonance in Medicine*, 45:299–310, 2001.

[22] W. Flugge. *Viscoelasticity.* Springer, Berlin, 1975 (second revised edition).

[23] R. D. Cook, D. S. Malkus, M. E. Plesha, and R. J. Witt. *Concepts and Applications of Finite Element Analysis*. Wiley, New York, 2002 (4th edition).

[24] A.D. Zacharopoulos, S.R. Arridge, O. Dorn, V. Kolehmainen, and J. Sikora. Three-dimensional reconstruction of shape and piecewise constant region values for optical tomography using spherical harmonic parametrization and a boundary element method. *Inverse Problems*, 22(5):1509–1532, 2006.

[25] J. Nocedal and S.J. Wright. *Numerical Optimization*. Springer, 1999.

[26] J.R. Shewchuk. An introduction to the conjugate gradient method without the agonizing pain. *unpublished paper*.

[27] E. Polak and G. Ribiere. Note sur la convergence de methods de directions conjugres, Revue francaise informat. *Recherche operationnelle*, 16:35–43, 1969.

[28] A.A. Oberai, N.H. Gokhale, and G.R. Feij o. Solution of inverse problems in elasticity imaging using the adjoint method. *Inverse Problems*, 19(2):297–313, 2003.

[29] H. Ling Liew and P.M. Pinsky. Recovery of shear modulus in elastography using an adjoint method with B-spline representation. *Finite Elements in Analysis & Design*, 41(7-8):778–799, 2005.

[30] S.J. Norton. Iterative inverse scattering algorithms: Methods of computing Fréchet derivatives. *The Journal of the Acoustical Society of America*, 106:2653, 1999.

[31] C.R. Vogel. *Computational Methods for Inverse Problems*. Society for Industrial Mathematics, 2002.

[32] N. Joachimowicz, C. Pichot, and J-P. Hugonin. Inverse scattering: An iterative numerical method for electromagnetic imaging. *IEEE. Trans. Antennas. Propogat.*, 39:1742–1752, 1991.

[33] D. W. Marquadt. An algorithm for least-squares estimation of non-linear parameters. *J. Soc. Indust. Appl. Math.*, 11:431–441, 1953.

[34] R.H. Byrd, J. Nocedal, and Y. Yuan. Global convergence of a class of quasi-Newton methods on convex problems. *SIAM J. Numer. Anal*, 24(5):1171–1190, 1987.

[35] J.C. Gilbert and J. Nocedal. Global convergence properties of conjugate gradient methods for optimization. *SIAM Journal on Optimization*, 2(1):21–42, 1992.

[36] P. Wolfe. Convergence conditions for ascent methods. *SIAM Review*, 11(2):226–235, 1969.

[37] EEW Van Houten, KD Paulsen, MI Miga, FE Kennedy, and JB Weaver. An overlapping subzone technique for MR-based elastic property reconstruction. *Magnetic Resonance in Medicine*, 42(4):779–786, 1999.

[38] E. E. W. van Houten, J. B. Weaver, M. I. Miga, F. E. Kennedy, and K. D. Paulsen. Elasticity reconstruction from experimental MR displacement data: initial experience with an overlapping subzone finite element inversion process. *Medical Physics*, 27:101–107, January 2000.

[39] E. E. W. Van Houten, M. I. Miga, J. B. Weaver, F. E. Kennedy, and K. D. Paulsen. Three-dimensional subzone-based reconstruction algorithm for MR elastography. *Magnetic Resonance in Medicine*, 45:827–837, 2001.

[40] L. Landini, V. Positano, and M. F. Santarelli. *Advanced Image Processing In Magnetic Resonance Imaging*. CRC Press, 2005.

[41] E.M. Haacke, RW Brown, MR Thompson, and R. Venkatesan. *Magnetic Resonance Imaging: Physical Principles and Sequence Design. 1999*. New York: John Wiley & Sons, Inc.

[42] CEI. *Ensight User Manual*, 2007.

[43] J.M. Ortega and W.C. Rheinboldt. *Iterative Solution of Nonlinear Equations in Several Variables*. Society for Industrial and Applied Mathematics Philadelphia, PA, USA, 2000.

[44] J. F. Semblat. Rheological interpretation of rayleigh damping. *Journal of Sound and Vibration*, 206:741–744, 1997.

[45] M.M. Doyley, J.B. Weaver, E.E.W. Van Houten, F.E. Kennedy, and K.D. Paulsen. Thresholds for detecting and characterizing focal lesions using steady-state MR elastography. *Medical Physics*, 30:495, 2003.

[46] AP Sarvazyan, AR Skovoroda, SY Emelianov, JB Fowlkes, JG Pipe, RS Adler, RB Buxton, and PL Carson. Biophysical bases of elasticity imaging. *Acoustical Imaging*, 21:223–240, 1995.

[47] TA Krouskop, TM Wheeler, F. Kallel, BS Garra, and T. Hall. Elastic moduli of breast and prostate tissues under compression. *Ultrason Imaging*, 20(4):260–74, 1998.

[48] C. Verdier. Review Article: Rheological Properties of Living Materials. From Cells to Tissues. *Computational and Mathematical Methods in Medicine*, 5(2):67–91, 2003.

[49] B. Fabry, G.N. Maksym, J.P. Butler, M. Glogauer, D. Navajas, N.A. Taback, E.J. Millet, and J.J. Fredberg. Time scale and other invariants of integrative mechanical behavior in living cells. *Physical Review E*, 68(4):41914, 2003.

[50] M.Z. Kiss, T. Varghese, and T.J. Hall. Viscoelastic characterization of in vitro canine tissue. *Phys. Med. Biol*, 49(18):4207–4218, 2004.

[51] R. Sinkus, K. Siegmann, T. Xydeas, M. Tanter, C. Claussen, and M. Fink. MR elastography of breast lesions: understanding the solid/liquid duality can improve the specificity of contrast-enhanced MR mammography. *Magn Reson Med*, 58(6):1135–44, 2007.

[52] A. Peters. *Digital Image Elasto-Tomography: Mechanical property Reconstruction from Surface Measured Displacement Data*. PhD thesis.

[53] R. Kouhia and R. Stenberg. A linear nonconforming finite element method for nearly incompressible elasticity and stokes flow. *Computer Methods in Applied Mechanics and Engineering*, 124(3):195–212, 1995.

[54] O.C. Zienkiewicz and R.L. Taylor. *The Finite Element Method. Vol. 1,. The Basis*. Butterworth-Heinemann, 2000.

[55] P. R. Amestoy, A. Guercmouche, J-Y. L'Excellent, S. Pralet, G. Alessandrini, A. Morassi, and E. Rosset. Hybrid scheduling for the parallel solution of linear systems. *Parallel Computing*, 32:136–156, 2006.

[56] S. Gong and Y. Gong. *Concise Complex Analysis*. World Scientific, 2007.